

Time Series Searching, Forecasting, and Classification 1  
with Applications in Bioinformatics 2  
時系列の探索・予測・分類とその生命情報学へ 3  
の応用 4

Coleman Yu 5  
余 浩旻



# Abstract

7

Time series data are ubiquitous across many different fields. Much of the data are inherently time series data. Additionally, some data, such as strings, images, and object shapes, that are not originally time series data, can be transformed into time series. Many data mining tasks, such as classification, clustering, and motif finding, have been defined for time series data. Hence, by developing appropriate transformation methods, we can apply a plethora of well-established time series methods to our problems.

This thesis contributes two aspects in time series data mining and bioinformatics. They are a novel application of time series classification to solve complex biological problems by transforming biological data into time series and developing a more expressive distance measure framework that removes certain underlying assumptions.

In the first part, we demonstrate the utility of time series analysis in bioinformatics by studying the problem of predicting Human Dicer Cleavage Sites. Recall that bioinformatics operates at the intersection of **biology**, **biotechnology**, and **informatics**. In this work, we formulate a specific **biology** problem, which is predicting Human Dicer Cleavage sites in microRNA biogenesis, into a machine learning framework. In particular, a multivariate time series classification problem, which is the **informatics** part. Due to current limitations in **biotechnology**, we are constrained to using 1-D RNA sequence inputs rather than 2-D or 3-D data, because these are more expensive to obtain. We propose MTSCCleav, a method that encodes RNA sequences and the probabilities of base pairs in predicted secondary structures into time series data. To the best of our knowledge, we are the first to make use of the probabilities of base pairs in this kind of classification task on RNA data. By doing this, we frame the problem of predicting Human Dicer Cleavage sites into a Multivariate Time Series Classification (MTSC) problem. Existing approaches rely on opaque deep neural networks or complex feature engineering. They are slow, and the feature engineering is over-designed. In contrast, our approach is simple, intuitive, and computationally efficient. The proposed transformation methods allow us to use any well-established time series tools to analyze this biological problem. Experiments demonstrate that MTSCCleav achieves comparable and even better accuracy to state-of-the-art methods while delivering a 3.7X to 28.8X speedup. Furthermore, our perturbation experiments reveal that regions near the center of pre-miRNAs are essential for cleavage-site prediction, consistent with the existing literature.

39 In the second part, we address the limitations of existing similarity measures. Simi-  
40 larity search is a core subroutine in time series data mining tasks. For example, recent  
41 studies show that a simple 1-NN classifier with an appropriate distance measure can out-  
42 perform many advanced, complicated methods. While Dynamic Time Warping (DTW)  
43 and Uniform Scaling (US) are prevailing measures for handling local distortions and  
44 global scaling, respectively, and some studies have demonstrated that combining both  
45 DTW and US is necessary to obtain meaningful results. Current approaches apply a  
46 single scaling factor to the entire sequence. We argue that since distinct phases of a pro-  
47 cess often evolve at different speeds, a single scaling factor is insufficient. We introduce  
48 the first distance measure framework, namely PSD, that achieves invariance to multiple  
49 scaling factors. We also provide speed-up techniques to enable efficient computation of  
50 the PSD. Experiments show that PSD better reflects the similarity between time series  
51 with multiple phases, and that the identified phases (segmentation) provide a clearer  
52 understanding of the data.

53 Collectively, this thesis advances the fields of time series data mining and bioinfor-  
54 matics by demonstrating the use of time series analysis to address fundamental biological  
55 questions and proposing a new, more expressive distance measure framework.

# Acknowledgements

56

To begin, I want to express my deepest gratitude to my PhD supervisor at Kyoto University, Prof. Tatsuya Akutsu. I thank him for his kindness and patience. He is a brilliant researcher who can explain complex concepts simply. In a seminar, he showed that simply using clear notation makes presentations much easier to follow. More importantly, he helps students when they are in “valleys” in their lives. When a car is off track, it needs a push—so do people. I am equally indebted to my MPhil supervisor at The Hong Kong University of Science and Technology (HKUST), Prof. Raymond Chi-Wing Wong. He has continued to help and advise me even after I graduated from HKUST.

Akutsu-sensei taught me the importance of reading good materials. In the weekly seminars, he organized reading seminars, assigning some of his favorite books for us to read and discuss. His favorite book is “Probability and Computing” by Mitzenmacher and Upfal. Additionally, through the journal club he organized, students were asked to present the core ideas from their ten selected papers published in leading venues, such as Nature, Science, Cell, and PNAS. Reading beyond my fields helped me identify research gaps others missed. I think some great ideas are born when we merge the ideas from different fields. He also emphasized the importance of mathematics and proof. It is what computer scientists can stand out in the field of bioinformatics. I think it becomes especially true now, since advances in AI make it possible for almost everyone to code (i.e., Vibe coding). He advised me to use the existing tools, libraries, and studies to leverage my own research. He also taught me that a good researcher must master both oral and written presentation; otherwise, others may misinterpret your talent and the effort you put in. When we are reading a paper, he urges us to identify the novelty and analyze the pros and cons of the paper.

Raymond taught me the power of focus and “First Principles”. I was always surprised that he did not use reference management software like Zotero, preferring to annotate hard copies and even type .bib files manually. He told me that when he starts to do research, he will print out the papers and get focused on the stack of papers (hard copies) in front of him. I am not saying it is beneficial not to use tools, but I want to emphasize the power of focus that underlies his work routine. He taught me that every good research starts with a set of good papers. He also emphasized that there is no right or wrong in research, only what you choose to do about it. His research receipt works as follows. When you

88 are tackling a problem, you first review the relevant existing studies to understand the  
89 state of the art (SOTA) for it. If the existing work addresses your particular problem,  
90 you can apply and adapt it to your problem setting. But most of the time, since your  
91 problem must be a particular version of a general problem, the existing general solution  
92 should not work well for it. It means that you have some room to improve it. And this  
93 is the research gap!. It reminds me of when we deal with the NP-complete problem.  
94 As Kleinberg and Tardos's Algorithm Design (Chapter 10) suggests, an NP-complete  
95 problem (assuming  $P \neq NP$ ) does not allow us to have an algorithm that possesses  
96 all three of the following desired properties simultaneously: Efficiency, Correctness, and  
97 Generalization. Hence, it is sometimes preferable to address a specific instance of the  
98 problem rather than the general one. He also emphasized the theory. He consistently  
99 noted that you need to add theory to the paper to strengthen it. He always mentioned  
100 that you need three motivations (why you are doing it) and three contributions (what you  
101 have done). Sometimes, I ask why he can write so fast, and he replies, "If you know what  
102 you are doing, then you write fast.". He also taught me that when you don't know some  
103 of the ideas, you just go back to the original idea. Doing a "deep first search" can help  
104 you reach the first principle, a concept that Elon Musk, one of the greatest entrepreneurs  
105 of our time, always emphasized. Without these two supervisors, I would not have made  
106 it this far. I could not have finished this program.

107 I would like to take this opportunity to share some of my thoughts on my PhD journey.  
108 I hope the readers may learn something from what I have gone through. My PhD journey  
109 was, to quote Dickens, "the best of times and the worst of times", and to quote Churchill,  
110 "This was their finest hour". For the best parts, it allows me to explore both in my daily  
111 life and in my research. I tried many things, walked many roads, drank many colas and  
112 alcohol, and met many people. This helped me see problems from new perspectives.  
113 Regarding the worst parts, I am reminded of a quote from one of my favorite movies,  
114 "Les Choristes": "Fond de l'étang". It literally means "Bottom of the Pond". At times, I  
115 felt like a frog at the well's bottom, trying hard to get out. Research is fun but also hard.  
116 Research is about exploring something new. It is about publishing (so others can learn  
117 from it). When I am stuck, the best solution is to aim for a reachable, well-defined goal.  
118 The goal should be clear, with obvious rewards and requirements. Also, make sure the  
119 effort of your actions can be accumulated. Like the frog, do not jump randomly, but aim  
120 to move to stable platforms towards escape. Then, each jump matters for your progress.  
121 Two of the materials helped me; they are "Eat the Frog!" and "THE PH.D. GRIND".

122 I would like to thank my thesis committee members. I would like to acknowledge  
123 Tamura-sensei and Mori-sensei (a former member) of the Akutsu laboratory. Tamura-  
124 sensei taught me to focus on the input-output relationship when encountering new algo-  
125 rithms/methods, and Mori-sensei introduced me to the fascinating application of time-  
126 series analysis to gene expression data, especially in trajectory inferences (i.e., pseudo-

time). I would like to thank the many communities that made my life in Japan colorful. 127  
Thank you to the people of the dormitories where I lived at the Uji and Yoshida cam- 128  
puses. I am grateful to my Japanese language teachers. I also cherish the friends I met 129  
through my extracurricular activities, including Kendo, Table Tennis, Naginata, Karate, 130  
and Aikido. I also met many interesting people from various international student events. 131

I am honored to receive the Asian Future Leaders Scholarship Program (AFLSP) 132  
scholarship to support my studies in Japan. I have made a great choice by enrolling in 133  
Kyoto University Design School, which has provided me with many valuable interdisci- 134  
plinary experiences and opportunities to meet people outside my field. In this program, 135  
I have conducted fieldwork in Okinawa, Hong Kong, and Bali, a rare opportunity for 136  
researchers in computer science. I would also like to thank the Institute for Chemical 137  
Research (ICR) for the Research Assistant position in the Akutsu laboratory. 138

Finally, I would like to express my deepest gratitude to my family and my friends who 139  
have stayed by my side with their countless acts of support; I have nothing to return to 140  
them but my love and time. 141

A special acknowledgement goes to my niece. As you grow up, I hope you explore 142  
the world and fulfill your eagerness for knowledge. Find materials that interest you. One 143  
day, you might find this thesis online and, I hope, find it worth reading and inspiring. 144



# List of Publications

145

This thesis is based on the following papers.

146

- (Chapter 3) **Coleman Yu**, Raymond Chi-Wing Wong, and Tatsuya Akutsu, “MTSC-<sup>147</sup>  
Cleav: a Multivariate Time Series Classification (MTSC)-based Method for Predict-<sup>148</sup>  
ing Human Dicer Cleavage Sites”, submitted to *IEEE Access*, under review<sup>149</sup>
  - (Chapter 4) **Coleman Yu**, Tatsuya Akutsu, and Raymond Chi-Wing Wong, “Scal-<sup>150</sup>  
ing with Multiple Scaling Factors and Dynamic Time Warping in Time Series<sup>151</sup>  
Searching”, submitted to *IEEE Access*, under review<sup>152</sup>
  - (Chapter 5) **Coleman Yu**, Raymond Chi-Wing Wong, and Tatsuya Akutsu, “Lever-<sup>153</sup>  
aging Nearest Neighbors for Time Series Forecasting with Matrix Profile”, in prepara-<sup>154</sup>  
tion<sup>155</sup>
- Other publications<sup>156</sup>
- **Coleman Yu** and Raymond Chi-Wing Wong, “A Melody Composer for both Tonal<sup>157</sup>  
and Non-Tonal Languages”, the 43rd International Computer Music Conference<sup>158</sup>  
2017, Shanghai, China on 16-20 Oct, 2017<sup>159</sup>
  - Yi Zheng, Bogdan Enescu, Jiancang Zhuang, and **Coleman Yu**, “Data replenish-<sup>160</sup>  
ment of five moderate earthquake sequences in Japan, with semi-automatic cluster<sup>161</sup>  
selection”, *Earthquake Science*, 34:310-322, 2021<sup>162</sup>



# Contents

163

<b>Abstract</b>	<b>i</b>	164
<b>Acknowledgements</b>	<b>iii</b>	165
<b>List of Publications</b>	<b>vii</b>	166
<b>List of Figures</b>	<b>xiii</b>	167
<b>List of Tables</b>	<b>xv</b>	168
<b>1 Introduction</b>	<b>1</b>	169
1.1 Background . . . . .	1	170
1.2 Contributions . . . . .	2	171
1.3 Organization . . . . .	2	172
<b>2 Preliminaries</b>	<b>3</b>	173
2.1 Distance Measures . . . . .	3	174
2.1.1 Euclidean Distance (ED) . . . . .	4	175
2.1.2 Dynamic Time Warping (DTW) . . . . .	4	176
2.1.3 Derivative Dynamic Time Warping (DDTW) . . . . .	4	177
2.1.4 Weighted Dynamic Time Warping (WDTW) . . . . .	5	178
2.1.5 Weighted Derivative Dynamic Time Warping (WDDTW) . . . . .	6	179
2.1.6 Shape Dynamic Time Warping (shapeDTW) . . . . .	6	180
2.1.7 Amercing Dynamic Time Warping (ADTW) . . . . .	6	181
2.2 Classification . . . . .	7	182
2.2.1 Ridge Classifier . . . . .	7	183
<b>3 MTSCCleav: a Multivariate Time Series Classification (MTSC)-based Method for Predicting Human Dicer Cleavage Sites</b>	<b>9</b>	184
3.1 Background . . . . .	10	186
3.2 Methods . . . . .	12	187
3.2.1 Data Preparation . . . . .	13	188

189	3.2.2	Time Series Encoding . . . . .	16
190	3.2.3	Time Series Classification . . . . .	19
191	3.2.4	Evaluation Metrics . . . . .	23
192	3.3	Results . . . . .	24
193	3.3.1	Channel Ablation Study . . . . .	25
194	3.3.2	Predictive Performance . . . . .	26
195	3.3.3	Running Time Analysis . . . . .	28
196	3.3.4	Subsequence Importance . . . . .	29
197	3.3.5	Summary . . . . .	30
198	3.4	Discussion . . . . .	30
199	3.5	Concluding Remarks . . . . .	31
200	<b>4</b>	<b>Scaling with Multiple Scaling Factors in Time Series Searching</b>	<b>33</b>
201	4.1	Background . . . . .	34
202	4.2	Related Work . . . . .	37
203	4.3	Preliminaries . . . . .	37
204	4.3.1	Euclidean Distance (ED) . . . . .	38
205	4.3.2	Dynamic Time Warping (DTW) . . . . .	39
206	4.3.3	Uniform Scaling (US) . . . . .	41
207	4.3.4	Uniform Scaling & Dynamic Time Warping (USDTW) . . . . .	42
208	4.3.5	Lower Bounds for DTW and USDTW . . . . .	43
209	4.4	Piecewise Scaling Distance . . . . .	46
210	4.4.1	Piecewise Scaling & Dynamic Time Warping (PSDTW) . . . . .	47
211	4.4.2	Speedup Techniques . . . . .	49
212	4.4.3	Guided Distance . . . . .	54
213	4.5	Experiments . . . . .	54
214	4.5.1	Experimental Setup . . . . .	54
215	4.5.2	Experimental Results . . . . .	57
216	4.6	Concluding Remarks . . . . .	60
217	<b>5</b>	<b>Leveraging Nearest Neighbors for Time Series Forecasting with Matrix Profile</b>	<b>63</b>
218	5.1	Introduction . . . . .	63
219	5.2	Related Work . . . . .	66
220	5.3	Method . . . . .	67
221	5.3.1	Problem Formulation . . . . .	68
222	5.3.2	Evaluation Method . . . . .	68
223	5.3.3	Gradient Boosting Regression Tree (GBRT) . . . . .	70
224	5.3.4	Matrix Profile . . . . .	70

5.4	Experiments . . . . .	71	226
5.5	Conclusion and Future work . . . . .	72	227
5.5.1	Conclusion . . . . .	72	228
5.5.2	Future Work . . . . .	72	229
<b>6</b>	<b>Conclusion and Future Directions</b>	<b>75</b>	<b>230</b>



# List of Figures

231

3.1	Predicted secondary structure of the sequence $S$ of pri-miRNA “hsa-let-7a-1” <sup>1</sup> . Experimental evidence suggests that the two deviated mature miRNAs are $UGA \cdots GUU$ and $CUA \cdots UUC$ . They are $S(6 : 27)$ and $S(57 : 77)$ (Both ends are inclusive.). The ends are highlighted in <b>bold</b> . Since $S(6 : 27)$ ( $S(57 : 77)$ ) is near the 5' (3') end, we call it “5p (3p) mature miRNA”. The two scissors indicate the two cleavage sites. The color intensity of the nodes reflects their base-pair probability in this predicted secondary structure. The deeper the color, the higher the probability. The unpaired nodes are uncolored. The raw figure is generated by RNAfold web server <sup>2</sup> .	232 233 234 235 236 237 238 239 240 11 241
3.2	The overall pipeline of this study. Symbol notations: Cylinder - Dataset, Rectangle - Process, Parallelogram - Input / Output, Rounded Rectangle - Component.	242 243 13 244
3.3	Relationship of the proposed encoding methods.	16 245
3.4	Features generation in the transformation	20 246
3.5	Convolutions of HYDRA for each input time series with a set of random kernels $w$ , organized into $g$ groups with $k$ kernels each.	21 247 248
3.6	CD diagrams of channel ablation study.	26 249
3.7	CD diagrams to compare different classifiers.	27 250
3.8	CD diagrams to compare different encoding methods.	28 251
3.9	Results of the perturbation experiment.	30 252
4.1	Applying nearest neighbor interpolation on $Q$ , which result in Scaled $Q$ , that can better reflect its similarity with $C$ .	253 35 254
4.2	$Q$ and $C$ are in different rates. A stretching version of $Q$ is similar to a prefix of $C$ , but not the whole $C$ .	255 35 256
4.3	Intuition of piecewise scaling (PS).	36 257
4.4	Z-normalization. Resulting time series have mean = 0 and std = 1.	38 258
4.5	Visualization of $D$ with local constraints. The black cells form the warping path.	40 259 260
4.6	Visualization of $\text{LB}_{\text{Keogh}}$ and $\text{LB}_{\text{Shen}}$	44 261

262	4.7	Relationship of $L_Q$ and $L_C$ . . . . .	51
263	4.8	Visualization of the GunPoint dataset. Left (Right): A time series of the “Gun” (“Point”) scenario. Critical periods, such as “Aiming”, are annotated.	55
264	4.9	The red solid time series shows an instant in the target set. The blue dashed time series shows an instant in the query set. . . . .	55
265	4.10	Runtime and number of distance calls comparison of GunPoint dataset. (a)-(d) $P = 1$ , (e)-(h) $P = 2$ , (i)-(l) $P = 3$ . . . . .	59
266	5.1	Flattening a 2D window of size $(1 + M) \times w$ to a 1D vector of length $w + M$ . The resulting vector serves as the <i>predictor</i> for the regressor. Its expected <i>response</i> is the vector of length $h$ . The regressor learns from this predictor-response pair. . . . .	64
267	5.2	The <i>left</i> ( <i>right</i> ) matrix profile and the <i>matrix profile</i> of a time series. The <i>matrix profile</i> shows the distances between each $m$ -subsequence and its nearest neighbor, where $m$ is a user-given value. The <i>left</i> ( <i>right</i> ) matrix profile shows the same information but is limited to its left (right) nearest neighbor. For a particular $m$ -subsequence shown by the right gray box, its nearest neighbor is the left gray box, as indicated by the dashed line in the <i>left matrix profile</i> and the <i>matrix profile</i> . Similarly, the nearest neighbor of the left gray box is the right gray box, as indicated by the dashed line in the <i>right matrix profile</i> and the <i>matrix profile</i> . The first (last) point in each box is denoted by a <i>red</i> circle (triangle). $h$ denotes the length of the immediate subsequence of the nearest neighbor. Intuitively, this subsequence should be similar to the immediate subsequence (i.e., future) of the right gray box. To note, the <i>left</i> ( <i>right</i> ) matrix profile starts (ends) at a later (earlier) index because the corresponding nearest neighbor with length $m$ does not exist. . . . .	65
268			
269			
270			
271			
272			
273			
274			
275			
276			
277			
278			
279			
280			
281			
282			
283			
284			
285			
286			
287			

# List of Tables

288

3.1	Selected representative records from miRBase. For the last two columns, the first line shows the name, the second line shows its location in the original sequence, and the third line indicates whether its existence has experimental evidence. The selected one is highlighted in <b>bold</b> . . . . .	289 290 291 13 292
3.2	The whole sequence of “hsa-let-7a-1” and its predicted secondary structure by RNAfold. The corresponding positions of the two mature miRNAs and the probability of the unpaired “U” are highlighted in <b>bold</b> . . . . .	293 294 14 295
3.3	The first row shows the “four strings” of “hsa-let-7a-1”. Their complementary strands are shown in the second row. As a whole, they are referred to as the “eight strings”. . . . .	296 297 15 298
3.4	Time series encoding. $P$ is the corresponding base-pair probability sequence of $S$ . $p_i = 1$ if we encode $S$ without incorporating base-pair probability sequence. . . . .	299 300 18 301
3.5	Comparison of rocket-based classifiers [64]. $\mathcal{N}(0, 1)$ : a standard normal distribution, $U(0, 1)$ : a uniform distribution between 0 and 1, 1 <sup>st</sup> order difference: $\Delta T = t_2 - t_1, t_3 - t_2, \dots, t_n - t_{n-1}$ . . . . .	302 303 23 304
3.6	Channel ablation study. The best results are highlighted in <b>bold</b> . . . . .	25 305
3.7	Performance on the 45 combinations between encoding methods and the ROCKET-based classifiers. The best results are highlighted in <b>bold</b> . . . . .	306 27 307
3.8	Comparative analysis between MTSCCleav with the best combination of the encoding method and classifier, with the SOTA, DiCleave, on the three datasets. The best results of using MiniROCKET have also been shown to compare the computational efficiency. The best results are highlighted in <b>bold</b> . . . . .	308 309 310 311 28 312
4.1	Details of the ten datasets for the experiments . . . . .	56 313
4.2	The accuracy comparison for eight distance measures of the GunPoint dataset . . . . .	314 57 315
4.3	The accuracy comparison for six PSED-guided distance measures of the GunPoint dataset . . . . .	316 58 317
4.4	The accuracy comparison for eight distance measures of the ten datasets	60 318

319	4.5 The accuracy comparison for six PSED-guided distance measures of the	
320	ten datasets . . . . .	60
321	4.6 The number of distance calls and runtime on PSED_vanilla and PSED_parallel_bsf	
322	of the ten datasets . . . . .	61
323	5.1 Dataset Statistics. $N$ is the number of time series in the dataset, while	
324	$ T  = n$ is the length of each time series. “rate” refers to the measuring	
325	rate. $w$ is the size of the look-back window. $h$ is the size of the forecasting	
326	window, also known as the forecasting horizon. $T_{\text{train}}$ is the training subse-	
327	quence of $T$ . $T_{\text{test}}$ is the test subsequence of $T$ . To note, $ T_{\text{train}}  +  T_{\text{test}}  = n$ .	
328	. . . . .	71

# Chapter 1

329

## Introduction

330

### 1.1 Background

331

Human generates a ton of data nowadays. We are producing more new data in one single day today than in the first twenty-one centuries of AD combined. We are drowning in information but thirsty for knowledge. It is natural for us to develop computational methods to accelerate the process of “harvesting” knowledge from information.

332

333

334

335

Computational tasks focus on the relationship between input and output. We would like to find the hidden function behind. To note, there are two ways to solve a problem. One is the algorithmic approach, and the other is the machine-learning approach. In Chapter 3, it demonstrates a machine learning approach to analyze a biology problem. In Chapter 4, we solve an algorithmic problem on distance measure.

336

337

338

339

340

There are two large categories of machine learning. They are supervised learning and unsupervised learning. Classification may be the most intuitive form of supervised learning. The input is data points with labels. We learn a model from the relationship between data points and the labels. The model predicts the labels for the new data points. They have many applications. For example, in medical applications, it involves classifying patients as healthy or diseased, or tumors as benign or malignant. The term “supervised” means the model has access to labeled data. In other words, it requires labeled training examples that provide ground truth. So, the model can learn the boundary between the categories. Our first study focuses on a classification problem in biology.

341

342

343

344

345

346

347

348

349

A representative of unsupervised learning is undoubtedly clustering. We aim to group data into distinct clusters. The key difference is that the data lack predefined labels. By grouping them, we aim to identify natural patterns hidden in the data. One example is clustering cells based on their gene-expression profiles. These clusters might reveal distinct cell types. Note that we do not have the ground truth for the cluster set. In bioinformatics, we typically use enrichment analysis to determine whether specific gene functions are enriched in these clusters. Cell types often show enrichment for genes

350

351

352

353

354

355

357 responsible for specific functions. This set of genes defines their biological role. In  
358 clustering, we first need to define a measure of similarity between two objects. And  
359 what should be ignored. This is called invariance. For example, in image classification,  
360 it should be invariant with respect to the zooming effect and the rotation effect. In  
361 Chapter 4, we define a new distance measure framework that achieves invariance when  
362 two time series are in different scaling factors.

## 363 1.2 Contributions

364 In this study, our contributions mainly include two parts. First, we propose the usage  
365 of the base pair probability sequence from the predicted secondary structure of RNA se-  
366 quence as a new information for the classification task. We apply Rocket-based classifiers  
367 to identify the human dicer cleavage sites. Because of the simplicity of the transformation  
368 method and the classifiers, our proposed method achieves 3.7X to 28.8X speedup while  
369 achieving better or comparable results than the current state-of-the-art method. Second,  
370 we propose a new distance measure framework, namely PSD, that can incorporate any  
371 existing distance measures to achieve invariance for two time series with multiple rates.  
372 Experiments show that our methods outperform ED, DTW and the other five DTW-  
373 based methods. Besides, we propose to use the segmentation result returned by PSD to  
374 improve the accuracy of other distance measures.

## 375 1.3 Organization

376 In Chapter 2, we review some of the basic knowledge in biology and time series data  
377 mining, in particular, we focus on distance measures and Rocket-based classifiers. In  
378 Chapter 3, we introduce our study of the problem of predicting human dicer cleavage  
379 sites. We proposed a novel approach to frame this task as a multivariate time series  
380 classification problem by introducing nine encoding methods and making use of Rocket-  
381 based classifiers. In Chapter 4, we introduce a new distance measure framework, namely  
382 PSD. It releases the assumption that there is only one scaling factor existing throughout  
383 the whole time series. In Chapter 6, we give a conclusion to these two studies and provide  
384 future work on them.

# Chapter 2

385

## Preliminaries

386

In this chapter, we provide background on time series, with a focus on distance measures 387  
and classification, particularly the ridge classifier, which is used in the ROCKET-based 388  
classifiers for time series classification. The remaining preliminary knowledge will be 389  
provided in the corresponding chapters. Section 2.1 gives an overview of the existing 390  
distance measures used in the evaluation in Chapter 4. Section 2.2 reviews the additional 391  
knowledge about the classifiers used in Chapter 3. We start with the definition of a time 392  
series. 393

### 2.1 Distance Measures

394

A general form of a time series  $T$  is an ordered pair of  $n$  real-valued variables,  $T = 395$   
 $(b_1, c_1), (b_2, c_2), \dots, (b_n, c_n)$ , where  $b_i$  is the behavioral attribute and  $c_i$  is the contextual 396  
attribute, where  $1 \leq i \leq n$ .  $c_i$  refers to the time stamp at which the measurement  $b_i$  397  
is taken. Since the measurements are always taken in a uniform manner,  $t_i$  is simply 398  
incrementing from 1 to  $n$  uniformly. Hence, we can represent a time series more concisely 399  
as  $T = t_1, t_2, \dots, t_n$ , where  $t_i = b_i$ . 400

We may be interested not only in the entire time series but also in a segment of it, 401  
called a subsequence. A subsequence  $T(i : j)$  of a time series  $T$  is a shorter time series, 402  
which is a contiguous subset of time points in  $T$ , that starts from position  $i$  and ends at 403  
position  $j$ . Formally,  $T(i : j) = t_i, t_{i+1}, \dots, t_j$ , where  $1 \leq i \leq j \leq n$ . We call  $T(1 : m)$  as 404  
the prefix of length  $m$  of  $T$ ,  $m$ -prefix in short. 405

To quantify the similarity between two time series, we need to define a distance 406  
measure, also known as a similarity measure, between them. Many distance measures 407  
have been proposed in the literature. Among them, the most established measures are 408  
undoubtedly Euclidean Distance (ED) and Dynamic Time Warping (DTW). They are 409  
representatives of the two board classes of distance measures, namely “lock-step” and 410  
“elastic”. 411

### <sup>412</sup> 2.1.1 Euclidean Distance (ED)

<sup>413</sup> ED is a lock-step distance measure. Given two time series  $Q$  and  $C$  with the same length  
<sup>414</sup>  $n$ , it compares the time point  $q_i$  of  $Q$  with the time point  $c_i$  of  $C$  at the same time (index).  
<sup>415</sup> Note that, traditionally, lockstep distance measures require the two time series to have  
<sup>416</sup> the same length because of the one-to-one alignment. However, in the setting of query by  
<sup>417</sup> content, where it is always the case that  $|Q| < |C|$ , we can still apply a lock-step distance  
<sup>418</sup> measure by either comparing  $Q$  with  $C(1 : |Q|)$  or padding  $Q$  using its last element to  
<sup>419</sup> lengthen it to the same length of  $C$ . The general form of ED is the Minkowski distance.  
<sup>420</sup> It is the  $L_p$ -norm of the difference between the two time series  $X$  and  $Y$ .

$$D(X, Y) = \left( \sum_{i=1}^n |x_i - y_i|^p \right)^{\frac{1}{p}} \quad (2.1)$$

<sup>421</sup> When  $p = 2$ , it corresponds to the Euclidean distance. When  $p = 1$ , it corresponds to  
<sup>422</sup> the Manhattan distance. When  $p = \infty$ , it corresponds to the Chebyshev distance. In our  
<sup>423</sup> studies, we focus on the Euclidean distance. Other lock-step distance measures include  
<sup>424</sup> Pearson correlation distance. It accounts for the linear association between the two time  
<sup>425</sup> series using the Pearson correlation coefficient.

### <sup>426</sup> 2.1.2 Dynamic Time Warping (DTW)

<sup>427</sup> Dynamic Time Warping is an elastic measure [74]. In contrast to lock-step distance mea-  
<sup>428</sup> sures, elastic distance measures allow one-to-many point matching. The one-to-many  
<sup>429</sup> point matching allows the elastic distance measures to warp in the time axis (i.e., tem-  
<sup>430</sup> porally) such that it can handle the local temporal distortions. While it will be detailed  
<sup>431</sup> in Chapter 4, it is briefly explained here. In short, it minimizes the cumulative distance  
<sup>432</sup> between two time series, subject to constraints, by finding an optimal warping path  $W^*$   
<sup>433</sup> in a cost matrix, where  $W$  is the set of all possible paths and  $W^*$  is the optimal one. The  
<sup>434</sup> constraints typically are (1) Boundary conditions, (2) Continuity, and (3) Monotonicity.  
<sup>435</sup> Note that we can reduce pathological warping and accelerate computation by introduc-  
<sup>436</sup> ing a warping window. DTW with a warping window constraint is called constrained  
<sup>437</sup> DTW (cDTW). Two famous windows are the Sakoe-Chiba band [74] and the Itakura  
<sup>438</sup> parallelogram [39]. In the study, we focus on the Sakoe-Chiba band.

### <sup>439</sup> 2.1.3 Derivative Dynamic Time Warping (DDTW)

<sup>440</sup> The Derivative Dynamic Time Warping (DDTW) is a variant of DTW [45]. Instead of  
<sup>441</sup> comparing original raw values, it compares two time series using their first-order deriva-  
<sup>442</sup> tives, but with an approximation. In DTW, a point on a rising trend may be mapped to  
<sup>443</sup> a point on a falling trend. It goes against our intuition. It can be solved by comparing

their first-order derivatives, which encodes the slope information. The derivative  $T'$  of a time series  $T$  is computed approximately as follows.

$$t'_i = \frac{(t_i - t_{i-1}) + \frac{t_{i+1} - t_{i-1}}{2}}{2} \quad (2.2)$$

This estimate is simply the average of “the slope of the line through  $t_i$  and  $t_{i-1}$  (i.e., its left neighbor)” and “the slope of the line through  $t_{i-1}$  (i.e., its left neighbor) and  $t_{i+1}$  (i.e., its right neighbor)”. The  $1/2$  term in the second item of the numerator comes from the fact that the separation in time of the  $t_{i-1}$  and  $t_{i+1}$  is 2. Note that the estimate is not defined for the first and last elements of the time series in the above equation. In these boundary cases, we use the estimates of the second and penultimate (i.e., the second-to-last thing) as the estimates for the first and last elements, respectively.

#### 2.1.4 Weighted Dynamic Time Warping (WDTW)

The Weighted Dynamic Time Warping (WDTW) is a variant of DTW [40]. It is a penalty-based DTW designed to prevent pathological paths. Recall that a warping window (e.g, Sakoe-Chiba band) is enforced on the cost matrix of DTW, such that some paths are excluded. Only the paths that reside entirely in the warping window are feasible. This constraint may be too strict. WDTW uses a softer way for the same purpose. Instead of using a window to forbid the alignment of  $x_i$  and  $y_j$  that are far away in time. WDTW weights the cost of such alignment by multiplying it by a modified logistic weight function (MLWF)  $\omega(k)$ , defined as follows.

$$\omega(k) = \frac{\omega_{\max}}{1 + \exp(-g \cdot (k - m_c))} \quad (2.3)$$

Where:

- $k = |i - j|$ . It is the phase difference (i.e., distance on the time axis from the diagonal. The diagonal refers to the line where  $i = j$ .)
- $\omega_{\max}$  is the desired upper bound for the weight parameter, which is suggested to be set to 1.
- $m_c$  is the midpoint of a sequence.  $m_c = m/2$ .
- $g$  is a constant that controls the level of penalization. It controls the curvature (slope) of the function.

Intuitively, if  $x_i$  and  $y_j$  are far apart temporally, it will have a larger weight to discourage their alignment and vice versa.

### 472 2.1.5 Weighted Derivative Dynamic Time Warping (WDDTW)

473 [40] also proposed the weighted version of DDTW. In brief, a weight is applied to the  
474 local cost function when computing DTW on the first derivative.

### 475 2.1.6 Shape Dynamic Time Warping (shapeDTW)

476 The Shape Dynamic Time Warping (shapeDTW) is a variant of DTW [100]. The main  
477 modification to the original DTW is the way the local distance between points is com-  
478 puted. Recall that DTW compares single scalar points. shapeDTW compares local  
479 descriptors. The local descriptors are constructed using a sliding window on the original  
480 series, such that for each point  $x$ , a  $L$ -subsequence with  $x$  as the center is extracted to  
481 compute the higher-level feature of  $x$ .  $L$  is the user-given length of the subsequence to  
482 consider. By default, it is set to 15. There are several ways to construct such a de-  
483 scriptor. For example, a raw subsequence (i.e., a set of neighbor points surrounding the  
484 point of interest), Piecewise aggregate approximation (PAA) [42, 96], slope, derivative,  
485 HOG-1D [99].

486 Then, the distance between descriptors is calculated rather than between raw values.  
487 When a raw subsequence is chosen to construct the local descriptors, a common metric  
488 used for comparing two local descriptors is the Euclidean distance. In the evaluation, a  
489 raw subsequence is chosen to construct the local descriptors.

### 490 2.1.7 Amercing Dynamic Time Warping (ADTW)

491 The Amercing Dynamic Time Warping (WDTW) is a variant of DTW [37]. It is also  
492 designed to constrain the amount of warping, as in cDTW and WDTW. While cDTW  
493 imposes a hard window and WDTW uses multiplicative weights (i.e, MLWF), ADTW  
494 introduces an additive penalty for non-diagonal alignment. The word “Amercing” means  
495 “fining”. The non-diagonal alignments are required to pay the fines. Unlike WDTW,  
496 which uses a multiplicative weight based on the position of the alignment, ADTW applies  
497 an additive penalty  $\omega$  based on the action of warping. The non-diagonal alignments are  
498 penalized. Formally, the recursive relation for ADTW is defined as:

$$D(i, j) = d(q_i, c_j) + \min \begin{cases} D(i - 1, j - 1), \\ D(i - 1, j) + \omega, \\ D(i, j - 1) + \omega \end{cases} \quad (2.4)$$

ADTW penalizes the last two alignment actions.  $\omega$  is a user-given hyperparameter. 499  
 It should be a non-negative scalar constant. In practice, it is defined through cross- 500  
 validation, which determines the optimal  $\omega$  by training on a subset of data or heuristic 501  
 search, which searches values in a user-given range. 502

To note, ADTW generalizes ED and DTW. If  $\omega = 0$ , no need to pay the fine for the 503  
 non-diagonal alignment, which reduces to DTW. If  $\omega \rightarrow \infty$ , the non-diagonal alignment 504  
 becomes prohibitive, and it reduces to ED. 505

## 2.2 Classification 506

In Chapter 3, we use ROCKET (RandOm Convolutional KErnel Transform) and its 507  
 variants, including MiniRocket, MultiRocket, and Hydra, as the time series classifiers on 508  
 the time series resulting from our encoding methods. Technically, they are not classifiers 509  
 in their own right but rather feature extractors. These features are also called summary 510  
 statistics. They are high-dimensional feature vectors that capture the characteristics of 511  
 the original time series. The summary statistics are then fed to the classifiers to output 512  
 the final classification results. 513

### 2.2.1 Ridge Classifier 514

The classifier that is usually chosen to work with ROCKET and its variants is a ridge 515  
 classifier. The main advantage of it is speed. ROCKET and its variants generate a large 516  
 number of features. 517

A ridge classifier is a wrapper that uses a ridge regression model as a routine to perform 518  
 classification. It first maps the categorical labels of targets into continuous numbers, does 519  
 the regression, and finally thresholds the numerical results from the regressor to obtain 520  
 the classification result. 521

Given a training dataset  $D = \{(x_i, y_i)\}_{i=1}^n$  with  $n$  instances, where  $x_i \in \mathbb{R}^P$  is the 522  
 feature vector with  $P$  dimensions and  $y_i \in \{+1, -1\}$  is its label, it minimize the following 523  
 optimization function. 524

$$\min_w \left( \sum_{i=1}^n (x_i^T w - y_i)^2 + \lambda \|w\|_2^2 \right) \quad (2.5)$$

Where  $\|w\|_2^2 = \sum_{j=1}^P w_j^2$  is the  $L_2$  norm of the weight vector and  $\lambda > 0$  control the 525  
 penalty. We explain the equation in brief. There are two terms inside the bracket. The 526  
 first term is simply the sum of the residual, same as the one in the least squares method. 527  
 The second term is called the  $L_2$  penalty and is used to introduce bias in the fit to avoid 528  
 overfitting. Hence,  $\lambda$  serves as a regularization hyperparameter between the trade-off 529  
 between bias and variance. 530

531 Since the above optimization function in a ridge classifier has a closed-form solution,  
532 it can be solved using linear algebra rather than iterative optimization, as in logistic  
533 regression. Besides, the generated features by the random kernels in ROCKET and its  
534 variants are highly correlated. Ridge regularization, also known as the  $L_2$  norm, can  
535 handle this case. Ridge regression shrinks regression coefficients toward zero by adding  
536 an L2 penalty. It reduces model complexity and helps with multicollinearity.

# Chapter 3

537

## MTSCCleav: a Multivariate Time Series Classification (MTSC)-based Method for Predicting Human Dicer Cleavage Sites

538

539

540

541

MicroRNAs (miRNAs) are small non-coding RNAs (ncRNAs) that regulate gene expression at the post-transcriptional level, thereby playing essential roles in diverse biological processes. The biogenesis of miRNAs requires dicer to cleave at specific sites on the precursor miRNAs (pre-miRNAs). Several machine learning approaches have been proposed to predict whether an input sequence contains a cleavage site. However, they rely heavily on complex feature engineering or opaque deep neural networks. It results in a lack of generalizability and a long running time. There is a need for an alternative modeling paradigm that is accurate, fast, and simple.

542

543

544

545

546

547

548

549

We proposed a novel approach to frame the task as a multivariate time series classification problem. Nine encoding methods have been proposed to convert the sequence and the predicted secondary structure into a time series. We also leveraged the probabilities of the base pairs in the predicted secondary structure. Computational experiments demonstrate that our proposed method can achieve better or comparable results in terms of using a simpler, more intuitive model and less computational time. It achieves 3.7X to 28.8X speedup. Through perturbation experiments, we found that regions close to the center of pre-miRNAs are essential for predicting human dicer cleavage sites.

550

551

552

553

554

555

556

557

By transforming the RNA sequence and its secondary structure information into a time series and utilizing simple, state-of-the-art time series classifiers, we achieved comparable or even superior performance in a simpler and faster manner.

558

559

560

Code is available at: <https://github.com/colemanyu/time-series-classification-cleavage>.

561

562

563 **3.1 Background**

564 One of the most important theories in molecular biology is the central dogma. It depicts  
565 the flow of genetic information [89, 6]. Proteins are the functional units. The information  
566 stored in DNA is used to create them. Genes (segments) in DNA are used as templates for  
567 messenger RNAs (mRNAs) synthesis. An mRNA acts as a set of instructions to assemble  
568 a chain of amino acids, which form a linear polypeptide. To become biologically active,  
569 this chain is folded into a specific 3D structure, a proper configuration that enables it to  
570 perform its desired functions. This folded polypeptide is called a functional protein, or  
571 simply a protein. This entire process closely resembles how a computer program runs on  
572 a machine. The source code does not function by itself. First, it is translated into an  
573 assembly code (a lower-level, less human-readable form) and then into an executable file  
574 that can actually perform the intended tasks [18].

575 These mRNAs are called “coding RNAs” because they code for proteins. There are  
576 other genes in which the final product is the RNA molecule itself. They are called  
577 non-coding RNAs (ncRNAs). Two types of small ncRNAs are particularly important.  
578 They are microRNAs (miRNAs) and small interfering RNAs (siRNAs). Their discovery  
579 was recognized with the 2006 Nobel Prize in Physiology or Medicine<sup>1</sup>, awarded for work  
580 completed only eight years prior [89].

581 In this study, we focus on miRNAs. An miRNA can regulate the expression of several  
582 proteins. Hence, understanding the biogenesis of miRNAs is of great value. It involves  
583 the processing of primary miRNAs (pri-miRNAs). RNAs are 3D molecules. However, it  
584 is hard to measure the 3D structure (tertiary structure) from the experiment and predict  
585 it from 1D sequence. We can understand their properties by analyzing their 1D sequence  
586 or 2D structure, known as secondary structure. RNA sequence is easily obtained through  
587 sequencing. The sequence and its predicted secondary structure of a pri-miRNA “hsa-  
588 let-7a-1” is shown in Figure 3.1.

589 Recall that a pri-miRNA contains a hairpin loop, also called a stem loop. A mi-  
590 croprocessor complex comprising Drosa and DCGR8 cleaves the pri-miRNA to form a  
591 precursor miRNA (pre-miRNA) inside the nucleus. The stem-loop is still preserved, but  
592 the two arms become shorter. After that, the pri-miRNA is transported by Exportin 5  
593 from the nucleus to the cytoplasm. It is further cleaved by an enzyme called dicer [50].  
594 Dicer cleaves the stem-loop from the two arms at the two cleavage sites, shown as the two  
595 scissors in Figure 3.1. The stem-loop is removed. It results in a short double-stranded  
596 miRNA molecule, known as an miRNA duplex, which consists of the 5p strand and the

---

<sup>1</sup>The Nobel Prize in Physiology or Medicine 2006 - NobelPrize.org:  
<https://www.nobelprize.org/prizes/medicine/2006/summary/> (Accessed on: 2025-06-13).

<sup>2</sup>Its miRBase entry: <https://mirbase.org/hairpin/MI0000060>. (Accessed on: 2025-06-12).

<sup>3</sup>RNAfold web server: <http://rna.tbi.univie.ac.at/cgi-bin/RNAWebSuite/RNAfold.cgi>. (Accessed on: 2025-06-12). The figure is viewed in “forna”. This view option can be chosen on the website.

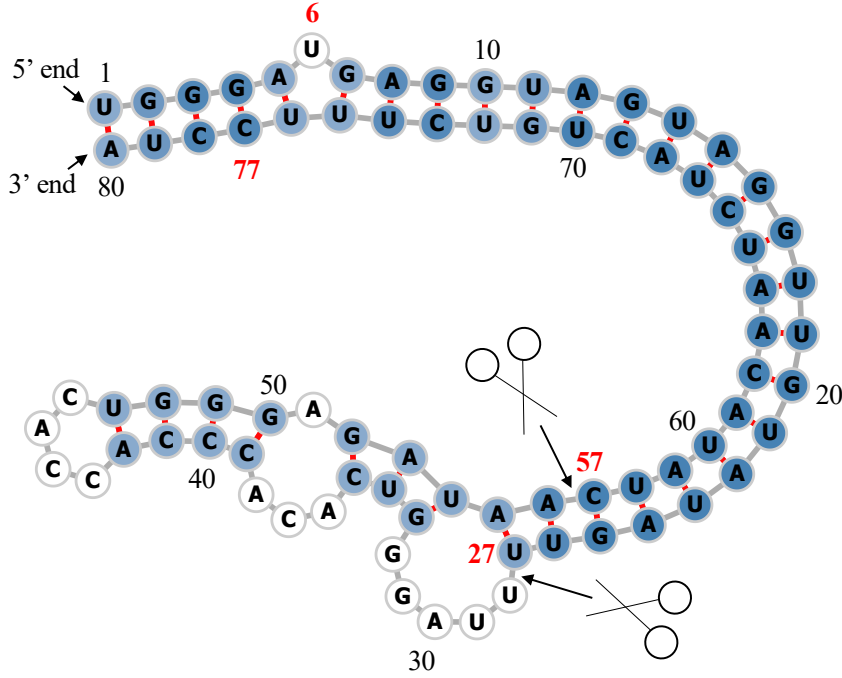


Figure 3.1: Predicted secondary structure of the sequence  $S$  of pri-miRNA “hsa-let-7a-1”<sup>2</sup>. Experimental evidence suggests that the two deviated mature miRNAs are  $UGA \cdots GUU$  and  $CUA \cdots UUC$ . They are  $S(6 : 27)$  and  $S(57 : 77)$  (Both ends are inclusive.). The ends are highlighted in **bold**. Since  $S(6 : 27)$  ( $S(57 : 77)$ ) is near the 5' (3') end, we call it “5p (3p) mature miRNA”. The two scissors indicate the two cleavage sites. The color intensity of the nodes reflects their base-pair probability in this predicted secondary structure. The deeper the color, the higher the probability. The unpaired nodes are uncolored. The raw figure is generated by RNAfold web server<sup>3</sup>.

3p strand<sup>4</sup>. These molecules may be subjected to additional trimming. The miRNA duplex is loaded into an RNA-induced silencing complex (RISC). RISC unwinds the duplex and tends to retain the strand with the less stable 5' end as the guide strand. The other strand is called the passenger strand. The retained strand guides the RISC to silence the target mRNA. Note that both strands can become the guide strand.

Dicer plays an important role in the biogenesis of miRNAs. It is reasonable to argue that the structure of the pre-miRNAs informs dicer about the cleavage process. It would be of great benefit to understand how dicer selects cleavage sites from the neighborhood information near the cleavage sites. Studies [36, 29, 58] revealed that the secondary structures are essential for cleavage site determination. Hence, to predict or classify whether a subsequence, extracted from the sequence of a pri-miRNA, contains a cleavage site, we can make use of both the sequence and secondary structure information. PHDcleav employed support vector machines (SVM), leveraging sequence and structure-based features for the classification [3]. LBSsizeCleav improved upon it by considering the loop and bulge

<sup>4</sup>The 5p strand comes from the 5' arm while the 3p strand comes from the 3' arm. For the directionality, the 5p (3p) strand retains the original 5' (3') end of the pre-miRNA.

lengths [9]. [56] proposed an ensemble learning approach, using a gradient boosting machine for better accuracy. [66] developed a deep learning model, namely DiCleave. This model used an autoencoder to learn the secondary structure embeddings of pre-miRNAs from all the species in the miRBase database and leveraged this information. All these methods begin with curated pre-miRNA sequences from the miRBase database. Their secondary structures are predicted. Patterns are extracted from the sequence and the secondary structure. They create the positive cleavage patterns by setting the cleavage sites at the middle of the patterns. The follow-up work of [66], which created the cleavage pattern by allowing cleavage sites to appear at any position within the pattern, instead of the middle only [65]. It created a much larger dataset. This increased dataset facilitates the learning of the deep learning method at the cost of increased running time. We utilized the original dataset setting [3, 9, 56, 66]. DiCleave is the current state-of-the-art (SOTA) for this problem with the original dataset setting.

These models suffer several limitations. They rely heavily on complicated feature engineering or opaque deep learning models [56, 66, 65]. It results in a lack of generalizability and a long running time. There is a need to design a simpler model so that it can be easily extended to other prediction tasks on RNA data. One way to analyze sequence data is to transform it into time series data. In response to this, we proposed a multivariate time series classification-based method. Our contributions are shown as follows.

1. To the best of our knowledge, we are the first to frame the prediction of the cleavage sites as a multivariate time series classification problem.
2. We introduced several encoding methods to convert RNA data to time series.
3. We proposed utilizing the base-pair probabilities in the predicted secondary structure for the prediction. To our surprise, this information has been ignored in the existing studies.
4. For computational efficiency, our method achieves a 3.7X to 28.8X speedup compared to the state-of-the-art (SOTA).
5. We conducted perturbation-based experiments. It shows that regions close to the cleavage sites are important for this problem. It is consistent with the existing study [56].

## 3.2 Methods

The overall pipeline of this study is summarized in Figure 3.2.

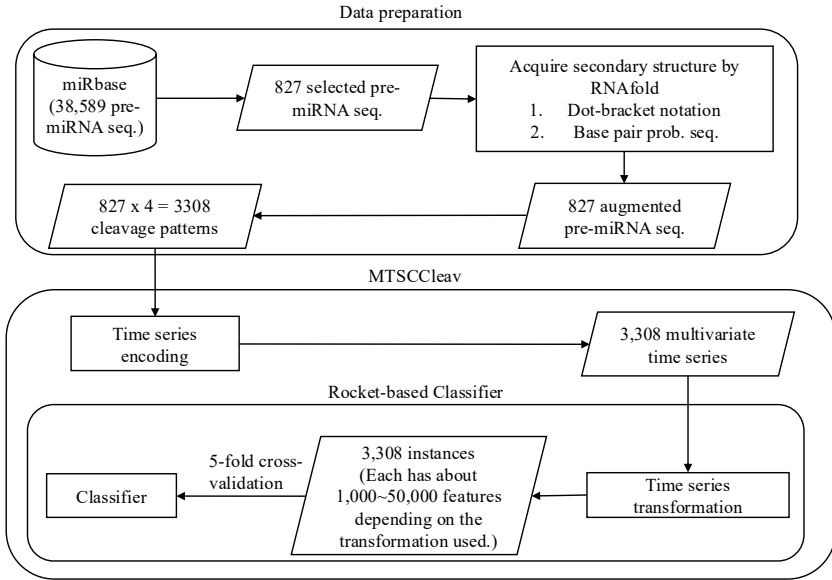


Figure 3.2: The overall pipeline of this study. Symbol notations: Cylinder - Dataset, Rectangle - Process, Parallelogram - Input / Output, Rounded Rectangle - Component.

### 3.2.1 Data Preparation

644

Accession	Name	Organism	Sequence	Mature miRNA 1	Mature miRNA 2
MI0000001	cel-let-7	<i>Caenorhabditis elegans</i>	<i>UACAC</i> … <i>UUCGA</i>	cel-let-7-5p 17:38 experimental	cel-let-7-3p 60:81 experimental
<b>MI0000060</b>	hsa-let-7a-1	<i>Homo sapiens</i>	<i>UGGGA</i> … <i>UCCUA</i>	hsa-let-7a-5p 6:27 experimental	hsa-let-7a-3p 57:77 experimental
MI0000114	hsa-mir-107	<i>Homo sapiens</i>	<i>CUCUC</i> … <i>ACAGA</i>	hsa-miR-107 50:72 experimental	NA
MI0000238	hsa-mir-196a-1	<i>Homo sapiens</i>	<i>GUGAA</i> … <i>UUCAC</i>	hsa-miR-196a-5p 7:28 experimental	hsa-miR-196a-1-3p 45:65 not experimental

Table 3.1: Selected representative records from miRBase. For the last two columns, the first line shows the name, the second line shows its location in the original sequence, and the third line indicates whether its existence has experimental evidence. The selected one is highlighted in **bold**.

We used miRBase database [35]<sup>5</sup>. The database comprises miRNA data from various organisms [92]. The database contains 38,589 miRNA records. Each record refers to an miRNA sequence, along with other properties such as name, accession, organism, and information on its derivative miRNA products. We are interested in pri-miRNA in humans. The derivative miRNA products are the mature miRNAs. The database also annotates the location of the mature miRNA within the original sequence and indicates whether its existence has experimental evidence.

645

646

647

648

649

650

651

<sup>5</sup>The website is [www.mirbase.org](http://www.mirbase.org), and the newest version of the database is Release 22.1 (Accessed on 2025-06-22).

652 Table 3.1 shows its four representative records. We first selected the records from  
 653 humans (*Homo sapiens*). It resulted in 1,917 records. To identify the actual locations of  
 654 the two cleavage sites in the pri-miRNA sequence supported by experimental evidence, we  
 655 selected records that have two mature miRNAs resulting from cleavage at the 5p arm and  
 656 the 3p arm, both of which have experimental support. Hence, only “MI0000060” (“hsa-  
 657 let-7a-1”) would be selected in the table. It would serve as our running example. Its whole  
 658 sequence is listed in Table 3.2. After the selection process, we selected 827 experimental  
 659 validated pre-miRNA sequences, each with its two mature miRNA products. This formed  
 660 our dataset.

Sequence	Secondary Structure (In Dot-bracket notation)
1 UGGGA <b>UGAGGUAGUAGGUUGUAUAGUU</b> 27 28 UUAGGGUCACACCCACCACUGGGAGAU 54 55 AA <b>CUAUACAAUCUACUGUCUUUC</b> CUA 80	1 (((((.((((((((((((( 27 28 UUAGGGUCACACCCACCACUGGGAGAU 54 55 ))))))))))))))))))))) 80
Base-pair probabilities sequence (the first 10 bases)	
1 (0.549, 0.946, 0.987, 0.987, 0.904) 5 6 ( <b>0.000</b> , 0.841, 0.974, 0.981, 0.890) 10	

Table 3.2: The whole sequence of “hsa-let-7a-1” and its predicted secondary structure by RNAfold. The corresponding positions of the two mature miRNAs and the probability of the unpaired “U” are highlighted in **bold**.

## 661 Augment the Dataset with Secondary Structure Information

662 We leveraged the predicted secondary structure of these sequences to enhance the ac-  
 663 curacy of the classification. Recall that a specific three-dimensional (3D) structure is  
 664 required for DNA, RNA, and protein to perform functions [104]. However, finding these  
 665 3D structures using experimental methods such as X-ray crystallography or nuclear mag-  
 666 netic resonance (NMR) is costly and time-consuming. Hence, prediction methods for such  
 667 3D structures are necessary and helpful for downstream analysis. However, predicting  
 668 the 3D structures is challenging. One of the reasons is that there are some “noncon-  
 669 ventional” base-pair interactions (e.g., noncanonical and rare A-G) that allow an RNA  
 670 sequence to fold into a 3D structure, in addition to the (G, U) wobble pair, which is  
 671 common and functionally important in RNA secondary structures. It makes the search  
 672 space for prediction much larger than, in the 2D case, the secondary structure. The local  
 673 structures of the 3D structures, the secondary structures, only focus on the conventional  
 674 base-pair interactions [6]. Hence, predicting secondary structures is easier and faster. We  
 675 employed RNAfold from the ViennaRNA Package<sup>6</sup> to predict the secondary structure for  
 676 a given pri-miRNA  $S$  [57]. RNAfold returns the secondary structure in the dot-bracket  
 677 notation and a matrix of base-pair probabilities. The matrix is a square matrix with the  
 678 side length  $|S|$ , where each entry  $m_{ij}$  is the probability of base  $s_i$  paired up with base  $s_j$ .

<sup>6</sup>The latest stable release is Version 2.7.0 (Accessed on 2025-06-22).

Dot-bracket notation is a way of representing the secondary structure of  $S$ . Open parentheses “(” (Close parentheses “)” ) indicates that the base is paired with a complementary base further (earlier) along in  $S$ . Dot “.” indicates that the base is unpaired. Equipped with the matrix, we can construct the base-pair probability sequence of  $S$ . The predicted secondary structure and the base-pair probability sequence of our running example are shown in Table 3.2. 679  
680  
681  
682  
683  
684

## Extract Cleavage Patterns 685

The locations of the two mature miRNAs on the whole sequence indicate the probable 686 locations of the two cleavage sites. The 5p cleavage site must be beyond and near the 687 ending location of the 5p mature miRNA. We deemed the immediate bond next to the 688 5p mature miRNA’s ending position the 5p cleavage site, with the knowledge that the 689 actual cleavage site may not be this immediate bond but rather the nearby bonds after 690 it. The same applies to the 3p cleavage site. It is located at the immediate bond before 691 the starting position of the 3p mature miRNA. 692

For each arm of each whole sequence, we extracted a 14-string<sup>7</sup> with the cleavage 693 site located at the center of the string. The first 7 nt (nucleotide) before the center are 694 highlighted in **bold**. In our running example, it would be “**UAUAGUU**UUAGGU” for 695 the 5p cleavage site and “**GAGAUAA**CUAUACA” for the 3p cleavage site. We refer to 696 these 14-strings as cleavage patterns. We also generate non-cleavage patterns by selecting 697 a 14-string with the center 6 nt away from the corresponding cleavage sites towards the 698 corresponding mature miRNA [9, 56] for each arm of each whole sequence. So, in our 699 running example, the 5p non-cleavage pattern would be “**AGGUUGU**AUAGUUU”. 700 The 3p non-cleavage pattern would be “**ACUAUAC**AAUCUAC”. 701

In conclusion, for a given pri-miRNA sequence, we can generate two cleavage patterns 702 and two non-cleavage patterns. We call these four patterns simply the “four strings” of 703 a given pri-miRNA. We also call each string a strand. The “four strings” of our running 704 example are listed in Table 3.3. 705

	5p cleav	5p non-cleav	3p cleav	3p non-cleav
Input strand	<b>UAUAGUU</b> UUAGGU	<b>AGGUUGU</b> AUAGUUU	<b>GAGAUAA</b> CUAUACA	<b>ACUAUAC</b> AAUCUAC
Complementary strand	AUAUCAA____UA	UCUAACAUAAUCAA_	C_CUGUUGAU AUGU	UGAUAUGUUGGAUG

Table 3.3: The first row shows the “four strings” of “hsa-let-7a-1”. Their complementary strands are shown in the second row. As a whole, they are referred to as the “eight strings”.

We can construct the complementary strand of each of the strands in the “four strings” 706 by finding the corresponding paired base for each of the bases in the input strand by 707 considering the secondary structure information. We use “\_” to denote the unpaired base 708

<sup>7</sup>String with length = 14.

in the complementary strand. For example, in Figure 3.1, “UUAGG” in the 5p cleavage pattern is unpaired, while other bases pair with some bases, the resulting complementary strand is “AUAUCAA\_\_\_\_\_UA”. There is a loop/budge there. We refer to the “four strings” and the four complementary strands together as the “eight strings” of the input pre-miRNA. It is also shown in Table 3.3.

### 3.2.2 Time Series Encoding

A *time series*  $T = t_1, t_2, \dots, t_n$  is a sequence of real-valued numbers<sup>8</sup>. A short contiguous region of  $T$  is called a subsequence. A *subsequence*  $T(i : j) = t_i, t_{i+1}, \dots, t_j$  of a time series  $T$  is a shorter time series that starts from position  $i$  and ends at position  $j$ , where  $i < j$ .

Strings and time series are temporal sequences. The difference between strings and time series lies in their behavioral attributes [1]. For strings, an entry is a letter from a predefined set called the *alphabet*. For example, the alphabet is  $\{A, C, G, T\}$  in the DNA string, while  $\{A, C, G, U\}$  in the RNA string. For time series, an entry is a real number. Unlike real numbers, there is no ordering in the alphabet unless some external domain knowledge is introduced.

The study of applying signal processing techniques to genomic data is called “Genomic Signal Processing” (GSP) [62, 7]. In the field of GSP, the time series representations of DNA strings are referred to as DNA numeric representations (DNR). Many DNRs have been proposed. We noted that DNA strings and RNA strings are equivalent from a computational standpoint. Many transformation methods designed for DNA can be applied to RNA by simply substituting  $T$  with  $U$ . We present nine encoding methods. The relationship among them is shown in Figure 3.3.

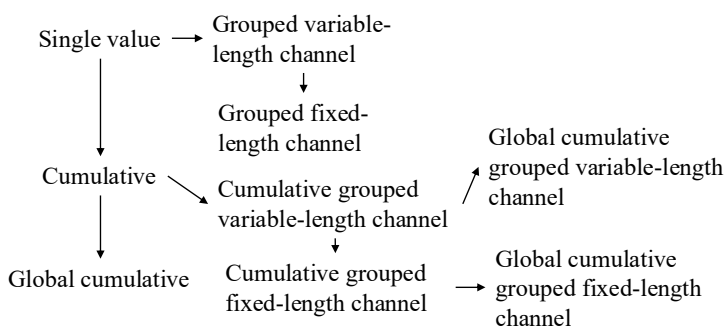


Figure 3.3: Relationship of the proposed encoding methods.

#### Single Value versus Cumulative

One of the simple, if not the simplest, encoding is to map the letters into numbers. Domain knowledge can be utilized. This approach is called the “Single value map-

<sup>8</sup>Unless otherwise specified, we denote entries of a time series (e.g.,  $T$ ) using the corresponding lowercase letter (e.g.,  $t$ ).

ping” [69, 19, 14, 101, 62]. One single value is assigned to each of the letters. [38] employed the atomic number of each nucleotide as the transformed values, where  $\{G = 78, A = 70, C = 58, T = 66\}$ . [68] used electron-ion interaction potential representation (EIIP) as such value, where  $\{G = 0.0806, A = 0.1260, C = 0.1340, T = 0.1335\}$ . Our goal is to transform the input strand and its complementary strand into time series, aiming to capture the information contained in these sequences and the secondary structure implied by them. We employed the following reasoning to assign the value:

1. We employ the complementary property [4, 14] during encoding. Recall that in the base-pairing rules,  $G$  pairs with  $C$  to form three hydrogen bonds while  $A$  pairs with  $U^9$  to form two hydrogen bonds.  $G-C$  pairs are more stable than  $A-U$  pairs.  $G$  ( $U$ ) can be regarded as the “inverse” of  $C$  ( $A$ ). We can preserve these base-pairing rules in the encoding by assigning  $G$  ( $A$ ) and  $C$  ( $U$ ) opposite values.
2.  $G$  and  $A$  have a two-ring structure. They are purines.  $C$  and  $U$  have a single-ring structure. They are pyrimidines. Hence, we put  $G$  and  $A$  ( $C$  and  $U$ ) on the same side of the number line with zero in the middle.
3. The lower stability of  $A-U$  pairs promotes strand separation, thereby facilitating the unwinding of the miRNA duplex during RISC loading. Regions rich in  $A$  and  $U$  are thus more likely to undergo strand selection and cleavage events. We assigned  $A$  ( $U$ ) with a larger absolute value than  $G$  ( $C$ ) to reflect this functional relevance. It aims to highlight sequence regions with higher cleavage potential.

It results in our baseline transformation method, namely “Single value mapping” as shown in row 1 of Table 3.4.  $S$  is the input strand. When we encode  $S$  without incorporating the corresponding base-pair probability sequence  $P$ , we set  $p_i = 1$  for all the entries of  $P$ . We use the first ten nucleotides of the complementary strand of the 3p cleav of “hsa-let-7a-1”, as shown in Table 3.3 as  $S$  in the examples in Table 3.4.

With the assigned value to each nucleotide defined in single-value mapping, we can compute a cumulative sum of those values over time. It captures the aggregated signal by accumulating past events, allowing us to focus on the trend [98, 11]. We named this method as “Cumulative mapping”, shown in row 4 of Table 3.4.

## Grouped Variable-Length Channel versus Grouped Local-Length Channel

We can transform the input strand into a multivariate time series with two channels using grouped binary encoding, where nucleotides are grouped into  $(A, U)$  and  $(G, C)$ . It releases our third assumption that  $A$  ( $U$ ) has a larger absolute value than  $G$  ( $C$ ). We proposed two variations. The first one allows the output to be variable-length sequences

---

<sup>9</sup>In DNA,  $A$  pairs with  $T$ .

	Encoding	Algorithm	Example
1	Single value mapping [69, 19, 14, 101, 62]	$\text{for } i = 1 \text{ to }  S :$ $t_i = \begin{cases} 2 \cdot p_i & \text{if } s_i = A \\ 1 \cdot p_i & \text{if } s_i = G \\ -1 \cdot p_i & \text{if } s_i = C \\ -2 \cdot p_i & \text{if } s_i = U \\ 0 & \text{otherwise} \end{cases}$ return $T$	$S = C, -, C, U, G, U, U, G, A, U$ $P = 0.843, 0.000, 0.807, 0.807, 0.793,$ $0.914, 0.982, 1.000, 0.999, 0.999$ Without base-pair probability sequence: $T = -1, 0, -1, -2, 1, -2, -2, 1, 2, -2$ With base-pair probability sequence: $T = -0.843, 0.000, -0.807, -1.614,$ $0.793, -1.829, -1.963,$ $1.000, 1.999, -1.998$
2	Grouped variable-length channel mapping	$j = 1, k = 1$ $\text{for } i = 1 \text{ to }  S :$ $t_j^1 = \begin{cases} 1 \cdot p_i & \text{if } s_i = A \\ -1 \cdot p_i & \text{if } s_i = U \\ 0 & \text{otherwise} \end{cases}$ $t_k^2 = \begin{cases} 1 \cdot p_i & \text{if } s_i = G \\ -1 \cdot p_i & \text{if } s_i = C \\ \text{if } (s_i = G) \text{ or } (s_i = C): \\ \quad \text{increment } k \text{ by 1} \\ \text{else:} \\ \quad \text{increment } j \text{ by 1} \end{cases}$ return $T^1, T^2$	Without base-pair probability sequence: $T^1 = 0, -1, -1, -1, 1, -1$ $T^2 = -1, -1, 1, 1$ With base-pair probability sequence: $T^1 = 0.000, -0.807, -0.914, -0.982, 0.999, -0.999$ $T^2 = -0.843, -0.807, 0.793, 1.000$
3	Grouped fixed-length channel mapping	$\text{for } i = 1 \text{ to }  S :$ $t_i^1 = \begin{cases} 1 \cdot p_i & \text{if } s_i = A \\ -1 \cdot p_i & \text{if } s_i = U \\ 0 & \text{otherwise} \end{cases}$ $t_i^2 = \begin{cases} 1 \cdot p_i & \text{if } s_i = G \\ -1 \cdot p_i & \text{if } s_i = C \\ 0 & \text{otherwise} \end{cases}$ return $T^1, T^2$	Without base-pair probability sequence: $T^1 = 0, 0, -1, 0, -1, -1, 0, 1, -1$ $T^2 = -1, 0, -1, 0, 1, 0, 0, 1, 0, 0$ With base-pair probability sequence: $T^1 = 0.000, 0.000, 0.000, -0.807,$ $0.000, -0.914, -0.982,$ $0.000, 0.999, -0.9999$ $T^2 = -0.843, 0.000, -0.807, 0.000,$ $0.793, 0.000, 0.000,$ $1.000, 0.000, 0.000$
4	Cumulative mapping [98, 11]	$t_1 = 0$ $\text{for } i = 1 \text{ to }  S :$ $t_{i+1} = \begin{cases} t_i + 2 \cdot p_i & \text{if } s_i = A \\ t_i + 1 \cdot p_i & \text{if } s_i = G \\ t_i - 1 \cdot p_i & \text{if } s_i = C \\ t_i - 2 \cdot p_i & \text{if } s_i = U \\ t_i & \text{otherwise} \end{cases}$ return $T //  T  =  S  + 1$	Without base-pair probability sequence: $T = 0, -1, -1, -2, -4, -3, -5, -7, -6, -4, -6$ With base-pair probability sequence: $T = 0.000, -0.843, -0.843, -1.650,$ $-3.265, -2.471, -4.300, -6.263,$ $-5.264, -3.265, -5.263$
5	Cumulative grouped variable-length channel mapping	$t_1^1 = 0, t_1^2 = 0$ $j = 1, k = 1$ $\text{for } i = 1 \text{ to }  S :$ $t_{j+1}^1 = \begin{cases} t_j^1 + 1 \cdot p_i & \text{if } s_i = A \\ t_j^1 - 1 \cdot p_i & \text{if } s_i = U \\ t_j^1 & \text{if } s_i = - \end{cases}$ $t_{k+1}^2 = \begin{cases} t_k^2 + 1 \cdot p_i & \text{if } s_i = G \\ t_k^2 - 1 \cdot p_i & \text{if } s_i = C \\ t_k^2 & \text{otherwise} \end{cases}$ $\text{if } (s_i = G) \text{ or } (s_i = C):$ $\quad \text{increment } k \text{ by 1}$ $\text{else:}$ $\quad \text{increment } j \text{ by 1}$ return $T^1, T^2$	Without base-pair probability sequence: $T^1 = 0, -1, -2, -3, -2, -3$ $T^2 = 0, -1, -2, -1, 0$ With base-pair probability sequence: $T^1 = 0.000, -0.807, -1.722,$ $-2.703, -1.704, -2.703$ $T^2 = 0.000, -0.843, -1.650,$ $-0.857, 0.143$
6	Cumulative grouped fixed-length channel mapping	$t_1^1 = 0, t_1^2 = 0$ $\text{for } i = 1 \text{ to }  S :$ $t_{i+1}^1 = \begin{cases} t_i^1 + 1 \cdot p_i & \text{if } s_i = A \\ t_i^1 - 1 \cdot p_i & \text{if } s_i = U \\ t_i^1 & \text{otherwise} \end{cases}$ $t_{i+1}^2 = \begin{cases} t_i^2 + 1 \cdot p_i & \text{if } s_i = G \\ t_i^2 - 1 \cdot p_i & \text{if } s_i = C \\ t_i^2 & \text{otherwise} \end{cases}$ return $T^1, T^2 //  T^1  =  T^2  =  S  + 1$	Without base-pair probability sequence: $T^1 = 0, 0, 0, -1, -1, -2, -3, -2, -3$ $T^2 = 0, -1, -1, -2, -2, -1, -1, 0, 0, 0$ With base-pair probability sequence: $T^1 = 0.000, 0.000, 0.000, 0.000,$ $-0.807, -0.807, -1.722, -2.703,$ $-2.703, -1.704, -2.703$ $T^2 = 0.000, -0.843, -0.843, -1.650,$ $-1.650, -0.857, -0.857, -0.857,$ $0.143, 0.143, 0.143$

Table 3.4: Time series encoding.  $P$  is the corresponding base-pair probability sequence of  $S$ .  $p_i = 1$  if we encode  $S$  without incorporating base-pair probability sequence.

per channel, depending on group-specific occurrences. The second one always returns two resulting sequences of a fixed length. Two variations extended from single value mapping are shown in rows 2 and 3, while those extended from cumulative mapping are shown in rows 5 and 6 in Table 3.4. 768  
769  
770  
771

## Global Cumulative versus Local Cumulative 772

In cumulative mapping and its variations, we can choose where to start the accumulation. 773  
For a given subsequence  $S'$  of the whole sequence  $S$ , accumulation can start from the 774  
beginning of  $S$  even if only  $S'$  is used downstream. It can also begin just at the start 775  
of the  $S'$ . The first one preserves the global context. It can be useful when previous 776  
nucleotides (those before  $S'$ ) influence later interpretation. The second one focuses solely 777  
on local history in  $S'$ , ignoring global history. It is helpful if the previous nucleotides do 778  
not affect the chemical property of  $S'$ . 779

Consider  $T = 0, -1, \dots, -6$  of the input string  $S$  in “Cumulative mapping” in Table 3.4, 780  
which accumulates from 0.  $S$  is the suffix with length = 10 of the constructed complemen- 781  
tary strand of  $S(1 : 63)$  in Figure 3.1. If we start the accumulation from the first entry 782  
of the constructed complementary strand instead, it will yield a different result. Suppose 783  
that the last entry of the time series encoded in the cumulative mapping of the con- 784  
structed complementary strand is -8, the time series encoded in the “Global cumulative 785  
mapping” for  $S$  would accumulate from -8 instead of 0. The result is  $T = -8, -9, \dots, -14$ . 786  
Note that it has the same trend as the original  $T$ . This “Global cumulative” concept can 787  
be applied to every cumulative-based method, as shown in Figure 3.3. 788

## Incorporating Base-Pair Probabilities 789

We can incorporate the base-pair probabilities  $P$  in the encoding by thinking of it as the 790  
weight or confidence  $p_i$  in the value assignment of each nucleotide  $s_i$ . It is implemented 791  
by multiplying the base-pair probability  $p_i$  of the nucleotide  $s_i$  with the assigned value of 792  
the kind of nucleotide of  $s_i$  during encoding, as shown in Table 3.4. 793

## Transforming the Secondary Structure into a Time Series 794

We can transform the secondary structure in the dot-bracket notation into a time series 795  
by “Single value mapping”, where “(” maps to 1, “.” maps to 0, and “)” maps to -1. 796

### 3.2.3 Time Series Classification 797

In univariate time series classification, an instance in the dataset consists of a time series 798  
 $x = x_1, x_2, \dots, x_m$  with  $m$  observations and a discrete class label  $y$ , which takes  $c$  possible 799

values [8, 73]. If  $c = 2$ , we refer to binary classification. If  $c > 2$ , we refer to multi-class classification. In multivariate time series classification, the time series is not a single sequence but a list of sequences. Each sequence is called a channel. There are many classifiers defined for time series data, including distance-based, feature-based, interval-based, shapelet-based, dictionary-based, convolution-based, and deep learning-based classifiers. Additionally, two or more of the above approaches can be combined, resulting in hybrid approaches [64, 73, 8]. We employed convolution-based classifiers due to their simplicity and accuracy.

## Convolution-Based Classifiers

Convolution-based classifiers first use randomly parameterized kernels to perform convolutions on the original time series  $T$ . A kernel is referred to as parameterized because its behavior is governed by a set of parameters, which will be discussed in detail later. Convolution is an operation to transform  $T$  to another time series  $M$ , where  $M$  is called the activation map. Its entry  $M_i$  is calculated by applying a kernel  $\omega$  with length  $l$  to  $T$  at position  $i$ , defined as follows:

$$M_i = T(i : i + l - 1) * \omega = \sum_{j=0}^{l-1} t_{i+j} \cdot \omega_{1+j}$$

To note,  $|T(i : i + l - 1)| = |\omega| = l$ . Entries  $M_i$ 's are calculated by sliding  $\omega$  across  $T$  and computing a dot product. Additionally, although the original paper [23] used the term “convolution” to refer to the above operation, “cross-correlation” may be a more suitable term for this operation. Recall  $T$  with length  $m$  has  $(m - l + 1)$  sliding windows of length  $l$ , given that the increment is  $1^{10}$ , which defines the length of  $M$ .

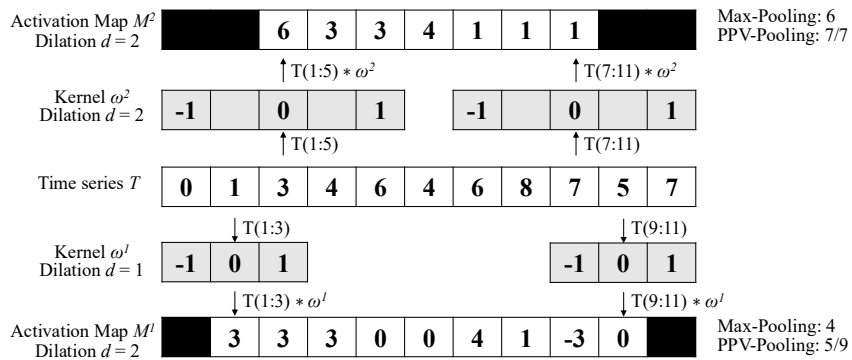


Figure 3.4: Features generation in the transformation

Figure 3.4 shows two kernels  $\omega^1$  and  $\omega^2$  with lengths 3 and 5, respectively. Each of which performs a convolution with  $T$  and returns two activation maps,  $M^1$  and  $M^2$ ,

<sup>10</sup>One step to the right per time.

respectively. For example,  $M_1^1 = T(1 : 3) * \omega^1 = 3$ . By sliding  $\omega^1$  one time stamp at a time, an activation map  $M^1$  with length =  $(m - l + 1) = 11 - 3 + 1 = 9$  is obtained. Then, pooling operations, such as the maximum (MAX) and proportion of positive values (PPV), are applied on  $M^1$  to derive the summary features. In Figure 3.4, MAX and PPV are applied on  $M^1$  and  $M^2$ . The summary features of  $M^1$  are 4 and  $5/9$ , which correspond to MAX and PPV, respectively. Dilation refers to a method that enables a kernel to cover a larger portion by creating empty spaces between entries in the kernel. The dilation  $d$  of  $\omega^2$  is 2. It introduces a gap of 1 in every two values of  $\omega^2$ .

The most popular convolution-based approach is the Random Convolutional Kernel Transform (ROCKET) [23]. It generates a large number of randomly parameterized kernels, ranging from thousands to tens of thousands. The kernel's parameters include length, weights (the entries inside the kernel), bias (the value added to the result of the convolution operation), and dilation. Additionally, padding can be applied to  $T$  at the start and end, ensuring  $M$  has the same length as the input. To note,  $T$ ,  $M_1$ , and  $M_2$  in Figure 3.4 have different lengths. The summary statistics of the activation map are obtained through two pooling operations: MAX and PPV. Hence, for  $k$  kernels, the transformed data has  $2k$  features. The default value of  $k$  is 10,000.

There are two extensions of ROCKET. They are MiniROCKET [24] and MultiROCKET [83]. MiniROCKET removes unnecessary operations and many of the random components in the definition of kernels used by ROCKET. It speeds up Rocket by over an order of magnitude with no significant difference in accuracy, making the classifier almost deterministic. For example, the kernel length is fixed, and only two weight values are used. Only PPV is used for the summary statistics. MultiROCKET is extended from MiniROCKET. The main improvement of it is to extract features from first-order differences as defined in Table 3.5 and add three new pooling operations [83]. The three added operations are mean of positive values (MPV), mean of indices of positive values (MIPV) and longest stretch of positive values (LSPV).

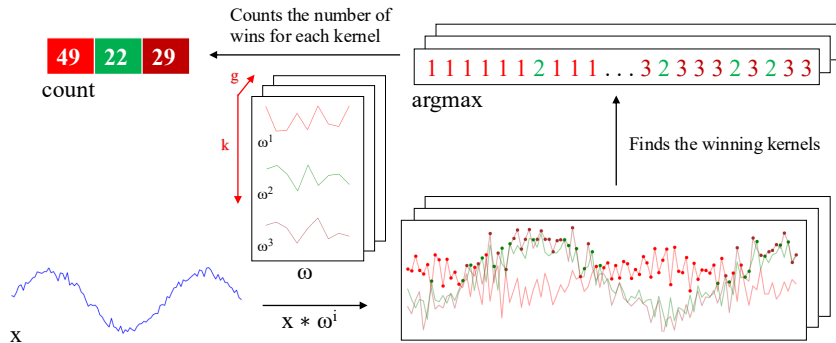


Figure 3.5: Convolutions of HYDRA for each input time series with a set of random kernels  $w$ , organized into  $g$  groups with  $k$  kernels each.

849 The HYbrid Dictionary-ROCKET Architecture (Hydra) combines dictionary-based  
850 and convolution-based models [25]. Similar to ROCKET-based classifiers, it uses random  
851 kernels to extract features from the input time series. But it groups the kernels into  $g$   
852 groups of  $k$  kernels each, as shown in Figure 3.5. Each time series is passed through  
853 all the groups. For each group of kernels, we slide them across  $T$  and compute the dot  
854 product at each timestamp. Recall that the dot product of two input vectors ( $x$  and  
855  $w_i$ ) has the maximum value when the two vectors align in the same direction and the  
856 minimum value when they are oriented in opposite directions. We record the kernel  
857 that best matches the subsequence of  $T$  at each timestamp in each group (i.e., argmax).  
858 We refer to these kernels as the winning kernels. This results in a  $k$ -dimensional count  
859 vector for each of the  $g$  groups, where  $k = 3$  in Figure 3.5. This results in a total of  
860  $g \times k$  features, with default values of  $g = 64$  and  $k = 8$ . It uses a total of  $k \times g = 512$   
861 kernels per dilation. In addition to recording the kernel with the maximum response,  
862 we can also record the kernel with the minimum response, knowing that this kernel will  
863 be the best match with the “inverted” subsequence of  $T$ . Hydra is applied to both the  
864 original time series and its first-order differences. Hydra generated approximately 1000  
865 features for each instance in our dataset. [25] found that it can improve the accuracy  
866 by concatenating features generated from Hydra with those from MultiRocket. This  
867 classifier is called MultiROCKET-Hydra.

868 These five classifiers share the same simple design pattern. It involves the overpro-  
869 duction of features followed by a selection strategy. A large number of features (1,000 ~  
870 50,000) are generated for each instance. The features are then fed into a simple linear  
871 classifier. It determines which features are most useful and returns the final classification  
872 result. A ridge classifier is used in this study. It is a linear classifier that extends ridge  
873 regression to classification tasks by applying a threshold to the predicted values. It uses  
874 L2 regularization to prevent overfitting. The regularization strength is selected by in-  
875 ternal cross-validation. A Ridge classifier is suggested for small datasets, as in our case,  
876 while a logistic regression classifier is suggested for large datasets [64].

877 While these five classifiers are often referred to as classifiers [64], they are technically  
878 time series transformation methods for generating features that are then fed to a down-  
879 stream classifier. The comparison of them is shown in Table 3.5. For MiniROCKET  
880 and MultiROCKET, the bias is determined from the convolution output, and the di-  
881 lation depends on the length of the input time series [24, 83]. The main differences  
882 among ROCKET-based classifiers lie in how the summary features are generated. The  
883 generation of the summary features depends on:

- 884 1. Kernels, which are defined based on the parameters, which consist of kernel length,  
885 kernel weights, bias, and dilation.

2. The way that padding applies to  $T$ , which leads to activation maps with different lengths. 886  
887
3. The pooling operations, which are used in extracting features on the activation map. 888  
889

	ROCKET	MiniROCKET	MultiROCKET	Hydra
kernel length	$\{7, 9, 11\}$	9	9	9
kernel weights	$\mathcal{N}(0, 1)$	$\{-1, 2\}$	$\{-1, 2\}$	$\mathcal{N}(0, 1)$
bias	$\mathcal{U}(0, 1)$	from output	from output	none
dilation	random	fixed (input-relative)	fixed (input-relative)	random
padding	random	fixed	fixed	always
pooling operations	MAX, PPV	PPV	PPV, MPV, MIPV, LSPV	Response per Kernel/Group
1 <sup>st</sup> order difference	no	no	yes	yes
feature vector size	20k	10k	50k	relative to input

Table 3.5: Comparison of rocket-based classifiers [64].  $\mathcal{N}(0, 1)$ : a standard normal distribution,  $\mathcal{U}(0, 1)$ : a uniform distribution between 0 and 1, 1<sup>st</sup> order difference:  $\Delta T = t_2 - t_1, t_3 - t_2, \dots, t_n - t_{n-1}$ .

### 3.2.4 Evaluation Metrics

To evaluate the performance of our time series-based classification (MTSC) model, we adopted five standard classification metrics. They are Accuracy (Acc), Specificity (Sp), Sensitivity (Sn), F1 score (F1), and Matthews Correlation Coefficient (MCC) [61].

$$Acc = \frac{TP + TN}{TP + TN + FP + FN}$$

$$Sp = \frac{TN}{TN + FP}$$

$$Sn = \frac{TP}{TP + FN}$$

$$F1 = \frac{2 \times TP}{2 \times TP + FP + FN}$$

$$MCC = \frac{TP \times TN - FP \times FN}{\sqrt{(TP + FP)(TP + FN)(TN + FP)(TN + FN)}}$$

where TP, TN, FP, and FN are the number of true positives, true negatives, false positives, and false negatives, respectively.

To extend a binary metric to multi-class problems, we can treat the data as a collection of binary problems, one for each class. One class is treated as positive while the other classes are treated as negative. Then, the multi-class metrics can be obtained by averaging binary metric calculations across the set of classes. There are different ways of doing the averaging. Here, we adopted a macro-averaging approach. It treats each class equally and calculates the mean of the binary metrics. To use  $MCC$  in the multiclass case, it

902 can be defined in terms of a confusion matrix  $C$  for  $K$  classes, where  $C_{i,j}$  is the number  
903 of observations that are actually in class  $i$  and predicted to be in class  $j$  [34].

$$MCC_{multi} = \frac{c \times s - \sum_k^K p_k \times t_k}{\sqrt{(s^2 - \sum_k^K p_k^2) \times (s^2 - \sum_k^K t_k^2)}}$$

904 where  $t_k = \sum_i^K C_{i,k}$  (denoting the number of times class  $k$  actually occurred),  $p_k =$   
905  $\sum_i^K C_{k,i}$  (denoting the number of times class  $k$  was predicted),  $c = \sum_k^K C_{k,k}$  (denoting  
906 the total number of samples correctly predicted) and  $s = \sum_i^K \sum_j^K C_{i,j}$  (denoting the total  
907 number of samples).

### 908 3.3 Results

909 The code implementing our method is available at <https://github.com/cyuab/time-series-classification-cleavage>. The dataset of this study is available at  
910 <https://www.mirbase.org>.

912 In all experiments, the models were trained and tested using 5-fold cross-validation.  
913 We retrieved 827 empirically validated sequences of pre-miRNAs. There are 5p arm  
914 and 3p arm in each sequence. For each arm, we defined a cleavage pattern and a non-  
915 cleavage pattern. Three datasets, namely “5p arm”, “3p arm”, and “multi-class” were  
916 constructed by these patterns. We refer to the cleavage patterns as positive instances  
917 and the non-cleavage patterns as negative instances. The 5p arm dataset comprises 827  
918 positive instances and an equal number of negative instances. The 5p arm and 3p arm  
919 datasets are binary-class datasets. The multi-class dataset comprises all patterns from  
920 both the 5p arm and the 3p arm. There are 827 “5p” instances<sup>11</sup>, 827 “3p” instances,  
921 and 1,654 negative instances.

922 For every fold in 5-fold cross-validation, the dataset was divided into a training set  
923 and a test set with sizes of 80% and 20% of the whole dataset, respectively. We kept the  
924 class distribution approximately the same in each fold, since it is in the original dataset.  
925 In each fold derived from the 5p arm and 3p arm datasets, the training set has a size of  
926 1,323, and the test set has a size of 331. In each fold derived from the multi-class dataset,  
927 the training set has a size of 2,262, and the test set has a size of 662. We reported the  
928 average of the five classification metrics.

929 The ROCKET-based classifiers require all channels in the multivariate time series to  
930 have equal length. We applied padding to the shorter channels using the constant value  
931 100, which does not appear in the original time series. It ensures the padding does not  
932 introduce ambiguity or interfere with the semantic meaning of the encoded nucleotide  
933 signals.

---

<sup>11</sup>Cleavage patterns from the 5p arm.

### 3.3.1 Channel Ablation Study

We utilized three types of data as the input features for each instance. They are (1) the RNA sequence, which consists of the primary strand and its complementary strand, (2) the secondary structure information, and (3) the base-pair probability sequence. To input the data into our time series-based classifiers, we converted them into multivariate time series. The primary strand and its complementary strand are each encoded into one or two channels, using the encoding methods in Table 3.4. For example, single value mapping encodes a strand in one channel, while grouped variable-length channel mapping encodes in two channels. The secondary structure information is converted into a univariate time series. The base-pair probability sequence is already in numerical form and does not require further transformation. It can be used either as a standalone channel or incorporated into the encoding of the complementary strand. We performed a channel ablation study to determine the most informative combination of the above channels.

We referred to the multivariate time series that consists of the channels from the RNA sequence only as the baseline setting. We added the other channels to this baseline. It leads to the following configurations (cfgs):

1. (cfg 1) Baseline: Time series derived only from the RNA sequence.
2. (cfg 2) Baseline + Secondary structure: Baseline + time series representation of the secondary structure.
3. (cfg 3) Baseline + Base-pair probability (Standalone): Baseline + the base-pair probability sequence as a standalone channel.
4. (cfg 4) Baseline + Base-Pair probability (Incorporated): Baseline with the base-pair probability sequence incorporated into the encoding of the complementary strand.

Classifier	5p arm					3p arm					multi-class					
	Acc	Sp	Sn	F1	MCC	Acc	Sp	Sn	F1	MCC	Acc	Sp	Sn	F1	MCC	
Baseline (cfg 1)	ROCKET	0.781	0.743	0.819	0.789	0.563	0.790	0.773	0.807	0.793	0.580	0.717	0.838	0.685	0.700	0.538
	MiniROCKET	0.755	0.728	0.782	0.762	0.512	0.788	0.781	0.794	0.789	0.576	0.685	0.823	0.653	0.662	0.486
	MultiROCKET	0.784	0.767	0.801	0.787	0.569	0.803	0.792	0.814	0.805	0.606	0.691	0.830	0.667	0.672	0.501
	Hydra	0.830	0.800	0.860	0.835	0.663	0.808	0.797	0.820	0.810	0.617	0.731	0.844	0.696	0.712	0.560
	MultiROCKET-Hydra	0.796	0.778	0.815	0.800	0.594	0.807	0.767	0.816	0.808	0.614	0.701	0.836	0.681	0.686	0.520
Baseline + Secondary Structure (cfg 2)	ROCKET	<b>0.847</b>	<b>0.832</b>	0.862	<b>0.849</b>	<b>0.695</b>	<b>0.855</b>	0.842	0.868	<b>0.857</b>	<b>0.711</b>	<b>0.836</b>	<b>0.907</b>	<b>0.828</b>	<b>0.833</b>	0.736
	MiniROCKET	0.825	0.807	0.843	0.827	0.652	0.822	0.802	0.843	0.826	0.646	0.823	0.900	0.812	0.818	0.715
	MultiROCKET	0.812	0.803	0.822	0.814	0.626	0.824	0.809	0.839	0.826	0.649	0.796	0.888	0.791	0.792	0.673
	Hydra	0.845	0.816	<b>0.873</b>	<b>0.849</b>	0.691	0.846	0.817	<b>0.874</b>	0.850	0.693	0.830	0.901	0.814	0.826	0.724
	MultiROCKET-Hydra	0.817	0.809	0.826	0.819	0.635	0.825	0.816	0.834	0.826	0.652	0.803	0.891	0.798	0.800	0.684
Baseline + Base-pair probability (Standalone) (cfg 3)	ROCKET	0.842	0.828	0.855	0.844	0.684	<b>0.855</b>	<b>0.856</b>	0.854	0.855	0.710	0.795	0.885	0.783	0.789	0.670
	MiniROCKET	0.817	0.820	0.814	0.816	0.634	0.836	0.834	0.838	0.836	0.673	0.772	0.872	0.757	0.764	0.632
	MultiROCKET	0.822	0.813	0.832	0.824	0.645	0.825	0.831	0.820	0.824	0.651	0.758	0.866	0.747	0.750	0.612
	Hydra	0.846	0.827	0.865	<b>0.849</b>	0.693	0.851	0.840	0.861	0.852	0.702	0.789	0.879	0.769	0.780	0.658
	MultiROCKET-Hydra	0.822	0.809	0.834	0.824	0.644	0.835	0.840	0.830	0.834	0.670	0.759	0.866	0.746	0.750	0.611
Baseline + Base-pair probability (Incorporated) (cfg 4)	ROCKET	0.799	0.771	0.827	0.805	0.600	0.809	0.786	0.832	0.813	0.619	0.737	0.850	0.712	0.724	0.573
	MiniROCKET	0.776	0.756	0.797	0.781	0.554	0.801	0.808	0.794	0.799	0.603	0.705	0.835	0.675	0.684	0.521
	MultiROCKET	0.814	0.801	0.828	0.817	0.630	0.816	0.812	0.820	0.816	0.634	0.726	0.848	0.706	0.712	0.556
	Hydra	0.822	0.787	0.857	0.828	0.647	0.834	0.828	0.840	0.835	0.669	0.759	0.862	0.734	0.746	0.608
	MultiROCKET-Hydra	0.814	0.802	0.820	0.817	0.629	0.820	0.825	0.816	0.819	0.642	0.736	0.853	0.717	0.723	<b>0.874</b>

Table 3.6: Channel ablation study. The best results are highlighted in **bold**.

957 We used single value mapping as the encoding method. Table 3.6 shows the result.  
 958 From the table, we can see that the addition of secondary structure, base-pair probability  
 959 as a standalone channel, and base-pair probability incorporated in the encoding of the  
 960 complementary strand can improve the performance. We plotted the critical difference  
 961 (CD) diagram as shown in Figure 3.6 to visualize Table 3.6 to make the performances  
 962 of different combinations more obvious. In CD diagrams, lower-ranked methods (toward  
 963 the right) are better. A horizontal bar connecting combinations indicates no statistically  
 964 significant difference.

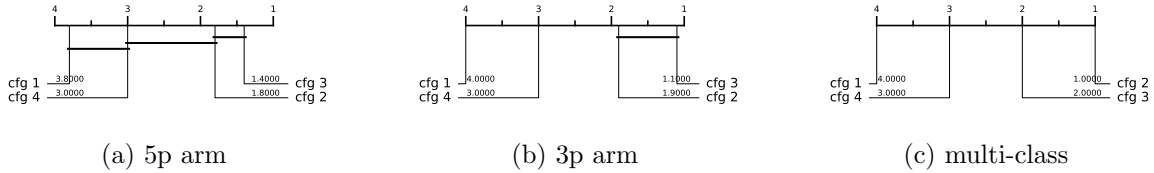


Figure 3.6: CD diagrams of channel ablation study.

965 From Figure 3.6, we can see that including time series derived from secondary struc-  
 966 ture information and base-pair probability as a separate channel can significantly improve  
 967 the performance of the classifiers. Incorporating the base-pair probability sequence in the  
 968 time series encoding of the complementary strand can also improve the classifier, but to  
 969 a minor degree compared to serving as a standalone channel. In our downstream analy-  
 970 sis, we adopted the combination of RNA sequence time series, secondary structure time  
 971 series, and base-pair probability time series as our multivariate time series input, with 4  
 972 to 6 channels, depending on the encoding used.

### 973 3.3.2 Predictive Performance

974 The experiment was conducted on three datasets: the 5p arm, the 3p arm, and the  
 975 multi-class datasets. Recall that we have nine encoding methods and five ROCKET-  
 976 based classifiers. It results in 45 combinations of encoding methods and classifiers.

977 The result is shown in Table 3.7. The best combination of encoding method and  
 978 classifier is shown in Table 3.8. For the 5p arm dataset, the best combination is “Global  
 979 Cumulative grouped fixed-length channel mapping + ROCKET”. For all five classifica-  
 980 tion metrics, it outperforms the state-of-the-art (SOTA) method, DiCleave. For the 3p  
 981 arm dataset, the best combination is “Global Cumulative grouped fixed-length channel  
 982 mapping + ROCKET”. Out of the five classification metrics, it outperforms DiCleave,  
 983 except in specificity. For the multi-class dataset, the best combination is “Global Cu-  
 984 mulative grouped fixed-length channel mapping + ROCKET”. For all five classification  
 985 metrics, it outperforms DiCleave. Note that for the 3p arm and the multi-class datasets,

	Classifier	5p arm					3p arm					multi-class				
		Acc	Sp	Sn	F1	MCC	Acc	Sp	Sn	F1	MCC	Acc	Sp	Sn	F1	MCC
Single value mapping (enc 1)	ROCKET	0.849	0.842	0.857	0.851	0.699	0.863	0.854	0.873	0.865	0.727	0.853	0.917	0.847	0.851	0.764
	MiniROCKET	0.823	0.809	0.837	0.825	0.647	0.823	0.828	0.817	0.822	0.647	0.835	0.906	0.828	0.833	0.735
	MultiROCKET	0.821	0.802	0.840	0.824	0.643	0.839	0.826	0.852	0.841	0.679	0.811	0.894	0.806	0.809	0.697
	Hydra	0.843	0.820	0.867	0.847	0.688	0.838	0.819	0.857	0.841	0.677	0.831	0.901	0.815	0.827	0.727
	MultiROCKET-Hydra	0.820	0.803	0.837	0.823	0.640	0.840	0.830	0.850	0.841	0.680	0.816	0.896	0.810	0.814	0.704
Grouped variable-length channel mapping (enc 2)	ROCKET	0.835	0.826	0.844	0.836	0.670	0.855	0.849	0.861	0.856	0.710	0.846	0.913	0.839	0.844	0.752
	MiniROCKET	0.843	0.833	0.853	0.844	0.686	0.831	0.821	0.842	0.833	0.663	0.837	0.907	0.828	0.834	0.737
	MultiROCKET	0.819	0.809	0.828	0.820	0.638	0.817	0.814	0.820	0.818	0.634	0.890	0.894	0.806	0.808	0.695
	Hydra	0.825	0.780	0.869	0.832	0.653	0.811	0.769	0.854	0.819	0.626	0.818	0.892	0.765	0.812	0.705
	MultiROCKET-Hydra	0.818	0.814	0.822	0.819	0.636	0.831	0.825	0.837	0.832	0.662	0.820	0.900	0.815	0.818	0.710
Grouped fixed-length channel mapping (enc 3)	ROCKET	0.851	0.843	0.859	0.852	0.702	0.863	0.850	0.875	0.864	0.726	0.849	0.915	0.843	0.847	0.757
	MiniROCKET	0.844	0.836	0.853	0.845	0.689	0.840	0.826	0.855	0.843	0.682	0.851	0.915	0.844	0.849	0.760
	MultiROCKET	0.831	0.815	0.848	0.834	0.663	0.824	0.813	0.836	0.826	0.649	0.811	0.896	0.808	0.808	0.698
	Hydra	0.848	0.816	0.880	0.853	0.699	0.862	0.839	0.884	0.864	0.724	0.843	0.908	0.837	0.839	0.746
	MultiROCKET-Hydra	0.836	0.813	0.859	0.839	0.672	0.833	0.820	0.845	0.835	0.665	0.828	0.905	0.824	0.826	0.725
Cumulative mapping (enc 4)	ROCKET	0.850	0.834	0.866	0.852	0.701	0.863	0.855	0.871	0.864	0.726	0.852	0.915	0.842	0.850	0.762
	MiniROCKET	0.840	0.821	0.860	0.843	0.682	0.840	0.837	0.844	0.841	0.682	0.843	0.911	0.835	0.840	0.747
	MultiROCKET	0.822	0.809	0.834	0.824	0.644	0.832	0.830	0.834	0.832	0.665	0.820	0.898	0.810	0.816	0.709
	Hydra	0.848	0.819	0.878	0.853	0.698	0.853	0.856	0.869	0.855	0.705	0.845	0.910	0.830	0.841	0.749
	MultiROCKET-Hydra	0.824	0.811	0.856	0.825	0.647	0.838	0.833	0.843	0.839	0.677	0.821	0.898	0.810	0.817	0.711
Cumulative grouped variable-length channel mapping (enc 5)	ROCKET	0.843	0.821	0.866	0.847	0.688	0.856	0.840	0.871	0.857	0.712	0.855	0.916	0.843	0.851	0.766
	MiniROCKET	0.845	0.826	0.865	0.848	0.691	0.836	0.833	0.838	0.836	0.672	0.840	0.909	0.833	0.838	0.742
	MultiROCKET	0.826	0.814	0.838	0.828	0.653	0.815	0.820	0.810	0.814	0.631	0.826	0.902	0.820	0.824	0.721
	Hydra	0.850	0.819	0.880	0.854	0.701	0.834	0.807	0.861	0.838	0.669	0.833	0.903	0.818	0.829	0.731
	MultiROCKET-Hydra	0.824	0.810	0.838	0.826	0.649	0.833	0.833	0.833	0.833	0.666	0.830	0.903	0.821	0.827	0.726
Cumulative grouped fixed-length channel mapping (enc 6)	ROCKET	0.856	0.836	0.876	0.858	0.712	0.870	0.861	0.879	0.871	0.741	0.863	0.921	0.852	0.860	0.780
	MiniROCKET	0.856	0.837	0.874	0.858	0.712	0.842	0.839	0.845	0.843	0.685	0.845	0.912	0.837	0.843	0.751
	MultiROCKET	0.820	0.802	0.839	0.824	0.642	0.798	0.798	0.798	0.798	0.597	0.809	0.894	0.806	0.807	0.694
	Hydra	0.850	0.814	0.885	0.855	0.701	0.855	0.840	0.869	0.857	0.711	0.847	0.910	0.831	0.843	0.752
	MultiROCKET-Hydra	0.820	0.801	0.839	0.823	0.641	0.807	0.813	0.802	0.806	0.615	0.821	0.900	0.817	0.819	0.713
Global Cumulative mapping (enc 7)	ROCKET	0.850	0.834	0.866	0.852	0.701	0.863	0.855	0.871	0.864	0.726	0.852	0.915	0.842	0.850	0.762
	MiniROCKET	0.847	0.832	0.862	0.849	0.695	0.848	0.839	0.857	0.850	0.697	0.845	0.911	0.836	0.843	0.750
	MultiROCKET	0.827	0.819	0.834	0.828	0.653	0.847	0.842	0.853	0.848	0.695	0.825	0.901	0.817	0.822	0.718
	Hydra	0.851	0.821	0.880	0.855	0.703	0.861	0.848	0.874	0.863	0.722	0.847	0.911	0.834	0.844	0.753
	MultiROCKET-Hydra	0.829	0.823	0.834	0.830	0.658	0.843	0.838	0.849	0.844	0.688	0.832	0.905	0.823	0.829	0.730
Global Cumulative grouped variable-length channel mapping (enc 8)	ROCKET	0.840	0.814	0.867	0.844	0.682	0.853	0.838	0.867	0.854	0.706	0.856	0.917	0.845	0.853	0.768
	MiniROCKET	0.848	0.834	0.862	0.850	0.697	0.841	0.824	0.859	0.844	0.683	0.844	0.911	0.856	0.842	0.748
	MultiROCKET	0.834	0.828	0.839	0.834	0.668	0.831	0.821	0.842	0.833	0.663	0.828	0.904	0.823	0.826	0.724
	Hydra	0.857	0.821	0.894	0.862	0.717	0.822	0.786	0.857	0.828	0.645	0.826	0.898	0.806	0.820	0.717
	MultiROCKET-Hydra	0.837	0.834	0.839	0.837	0.674	0.834	0.827	0.840	0.835	0.668	0.835	0.907	0.828	0.832	0.734
Global Cumulative grouped fixed-length channel mapping (enc 9)	ROCKET	0.856	0.836	0.876	0.858	0.712	0.870	0.861	0.879	0.871	0.741	0.863	0.921	0.852	0.860	0.780
	MiniROCKET	0.857	0.845	0.870	0.859	0.715	0.840	0.821	0.859	0.843	0.681	0.844	0.911	0.837	0.842	0.749
	MultiROCKET	0.829	0.825	0.833	0.830	0.658	0.820	0.816	0.823	0.820	0.640	0.819	0.900	0.816	0.817	0.710
	Hydra	0.856	0.817	0.894	0.861	0.713	0.859	0.838	0.880	0.862	0.719	0.846	0.911	0.832	0.843	0.752
	MultiROCKET-Hydra	0.829	0.824	0.834	0.830	0.658	0.822	0.825	0.819	0.821	0.644	0.827	0.904	0.823	0.824	0.722

Table 3.7: Performance on the 45 combinations between encoding methods and the ROCKET-based classifiers. The best results are highlighted in **bold**.

the combination of “Cumulative grouped fixed-length channel mapping + ROKCET” 986 also attains the best result. 987

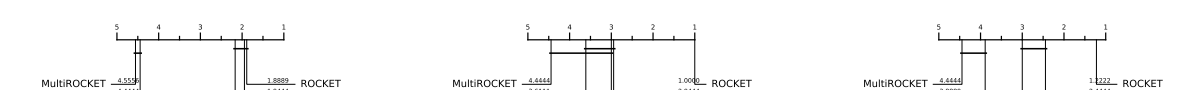


Figure 3.7: CD diagrams to compare different classifiers.

To summarize Table 3.7, we plot the CD diagrams for finding the best classifier, as shown in Figure 3.7, and the best encoding method, as shown in Figure 3.8. 988 989

Dataset	Methods	Acc	Sp	Sn	F1	MCC	Time (s)
5p arm	enc 9 + MiniROCKET	<b>0.857</b>	<b>0.845</b>	<b>0.870</b>	<b>0.859</b>	<b>0.715</b>	<b>0.787</b>
	DiCleave	0.818	0.790	0.846	0.822	0.653	21.249
3p arm	enc 9 + ROCKET	<b>0.870</b>	0.861	<b>0.879</b>	<b>0.871</b>	<b>0.741</b>	4.311
	enc 7 + MiniROCKET	0.848	0.839	0.857	0.850	0.697	<b>0.989</b>
	DiCleave	0.854	<b>0.891</b>	0.817	0.847	0.715	15.919
multi-class	enc 9 + ROCKET	<b>0.863</b>	<b>0.921</b>	<b>0.852</b>	<b>0.860</b>	<b>0.780</b>	12.208
	enc 3 + MiniROCKET	0.851	0.915	0.844	0.849	0.760	<b>4.550</b>
	DiCleave	0.820	0.895	0.804	0.815	0.710	131.151

Table 3.8: Comparative analysis between MTSCCleav with the best combination of the encoding method and classifier, with the SOTA, DiCleave, on the three datasets. The best results of using MiniROCKET have also been shown to compare the computational efficiency. The best results are highlighted in **bold**.

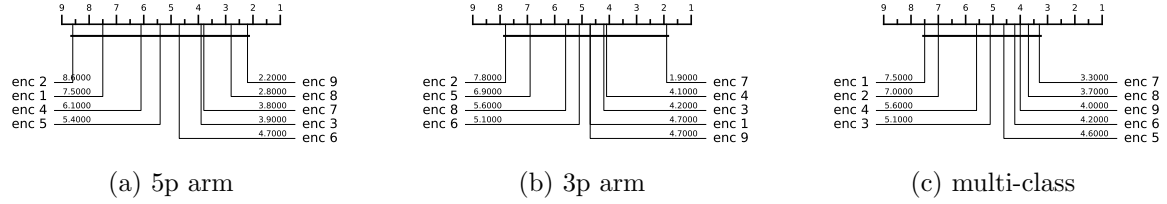


Figure 3.8: CD diagrams to compare different encoding methods.

### 3.3.3 Running Time Analysis

To compare the computational efficiency of MTSCCleav and DiCleave, we conducted a comparative analysis of their running times. For DiCleave, we employed the code from its supporting website<sup>12</sup>, without any modifications. All experiments were conducted on the same machine (a personal laptop equipped with an Apple M1 Pro chip and 16 GB of memory) and using the same splits of the training and test datasets under 5-fold cross-validation to ensure fairness. The reported running times are the averages of the five runs. The timing results were measured from the training phase to the return of the five classification metrics. The result is shown in Table 3.8. MiniROCKET is the most computationally efficient of the five rocket-based classifiers. We also included its best result, along with the corresponding encoding method, even though this combination may not be the best overall.

MTSCCleav demonstrated a significant advantage in computational efficiency, achieving an average 27.0X, 3.7X, and 10.7X speedup over DiCleave, for the 5p arm, 3p arm, and multi-class datasets, respectively. If we consider using the MiniROCKET in the case of 3p arm and multi-class datasets, it achieves 16.1X and 28.8X speedup. To note, in the

<sup>12</sup>

<https://github.com/MGuard0303/DiCleave> (Accessed on: 2025-07-13).

case of the 3p arm dataset, the performance of MiniROCKET is only slightly worse than 1006  
DiCleave. In the case of the multi-class dataset, even the performance of MiniROCKET 1007  
is better than DiCleave. DiCleave is a deep learning-based method that requires sub- 1008  
stantial time for model inference, while MTSCleav leverages efficient ROCKET-based 1009  
classifiers. This significant reduction in runtime makes MTSCcleav more suitable for 1010  
large-scale data and real-time applications. 1011

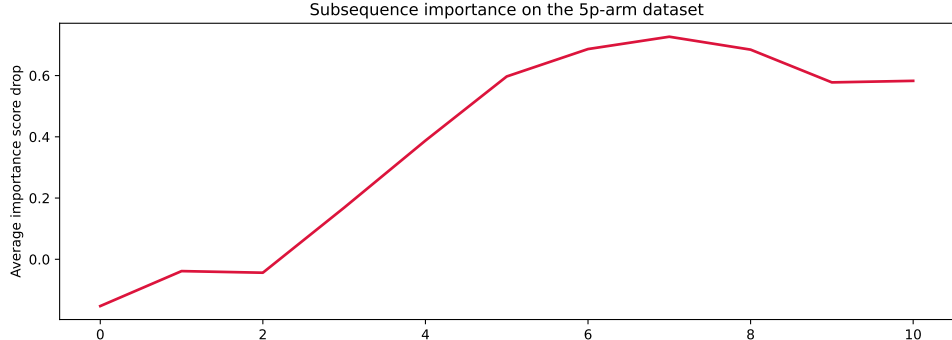
### 3.3.4 Subsequence Importance

To evaluate the sensitivity of MTSCcleav to subsequences of the input, we conducted a 1013  
perturbation experiment to evaluate the importance of subsequences based on masking 1014  
windows. The goal of this experiment is to identify which subsequences of the entire 1015  
time series are critical for classification. We examine how various modifications to the 1016  
original input impact model performance. It suggests which features are essential for 1017  
classification. 1018

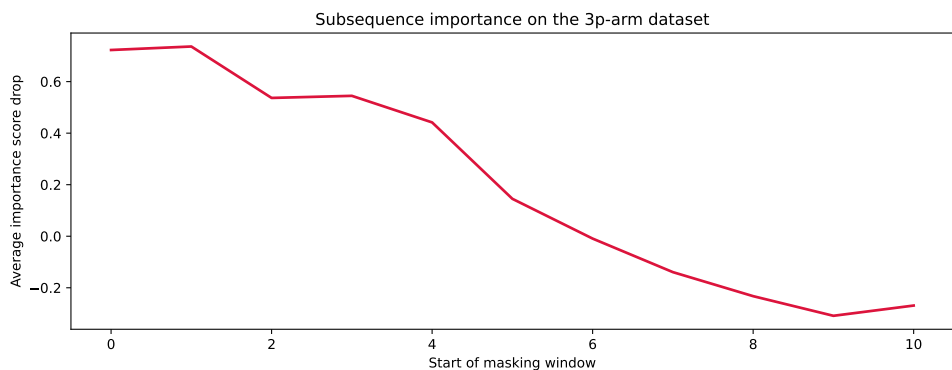
The model was trained on the original training dataset. For each instance in the test 1019  
dataset, we measure its original score and the masked score. We slid a masking window 1020  
 $w$  with a fixed length over the input time series  $T$ .  $|w|$  was set to 4. For each window 1021  
position  $i \in \{1, 2, \dots, |T| - |w| + 1\}$ , we masked all entries across all the channels of  $T$  1022  
within the window. Hence, we removed or hid that portion of information from the model 1023  
during inference. The changes in classification performance in terms of accuracy relative 1024  
to the unmasked original score of each  $i$  are recorded. Intuitively, if the information of a 1025  
subsequence is critical for the classification, the masking of this subsequence would lead 1026  
to a great drop in classification performance. We aggregated the importance score across 1027  
the test dataset. 1028

The result is shown in Figure 3.9. For the encoding methods, we cannot use the 1029  
methods derived from the cumulative mapping because the accumulation would leak in- 1030  
formation from the masked region. We adopted “Grouped fixed-length channel mapping” 1031  
as the encoding method and ROCKET as the classifier. “Grouped fixed-length channel 1032  
mapping” is the best encoding, other than the methods derived from the cumulative map- 1033  
ping, in all datasets, as shown in Figure 3.8. ROCKET is the best classifier, as shown in 1034  
Figure 3.7. 1035

In the 5p arm dataset, we found that masking subsequences at the tailing part caused 1036  
a significant drop in the importance score, as shown in Figure 3.9 (a). In the 3p arm 1037  
dataset, we found that masking subsequences at the leading part caused a significant 1038  
drop in the importance score, as shown in Figure 3.9 (b). 1039



(a) 5p arm



(b) 3p arm

Figure 3.9: Results of the perturbation experiment.

### 3.3.5 Summary

Our method achieves better or comparable predictive results and a 3.7X to 28.8X speedup compared to the state-of-the-art (SOTA).

## 3.4 Discussion

The channel ablation study reveals that the involvement of the time series derived from the secondary structure can improve accuracy. It suggests the importance of RNA folding in dicer processing. Furthermore, we found that the base-pair probability sequence of the secondary structure can also enhance accuracy. To the best of our knowledge, it is a novel application of the base-pair probability sequence. Experiments show that using the probability sequence as an additional channel can enhance accuracy more than incorporating it in the encoding. It is likely because keeping it as an additional channel can preserve more information, of both the probability sequence itself and the complementary strand.

Out of the three datasets, the best classifier is ROCKET. The ranking of the five classifiers by performance, starting from the best, is as follows: ROCKET, Hydra, MiniROCKET, MultiROCKET-Hydra, and MultiROCKET. It indicates that the fea-

tures created from the pooling operations that are only in MultiROCKET but not in MiniROCKET, confuse the final classifier. They are mean of positive values (MPV), mean of indices of positive values (MIPV) and longest stretch of positive values (LSPV) [83]. In contrast, the pooling operator that is only present in ROCKET but not in MiniROCKET, enhances the classification performance. It is maximum (MAX). 1055  
1056  
1057  
1058  
1059

For the encoding methods, we have the following observations. Fixed-length grouped channel mappings outperform variable-length counterparts with one exception in the multi-class dataset, likely because fixed-length schemes better preserve the original positional information of nucleotides within the sequence. Global cumulative methods consistently yield better performance than local cumulative methods. It suggests that the upstream information of the cleavage pattern plays a critical role in identifying cleavage sites. Cumulative-based encodings perform better than single-value mappings, with one exception in the 3p dataset, suggesting that the accumulated nucleotide signal is more informative for cleavage site prediction than the local or isolated presence of nucleotides. In the 5p arm dataset, encoding RNA sequence in two channels appears to worsen the result. This suggests that the 5p arm dataset and the 3p arm dataset need different nucleotide grouping methods for the encoding. 1060  
1061  
1062  
1063  
1064  
1065  
1066  
1067  
1068  
1069  
1070  
1071

One limitation of DiCleave is overfitting during training because of the relatively small size of the dataset [66]. DiCleave is a deep learning-based method. Deep learning models typically require a large amount of training data to generalize effectively. They are data-hungry. In contrast, MTSCCleav leverages ROCKET-based methods for the classification. They rely on random convolutional feature extraction followed by a simple linear classifier. The Ridge classifier used in this study is less data-hungry compared to deep learning methods due to its use of L2 regularization and the simplicity of its linear model nature. It allows ROCKET-based classifiers, and hence MTSCCleav, to maintain strong predictive performance even in settings with a relatively small dataset size. 1072  
1073  
1074  
1075  
1076  
1077  
1078  
1079  
1080

The subsequence importance reveals some connections between RNA secondary structure and human dicer cleavage site prediction. The perturbation experiment shows that the leading part of 5p arm and the tailing part of 3p arm are important for the classification. These parts are close to the center of the RNA secondary structure of pre-miRNA. It indicates that the center region is more crucial for human dicer cleavage site prediction. It is consistent with the previous study [56]. 1081  
1082  
1083  
1084  
1085  
1086

### 3.5 Concluding Remarks 1087

We proposed an accurate, fast, and simple multivariate time series classification (MTSC)-based method, termed MTSCCleav, for predicting human dicer cleavage sites. Base-pair probability sequences of the secondary structures have also been leveraged in the classification. MTSCCleav consists of three parts: time series encoding, time series 1088  
1089  
1090  
1091

transformation, and classification. ROCKET-based methods were used for time series transformation. Ridge Classifier was used for classification. For the computational experiments, we evaluated nine time series encoding methods in conjunction with five time series transformation methods. MTSCCleav outperformed the SOTA method in all five evaluation metrics for the 5p-arm and multi-class datasets, and four of the metrics for the 3p-arm dataset. In terms of computational efficiency, MTSCCleav with the optimal setting achieved an average 3.7X to 27.0X speedup over the SOTA method on the three datasets. With the use of a less accurate but faster time series classification method, MTSCCleav achieved an average speedup of 16.1X to 28.8X, respectively. We analyzed the subsequence importance of the input multivariate time series. The results show that subsequences near the center of the pre-miRNA sequences are more important. This aligns with the findings from previous work. This study demonstrates that time series analysis provides a powerful alternative to conventional modeling in the context of RNA processing. This framework may be extended to other RNA-processing tasks. Notably, the encoding of RNA sequence into time series enables us to utilize any well-established tools from the time series community.

# Chapter 4

1108

## Scaling with Multiple Scaling

1109

## Factors in Time Series Searching

1110

Time series data are ubiquitous across many different fields. Many data mining tasks, such as classification, clustering, and motif finding, have been defined for time series data. They utilize similarity search as a core subroutine, making it crucial to design similarity measures that align with our intuitions. To facilitate efficient computation, speedup techniques are essential. Dynamic Time Warping (DTW) is arguably the most prevailing distance measure for time series data. However, studies have shown that for certain data, another distance measure, namely Uniform Scaling (US), is equally crucial as DTW. DTW handles the local distortion, while US handles the global scaling. In addition, studies have demonstrated that combining DTW and US is necessary to obtain meaningful results in some cases. Surprisingly, all existing studies employ only a single scaling factor for the entire time series. A time series could consist of phases. Since each phase of a time series expresses at its own rate, using a single scaling factor is insufficient when comparing two time series that share similar phases but differ in their expression rates. We introduce the first framework that accounts for multiple scaling factors, Piecewise Scaling Distance (PSD). PSD employs other existing distance measures as subroutines. Because the naive implementation of PSD is slow, we propose a constrained version of PSD that enforces constraints based on the allowed segment lengths derived from the given scaling factor bound. It also prevents pathological results. In addition, two other speedup techniques have been proposed, which achieve 10.10X to 191.46X speedup. We also demonstrate the usage of a lower bound when DTW is used as the subroutine of PSD. Moreover, we show that the segmentation results returned by PSD can improve the accuracy of other distance measures.

1132

1133 **4.1 Background**

1134 To study the mechanism of a process, we take measurements. Measurements are usually  
1135 taken continuously by the sensors. Measurements of processes always yield continuous  
1136 values at discrete timestamps. They are time series data. For example, smartphones  
1137 collect users' GPS data. ECG monitors measure patients' heart rate. The continuous  
1138 measurements compose a time series. It is not hard to see why time series data are  
1139 ubiquitous across many different fields. In GPS data, each time series data point consists  
1140 of the user's latitude and longitude information. They are multivariate time series. In  
1141 ECG data, each data point represents the amplitude of the patient's cardiac electrical  
1142 activity. They are univariate time series In this study, we focus on univariate time series.

1143 Many data mining tasks can be defined on time series data. For example, given a  
1144 time series database, we can perform clustering based on the pairwise similarity of the  
1145 time series instances. A classifier can be trained when categorical labels are available.  
1146 Alternatively, given a long time series, for motif finding, we identify recurring patterns.  
1147 In contrast, for anomaly detection, we identify abnormal subsequences. Almost all time  
1148 series data mining tasks can be reduced to arguing the similarity between two time se-  
1149 ries. A good distance measure, also known as a similarity measure, can determine the  
1150 success or failure of the algorithms built on it. The choice of an appropriate distance mea-  
1151 sure is particularly evident in classification. Studies show that simple nearest-neighbor  
1152 classification (1-NN) is difficult to beat and can compete with more complex methods [8].

1153 A time series is treated as a whole rather than as a collection of individual values.  
1154 The relationships between values are important. They constitute trends and shapes.  
1155 Hence, similarity search in time series data is approximate-based rather than exact match-  
1156 based [32]. Besides, different invariances should be allowed during the comparison.

1157 Dynamic Time Warping (DTW) is one of, if not the most common, similarity mea-  
1158 sures. DTW provides invariance to time distortion by aligning and measuring the sim-  
1159 ilarity between two series that may be misaligned in time. However, it assumes that  
1160 the time series are expressed on a similar global expression rate. This assumption limits  
1161 its performance when comparing two time series expressed at different global expression  
1162 rates. We often see this behavior in domains such as speech recognition, motion analysis,  
1163 patient biomedical signals, and sensor data in the manufacturing industry.

1164 Uniform Scaling (US) can achieve global scaling invariance by scaling the two time  
1165 series to the same length via interpolation, such as nearest-neighbor interpolation, before  
1166 comparison, as shown in Figures 4.1. It is reported that in some domains, such as  
1167 gestures [72, 54] and music performance [21], the scaling is about 10-15% (i.e., scaling  
1168 factors: 1.1 to 1.15). The scaling factors are relatively small, since the nature of the  
1169 music and the gait will change with significant scaling factors. However, in some other  
1170 domains, we may encounter larger scaling factors. In bioinformatics, gene expression time

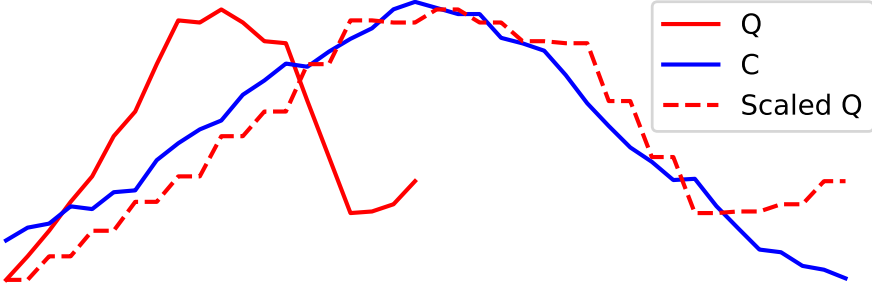


Figure 4.1: Applying nearest neighbor interpolation on  $Q$ , which result in Scaled  $Q$ , that can better reflect its similarity with  $C$ .

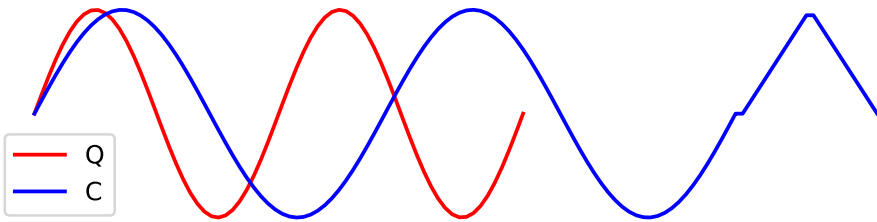


Figure 4.2:  $Q$  and  $C$  are in different rates. A stretching version of  $Q$  is similar to a prefix of  $C$ , but not the whole  $C$ .

series data could differ by a factor of 1.41 [52, 10]. In Figure 4.2,  $Q$  and a prefix of  $C$  1171  
are similar, but at different rates. In searching, we typically have a query  $Q$  and a longer 1172  
candidate  $C$ . We seek a prefix of  $C$  that is close to  $Q$ . For better comparison, we need 1173  
to eliminate the scaling effect. These observations demonstrate the necessity of uniform 1174  
scaling. 1175

DTW and US are used to achieve different kinds of invariance. DTW handles local 1176  
distortion, while US handles global scaling. Furthermore, some studies show that the 1177  
combination of US and DTW, namely USDTW, better reflects similarity [31, 79, 80]. US 1178  
is first applied to transform the two time series into the same length to eliminate the effect 1179  
resulting from the different rates. Then, DTW, rather than ED, is applied to address 1180  
local misalignment. USDTW is computationally more expensive than DTW because it 1181  
involves the calculation of the DTW between  $Q$  and different lengths of each prefix of  $C$ . 1182  
The different lengths of the prefixes correspond to different scaling factors. 1183

It is not uncommon for the data sampling strategy to change over time [2]. There are 1184  
different phases, each with its own rate. To achieve invariance for this kind of scaling effect 1185  
resulting from multiple rates, rather than using a single scaling factor, it is beneficial to 1186  
identify these different phases and use the appropriate scaling factors for these segments, 1187  
also known as pieces. We refer to this as piecewise scaling (PS). Figure 4.3 shows the 1188  
intuition of PS. The prefix of  $C$  (i.e.,  $C(1 : k)$ ) and  $Q$  share the same set of segments, 1189  
but each has a different scaling. Multiple scaling factors must be used. It motivates us 1190

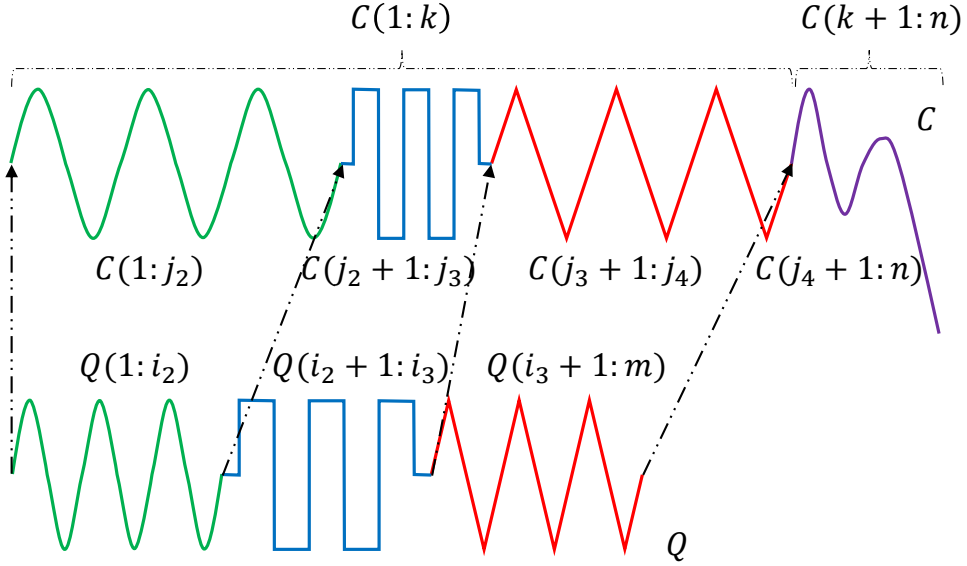


Figure 4.3: Intuition of piecewise scaling (PS).

1191 to design a new distance measure or framework that considers applying a scaling factor  
 1192 on each of the phases as defined by dashed lines in Figure 4.3, during the comparison of  
 1193 two time series.

1194 Our contributions are as follows:

- 1195 • We propose the first framework to achieve piecewise scaling (PS) invariance. In  
 1196 particular, we focus on two instantiations of PSD, namely PSED (i.e., ED with PS  
 1197 invariance) and PSDTW (i.e., DTW with PS invariance).
- 1198 • We design a dynamic programming method to compute PSD.
- 1199 • We propose a constrained version of PSD (cPSD) based on the allowed segment  
 1200 lengths. Besides, two other speedup techniques have been proposed. For a partic-  
 1201 ular instantiation of PSD, PDTW, we demonstrate the usage of a lower bound to  
 1202 further speed it up.
- 1203 • We demonstrate that the segmentation results returned by PSD can improve the  
 1204 accuracy of other distance measures.

1205 The rest of this paper is structured as follows. We present related work in Section 5.2  
 1206 and preliminaries in Section 4.3. Section 5.3 introduces our new distance measure frame-  
 1207 work, its constrained version, and speedup techniques. It is experimentally demonstrated  
 1208 in Section 4.5 for the problem of querying. In Section 5.5, we conclude this study with  
 1209 some future work.

## 4.2 Related Work

1210

This study focuses on distance measures of time series. For the overall review of time 1211 series, we direct the readers to [32, 28] for a more comprehensive understanding of this 1212 field. 1213

For many tasks, having appropriate distance measures that align with our intuition 1214 for the domains we work with is essential. One well-known distance measure is Dynamic 1215 Time Warping (DTW). It is initially designed for speech analysis [74]. However, DTW 1216 is computationally expensive. Lower bounds are used to speed up time series similarity 1217 search by admissibly pruning the unpromising candidates. One of the popular exact 1218 lower bounds of DTW is  $LB_{Keogh}$ . [70] improves the scalability of DTW by introducing a 1219 subsequence search suite of their four novel ideas, namely the UCR suite. For an overall 1220 review of lower bounds, we refer readers to [85, 81]. There is an approximate algorithm 1221 that approximates DTW with high accuracy while drastically cutting down the time and 1222 space requirements [75]. 1223

While ED is sensitive to distortions in the time axis, uniform scaling (US) has been 1224 shown to be a critical invariance in domains such as motion capture. [43] demonstrated 1225 that DTW is insufficient for handling global scaling effects, and that identifying DTW is 1226 not the solution to achieve this kind of invariance. There is a need for US. [93] extends 1227 the importance of uniform scaling to motif discovery. The authors show that meaningful 1228 motifs often suffer from a global scaling effect, causing standard motif finding algorithms 1229 to miss them completely. 1230

To the best of our knowledge, three studies analyze the combination of US and DTW, 1231 namely USDTW. It was first proposed by [31]. It extended  $LB_{Keogh}$  to bound the US- 1232 DTW. However, the extended  $LB_{Keogh}$  is still too loose with invariance to large amounts 1233 of uniform scaling. [79] and its follow-up study [80] proposed a new lower bound, namely 1234  $LB_{Shen}$ <sup>1</sup>, which has been shown to be tighter than  $LB_{Keogh}$  on USDTW. 1235

To our surprise, despite a fruitful discussion of DTW, US, and USDTW, no study has 1236 proposed a distance measure capable of handling scaling effects across multiple scaling 1237 factors. This is precisely what we will address in this study. 1238

## 4.3 Preliminaries

1239

We refer to time as the contextual attribute because it provides the context for the mea- 1240 surements to be made. We refer to the measurements as the behavioral attributes. Time 1241 series are multivariate when more than one behavioral attribute is present. Otherwise, it 1242 is called univariate. We focus on the univariate case. 1243

---

<sup>1</sup>It is denoted as  $LB_{New}$  in the original study. We rename it to prevent any confusion.

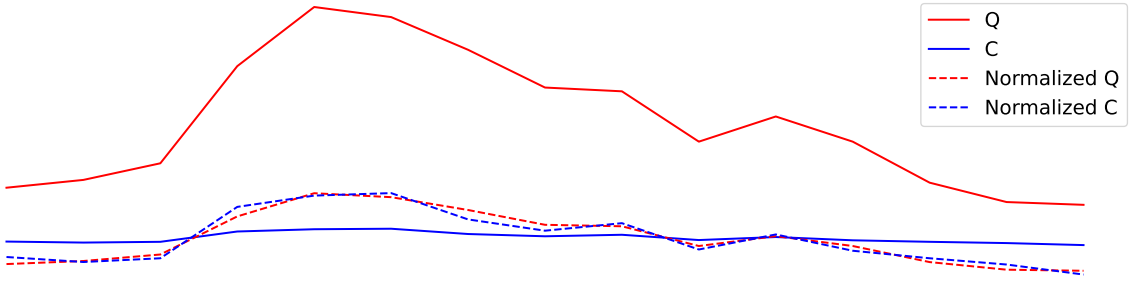


Figure 4.4: Z-normalization. Resulting time series have mean = 0 and std = 1.

1244 **Definition 1** (Time Series). A time series  $T = t_1, t_2, \dots, t_n$  is a sequence of real-valued  
1245 numbers with length =  $n$ .

1246 When two time series are involved in the discussion, we denote them as  $Q$  (Query)  
1247 and  $C$  (Candidate), with lengths  $m$  and  $n$ , respectively. Since  $Q$  is the query sequence,  
1248 it is not longer than  $C$  (i.e.,  $m \leq n$ ). The requirement of “ $m \leq n$ ” is a natural setting.  
1249 In “Query by Content”, a user is going to search for a candidate in the database from a  
1250 user-input query in which the query may only contain partial information of the target  
1251 candidate. For example, a user often wants to find a song or tune that is lingering in  
1252 their head by humming a part but not whole of the tune [103]. We are also interested in  
1253 a segment or subsequence of a time series.

1254 **Definition 2** (Subsequence). A subsequence  $T(i : j)$  of a time series  $T$  is a shorter time  
1255 series that starts from position  $i$  and ends at position  $j$  with length =  $j - i + 1$ . Both  
1256 ends are inclusive. Formally,  $T(i : j) = t_i, t_{i+1}, \dots, t_j$ ,  $1 \leq i \leq j \leq n$ .

1257 We call  $T(1 : j)$  the prefix of  $T$  of length  $j$ .

1258 Before comparison, we need to standardize or normalize them. A common way is  
1259 Z-Normalization, which is  $T = (T - \text{mean}(T)) / \text{std}(T)$ , as shown in Figure 4.4. The most  
1260 fundamental distance measure is the Euclidean Distance (ED).

### 1261 4.3.1 Euclidean Distance (ED)

1262 Given two points on a plane, it is intuitive to define the distance between them as the  
1263 length of the line segment between them. This idea extends to the case of  $n$ -dimensions  
1264 in time series with length  $n$ .

1265 **Definition 3** (Euclidean Distance (ED)). Given two series  $Q$  and  $C$  both with length  $n$ ,  
1266 the Euclidean Distance between them is defined as:

$$\text{ED}(Q, C) = \sqrt{\sum_{i=1}^n (q_i - c_i)^2} \quad (4.1)$$

A square root is usually involved in the computation of distance measures. It is a <sub>1267</sub> monotonic function. Since it does not change the relative ranking of the results, we can <sub>1268</sub> omit the square root operation for simplicity and optimization. ED aligns the entries <sub>1269</sub> between two series in a one-to-one manner. Two similar series will have a large distance <sub>1270</sub> under ED if they are not aligned well in the time dimension. ED cannot handle local <sub>1271</sub> distortion along the time axis because warping in the alignment is not allowed. A stan- <sub>1272</sub> dard distance measure that provides warping invariance is called Dynamic Time Warping <sub>1273</sub> (DTW). <sub>1274</sub>

### 4.3.2 Dynamic Time Warping (DTW)

Dynamic Time Warping (DTW) is an algorithm that measures similarity between two <sub>1276</sub> time series while accounting for local distortions. DTW aligns the two series by nonlin- <sub>1277</sub> early warping the time axis to minimize the final cumulative distance. <sub>1278</sub>

Given two time series,  $Q$  and  $C$ , we first construct an  $m$  by  $n$  distance matrix  $M$ . <sub>1279</sub> The origin  $(1, 1)$  is set at the bottom-left element of  $M$ . The  $(i, j)$  element of  $M$  <sub>1280</sub> contains the distance  $d(q_i, c_j)$  between points  $q_i$  and  $c_j$ . This local distance  $d(\cdot, \cdot)$  is <sub>1281</sub> usually calculated by  $(q_i - c_j)^2$ . Each  $(i, j)$  element refers to an alignment or mapping <sub>1282</sub> of the two points. A contiguous set of such elements forms a warping path  $W$ .  $W$  <sub>1283</sub> represents the non-linear alignment of  $Q$  and  $C$ .  $W = w_1, w_2, \dots, w_K$  in which  $w_k = (i, j)_k$  <sub>1284</sub> represents the mapping between  $q_i$  in  $Q$  and  $c_j$  in  $C$ , where  $\max(m, n) \leq K \leq m + n - 1$ . <sub>1285</sub> “ $\max(m, n) \leq K$ ” because the alignment of two series must include every point in both  $Q$  <sub>1286</sub> and  $C$ . “ $K \leq m + n - 1$ ” because the longest warping path is either the “concatenation of <sub>1287</sub> the bottom row and the rightmost column” (with the bottom-right cell being overlapped) <sub>1288</sub> or the “concatenation of the leftmost column and the top row” (with the top-left cell being <sub>1289</sub> overlapped). <sub>1290</sub>

The warping path  $W$  is typically subject to the following three constraints. <sub>1291</sub>

- Boundary conditions:  $w_1 = (1, 1)$  and  $w_K = (m, n)$ . The first (last) point of  $Q$  <sub>1292</sub> must map to that of  $C$ . <sub>1293</sub>
- Continuity: Given  $w_k = (i, j)$  and  $w_{k-1} = (i', j')$ ,  $i - i' \leq 1$  and  $j - j' \leq 1$ . An <sub>1294</sub> entry in the warping path  $W$  is adjacent to its one-step previous entry. <sub>1295</sub>
- Monotonicity: Given  $w_k = (i, j)$  and  $w_{k-1} = (i', j')$ ,  $i - i' \geq 0$  and  $j - j' \geq 0$ . The <sub>1296</sub> warping path  $W$  does not go back. <sub>1297</sub>

We denote  $W^*$  as a set of all allowed possible paths. <sub>1298</sub>

**Definition 4** (Dynamic Time Warping (DTW) [74]). DTW returns the minimum warp- <sub>1299</sub> ing cost: <sub>1300</sub>

$$\text{DTW}(Q, C) = \min_{W \in W^*} \sum_{k=1}^{|W|} w_k \quad (4.2)$$

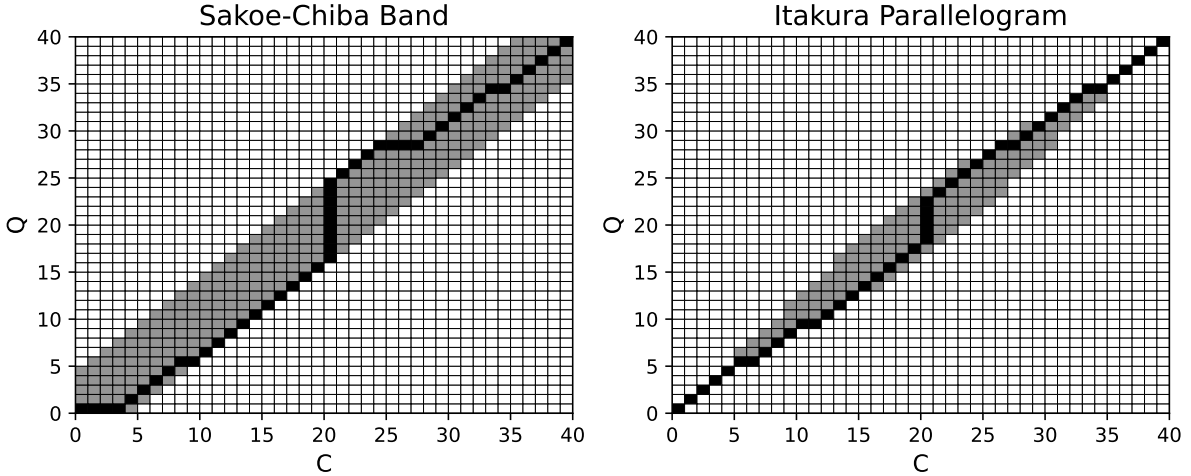


Figure 4.5: Visualization of  $D$  with local constraints. The black cells form the warping path.

To find the minimum warping cost and its corresponding warping path, we can use dynamic programming (DP) to evaluate the following recurrence.

$$D(i, j) = d(q_i, c_j) + \min \begin{cases} D(i - 1, j - 1), \\ D(i - 1, j), \\ D(i, j - 1) \end{cases} \quad (4.3)$$

It can be solved by building the accumulated cost matrix  $D$ , where the y-axis refers to  $Q$ , and the x-axis refers to  $C$ . The base cases, which are the first row and the first column, are defined as  $D(1, j) = \sum_{k=1}^j d(q_1, c_k), j \in [1, n]$  and  $D(i, 1) = \sum_{k=1}^i d(q_k, c_1), i \in [1, m]$ . After we have initialized the base cases, we can fill up  $D$  starting from the bottom up. There are  $m \times n$  entries in  $D$ . It takes  $\mathcal{O}(mn)$  to fill it up. Once  $D$  is built, we can find the path corresponding to this minimum cost by simple backtracking from the end cell  $D(m, n)$  to the origin cell  $D(1, 1)$ .

Some constraints have been proposed to prevent pathological warping paths with the aim of accuracy and efficiency. Two of the most popular are Sakoe-Chiba Band [74] and Itakura Parallelogram [39]. They only allow the warping paths to pass through the allowed region, as shown in Figure 4.5, by setting the cells outside this region in  $D$  to have  $\infty$  accumulated distance cost. [44] suggested that these constraints can be viewed as constraints on the warping path entry  $w_k = (i, j)_k$ . It represents these constraints as inequalities applying to the indices  $i$  and  $j$  locally, without depending on the main diagonal in  $D$ . In the Sakoe-Chiba Band, the constraints can be represented as  $j - r \leq$

$i \leq j + r$ , where  $r$  is an integer. It is sometimes specified as a fraction (or percentage) 1318 of the longer time series length to ensure length invariance. For clarity, we assume  $r$  is 1319 an integer unless specified otherwise. This means that  $q_i$  can only align with  $c_j$  if their 1320 indices differ by at most  $r$ . Since  $r$  defines the maximum allowed difference between the 1321 mapping indices,  $|n - m| \leq r$ , to ensure that the end points of  $Q$  and  $C$  can map. In 1322 the Itakura Parallelogram,  $r$  is a function of  $i$  rather than a constant value. ED can 1323 be seen as a special case of DTW where the warping path is fixed to be diagonal.  $q_i$  1324 aligns to  $c_i$  for every  $i$  (i.e.,  $r = 0$ ). DTW minimizes over all possible warping paths, 1325 and the warping path of ED is one of them. Because of the band, we only need to fill 1326 up the cells within the band. The complexity is  $\mathcal{O}(\#\text{of\_cells\_inside})$ . In the case of the 1327 Sakoe-Chiba Band, the band has a constant width  $w = 2r + 1$ . The complexity becomes 1328  $\mathcal{O}(w \times \text{length\_of\_diagonal}) = \mathcal{O}(rn)$ . The constrained DTW is denoted as  $\text{DTW}_r$ . 1329

### 4.3.3 Uniform Scaling (US)

In US, we compare the whole sequence of  $Q$  to a prefix of  $C$ , as shown in Figure 4.2. 1331 The two compared sequences are scaled to the same length via interpolation before ED 1332 is applied. A common interpolation method is nearest neighbor interpolation. 1333

**Definition 5** (Nearest Neighbor Interpolation). Given a time series  $T$  of length  $n$  and 1334 an integer  $L$ , Nearest Neighbor Interpolation scales  $T$  into  $T^L$  as follows: 1335

$$T_j^L = T_{\lceil n(j/L) \rceil} \quad \text{where } 1 \leq j \leq L \quad (4.4)$$

We can scale up or down a given series using Equation 4.4, as shown in Example 1. 1336

**Example 1.** Given a series  $T = 1, 2, \dots, 6$  with length  $n = 6$ . Let  $T(1 : 4)$  be the prefix 1337 of  $T$  of length  $k = 4$  (i.e.,  $T(1 : 4) = 1, 2, 3, 4$ ). Given an integer  $L = 8$ , we compute 1338  $T(1 : 4)^8$  as follows. 1339

$$\begin{aligned} T(1 : 4)^8 &= T_{\lceil 4(1/8) \rceil}, T_{\lceil 4(2/8) \rceil}, T_{\lceil 4(3/8) \rceil}, \dots, T_{\lceil 4(8/8) \rceil} \\ &= T_1, T_1, T_2, \dots, T_4 \\ &= 1, 1, 2, \dots, 4. \end{aligned}$$

When  $L > k$ ,  $T$  is said to be stretched. When  $L < k$ ,  $T$  is said to be shrunk. 1340

**Definition 6** (Uniform Scaling (US) [43]). Given two series  $Q$  and  $C$ , of length  $m$  and 1341  $n$  respectively, and a scaling factor bound  $l$ , where  $l \geq 1$ . Let  $C(1 : k)$  be the prefix of 1342  $C$ , where  $\lceil m/l \rceil \leq k \leq \min(\lfloor lm \rfloor, n)$ , and  $C(1 : k)^L$  be a rescaled version of  $C(1 : k)$  with 1343 length  $L$ , where  $L = \min(\lfloor lm \rfloor, n)$ .  $L$  is called the alignment factor.  $\min(\lfloor lm \rfloor, n)$  is the 1344

1345 largest alignment factor.

$$\text{US}(Q, C, l, L) = \min_{k=\lceil m/l \rceil}^{\min(\lfloor lm \rfloor, n)} \text{ED}(Q^L, C(1:k)^L) \quad (4.5)$$

1346  $L$  is set as the largest alignment factor [80] to ensure all the points in  $Q$  and  $C(1:k)$  are  
1347 preserved during interpolation because of up-sampling, and the scaled version of all the  
1348 prefixes is going to have the same length (i.e.,  $L$ ), for fair comparison, since comparison  
1349 between two longer time series generally results in a larger distance measure. Through  
1350 Equation 4.5, we find the minimum value and the corresponding argument (i.e.,  $k$ ) by  
1351 checking the minimum value of the ED function from  $\lceil m/l \rceil$  to  $\min(\lfloor lm \rfloor, n)$ . The scaling  
1352 factor is defined by the argument minimum value of  $k$ . The smaller  $k$  is, the more we  
1353 need to “stretch”  $C$  for  $Q$  to compare with  $C(1:k)$ , which is  $m/k$  times.

1354 Consider a time series database  $D$  comprising a set of candidate instances, and a  
1355 single query series  $Q$ . The search task aims to retrieve the most similar instance (or  
1356 top- $k$  instances) from  $D$  to  $Q$ . We maintain  $Q$  as a fixed reference and extract only the  
1357 prefixes from each instance in  $D$  for comparison. Furthermore, to simplify notation, we  
1358 apply scaling exclusively to the instances in  $D$ , leaving  $Q$  unscaled.

#### 1359 4.3.4 Uniform Scaling & Dynamic Time Warping (USDTW)

1360 Uniform Scaling & Dynamic Time Warping (USDTW) measures the similarity by applying  
1361 scaling with an appropriate scaling factor on  $C$  and then applying DTW. The tail  
1362 part of  $C$  can be ignored, as shown in Figure 4.2.

1363 **Definition 7** (Uniform Scaling & Dynamic Time Warping (USDTW) [80]). With the  
1364 same notations defined in Definition 6,

$$\text{USDTW}_r(Q, C, l, L) = \min_{k=\lceil m/l \rceil}^{\min(\lfloor lm \rfloor, n)} \text{DTW}_r(Q^L, C(1:k)^L) \quad (4.6)$$

1365 where  $r$  is the DTW constraint parameter.

1366 We replace the ED function in Equation 4.5 by DTW function to form Equation 4.6.  
1367 As mentioned in Section 5.1, there may exist more than one scaling factor. Hence,  
1368 both the existing distance measures, US and USDTW, which are designed to handle  
1369 only one scaling factor, are insufficient. This motivates us to design a new framework of  
1370 distance measures.

### 4.3.5 Lower Bounds for DTW and USDTW

1371

We first introduce the concept of lower bounds and explain how they can benefit search. 1372  
 DTW is computationally more expensive than ED. They compute an accumulated cost 1373  
 matrix of size  $m \times n$ , where  $m$  and  $n$  denote the lengths of the two time series. It 1374  
 results in quadratic complexity. This complexity poses a challenge for similarity search. 1375  
 The most common approach is to compute a lower bound of the real value, which is 1376  
 computationally cheap and tight. We can use this lower bound to filter out unpromising 1377  
 candidates and perform the expensive distance computation only on the small set of 1378  
 promising candidates. In searching, we would keep track of the best\_so\_far distance bsf 1379  
 between the query  $Q$  and the testing candidates. When testing a new candidate  $C$ , we 1380  
 first compute the  $\text{LB}(Q, C)$ . We only compute the actual DTW when  $\text{LB}(Q, C) \leq \text{bsf}$ . 1381

We then introduce some common lower bounds. 1382

**Kim Lower Bound [46]:**  $\text{LB}_{\text{Kim}}$  is a simple and fast lower bound of DTW. The 1383  
 complexity is  $O(1)$ . It uses the four features in  $Q$  and  $C$ . We denote  $t_{-1}$  as the last point 1384  
 and  $t_{\max}$  ( $t_{\min}$ ) as the maximum (minimum) point in time series  $T$ . 1385

$$\text{LB}_{\text{Kim}} = \max \begin{cases} d(q_1, c_1) \\ d(q_{-1}, c_{-1}) \\ d(q_{\max}, c_{\max}) \\ d(q_{\min}, c_{\min}) \end{cases} \quad (4.7)$$

$d(\cdot, \cdot)$  refers to the local distance used in the point alignment. The first two lines come 1386  
 from the boundary condition in DTW. The alignment between the first pair of points and 1387  
 the last pair of points must contribute to the accumulated sum of DTW. Each point in 1388  
 $Q$  must align with some point in  $C$ , and vice versa. Each alignment contributes a local 1389  
 distance to the final sum. The minimum possible local distance for the alignment of  $q_{\max}$  1390  
 would be the one aligned with  $c_{\max}$ . The same applies to the last line in the equation. 1391

There is a simplification of  $\text{LB}_{\text{Kim}}$ . Only the first and last pair are used in the lower 1392  
 bound computation. In the normalized time series, the third and fourth rows in Equa- 1393  
 tion 4.7 should have small values [70]. Ignoring them can improve the complexity from 1394  
 $\mathcal{O}(n)$  to  $\mathcal{O}(1)$ . The simplified lower bound is  $\text{LB}_{\text{KimFL}} = d(q_1, c_1) + d(q_{-1}, c_{-1})$ . 1395

**Keogh Lower Bound [44]:**  $\text{LB}_{\text{Keogh}}$  builds the upper  $U$  and lower envelopes  $L$  of 1396  
 one of the time series out of the two compared sequences. Usually, the envelopes are 1397  
 constructed for  $Q$  instead of  $C$  as we will compare one  $Q$  against many  $C$ 's. Otherwise, 1398  
 we need to build the envelopes for each candidate instead [70]. 1399

To the best of our knowledge, they are the first to interpret the constraint as a 1400  
 restriction on the indices of the warping path  $w_k = (i, j)_k$  such that  $j - r \leq i \leq j + r$ , 1401  
 where  $r$  defines the allowable deviation of alignment between  $q_i$  and  $c_j$ . For ease of 1402

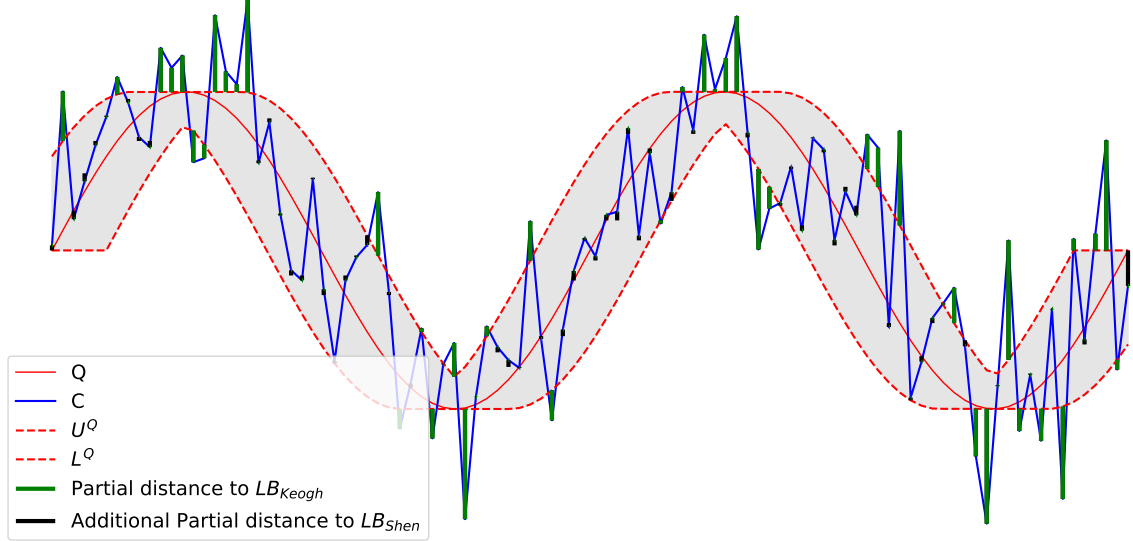


Figure 4.6: Visualization of LB<sub>Keogh</sub> and LB<sub>Shen</sub>

exposition, we focus on the most used constraint in the literature, which is the Sakoe-Chiba Band [84]. Two sequences are constructed for \$Q\$, namely the upper \$U^Q\$ and lower envelopes \$L^Q\$ of \$Q\$ as shown in Figure 4.6. For each \$q\_i\$, we would assign a window of \$q\_i\$ based on its index \$i\$ as follows.

$$\begin{aligned} U_i^Q &= \max(q_{\max(1,i-r)} : q_{\min(i+r,m)}) \\ L_i^Q &= \min(q_{\max(1,i-r)} : q_{\min(i+r,m)}) \end{aligned} \quad (4.8)$$

$\max(1, \cdot)$  and  $\min(\cdot, m)$  are used for handling the boundary cases. \$U^Q\$ and \$L^Q\$ together form a bounding envelope that encloses the original \$Q\$, it is the grey region in the figure. For each \$c\_j\$, either \$(c\_j, U\_j^Q)\$ or \$(c\_j, L\_j^Q)\$ corresponds to the possible alignment that contributes the minimum distances if \$c\_j\$ falls outside the envelope. Herein, the lower bound is the sum of these distances, as shown in the following equation.

$$LB_{Keogh}(Q, C) = \sum_{j=1}^n \begin{cases} d(c_j, U_j^Q) & \text{if } c_j > U_j^Q \\ d(c_j, L_j^Q) & \text{if } c_j < L_j^Q \\ 0 & \text{otherwise} \end{cases} \quad (4.9)$$

Visually, these distances are the distances between \$c\_j\$ outside the envelope and the vertically corresponding points on the envelope. The distances are the green bars in the figure. Equation 4.9 returns the sum of the green bars.

**Shen Lower Bound [79, 80]:** It leverages the boundary and continuity conditions to create a lower bound of DTW. It can be used to lower-bound the USDTW with slight modification. The intuition is to find the minimum possible alignment of each \$c\_j\$ with

points in  $Q$ , subject to the local constraint  $r$  from DTW and the global constraint  $l$  from US. 1418  
1419

We will first introduce  $\text{LB}_{\text{Shen}}$  for DTW. Given the candidate sequence  $C$  with length  $n$ , for each  $c_j$ , we create its possible reach  $\mathbf{q}_j$  in  $Q$  under DTW as in Equation 4.10. The elements  $\mathbf{q}_j$  form an indexed collection  $\mathbb{Q} = (\mathbf{q}_1, \mathbf{q}_2, \dots, \mathbf{q}_{\min(\lfloor lm \rfloor, n)})$ . 1420  
1421  
1422

$$\mathbf{q}_j = (q_{\max(1, j-r)}, \dots, q_{\min(j+r, m)}) \quad (4.10)$$

We define  $\delta(x, Y) = \min_{y \in Y} d(x, y)$ . The possible minimum cost contributed by the alignment of  $c_j$  and some point in  $Q$  to the accumulated sum would be  $\delta(c_j, \mathbf{q}_j)$ . The lower bound  $\text{LB}_{\text{Shen}}$  is defined as: 1423  
1424  
1425

$$\text{LB}_{\text{Shen}}(Q, C) = d(c_1, q_1) + \sum_{j=2}^{n-1} \delta(c_j, \mathbf{q}_j) + d(c_n, q_m) \quad (4.11)$$

We direct the reader to [79] for the formal proof, while an intuition of the proof is presented here. There are three items on the right-hand side of Equation 4.11. The continuity requirement ensures that each  $c_i$  is involved in at least one alignment. The first and the last items are from the boundary condition. The middle item returns the possible minimum distances contributed by each  $c_j$ 's, where  $2 \leq j \leq n - 1$ . It is obvious that  $\text{LB}_{\text{Shen}}$  in Equation 4.11 is tighter when we use the first pair of points and the last pair of points instead of doing the middle summation all from  $j = 1$  to  $n$ . It is because the distance contributed by the first pair (last pair) must be greater than  $\delta(c_1, \mathbf{q}_1)$  ( $\delta(c_n, \mathbf{q}_n)$ ). 1426  
1427  
1428  
1429  
1430  
1431  
1432  
1433

It is proven that it is tighter than  $\text{LB}_{\text{Keogh}}$  [79]. It is shown in Figure 4.6 visually. The black bars refer to the additional lower bound distance sum on top of  $\text{LB}_{\text{Keogh}}$ . We will give an intuitive proof here. Both  $\text{LB}_{\text{Keogh}}$  and  $\text{LB}_{\text{Shen}}$  compute the lower bounds by summing the local distance resulting from the alignment of each  $c_j$  with some points in  $Q$ , which is guaranteed to be not greater than the partial distance contributed by the real alignment, which we only know until we compute the exact distance measure. In  $\text{LB}_{\text{Keogh}}$ , if this  $c_j$  falls outside the envelope, this local distance is the vertical distance between  $c_j$  and the envelope. If  $c_j$  falls inside, this local distance would be 0. For those points outside the envelope, the local distances for  $c_j$  of  $\text{LB}_{\text{Keogh}}$  and  $\text{LB}_{\text{Shen}}$  are the same. But  $\text{LB}_{\text{Shen}}$  aims to return the minimum possible partial distance for each  $c_j$ , even within the envelope. Hence,  $\text{LB}_{\text{Keogh}} \leq \text{LB}_{\text{Shen}}$ . 1434  
1435  
1436  
1437  
1438  
1439  
1440  
1441  
1442  
1443  
1444

In order to compute Equation 4.11 efficiently, we first sort sequences  $\mathbf{q}_j$  and the resulting sorted sequences are denoted as  $\tilde{\mathbf{q}}_j$ . The sorted sequences allow us to do a binary search when we are calculating  $\delta(c_j, \tilde{\mathbf{q}}_j)$  in contrast to  $\delta(c_j, \mathbf{q}_j)$ . The sorting only needs to be done once because we are testing the same  $Q$  with different candidates. 1445  
1446  
1447  
1448

It can be extended to the USDTW case [79, 80]. The possible reach now is not only defined by  $r$ , but also by the scaling factor bound  $l$ . 1449  
1450

$$\mathbf{q}_j = (q_{\max(1, \lceil j/l \rceil - r)}, \dots, q_{\min(\lfloor j/l \rfloor + r, m)}) \quad (4.12)$$

[79] proves the following theorem to allow us to consider the lower bound between each prefix of  $C$  and  $Q$  without the scaling up of each prefix of  $C$  (i.e.,  $C(1 : k)^L$ ) and the scaling up of  $Q$  (i.e.,  $Q^L$ ).

**Theorem 8.** *For any  $\lceil m/l \rceil \leq k \leq \min(\lfloor lm \rfloor, n)$ ,  $\text{DTW}_r(Q^{\min(\lfloor lm \rfloor, n)}, C(1 : k)^{\min(\lfloor lm \rfloor, n)})$  is always lower bounded by  $\sum_{j=1}^k \delta(c_j, \mathbf{q}_j)$ .*

Recall that USDTW calculates DTW distances between each rescaled prefix of  $C$  to the rescaled  $Q$ , and outputs the minimum DTW distance, as in Equation 4.6. The incremental nature of the lower bound frees us to calculate the lower bound of each DTW distance from scratch. This theorem allows us to first calculate the lower bound of the shortest prefix  $C(1 : \lceil m/l \rceil)$  of  $C$  and  $Q$ , and then incrementally calculate the lower bound of the longer prefix with length from  $\lceil m/l \rceil + 1$  to  $\min(\lfloor lm \rfloor, n)$  by adding on each  $\delta(c_j, \mathbf{q}_j)$ . To note, it also means that if  $\text{LB}_{\text{Shen}}(Q, C(1 : k))$  is larger than a value, namely bsf,  $\text{LB}_{\text{Shen}}(Q, C(1 : k'))$ , where  $k' > k$ , would also be larger than bsf. To note, we can tighten  $\text{LB}_{\text{Shen}}$  by using  $d(c_1, q_1)$  instead of  $\delta(c_1, \mathbf{q}_1)$ .

The above analysis can also apply to the case of US distance. We only need to define the corresponding reaches as follows:

$$\mathbf{q}_j = (q_{\max(1, \lceil j/l \rceil)}, \dots, q_{\min(\lfloor j/l \rfloor, m)}) \quad (4.13)$$

## 4.4 Piecewise Scaling Distance

The motivation stems from the limitations of US and USDTW. They assume that the relationship between  $Q$  and  $C$  is governed by only a single, global scaling factor. This assumption fails when applied to multi-rate data, where different phases of the time series express at different rates.

Note that existing studies [43, 70] can find all scaling factors, defined by the chosen prefix of  $C$ , ranging from  $\lceil m/l \rceil$  to  $\min(\lfloor lm \rfloor, n)$ . However, they can use only one of them in the scaling. Consider the following illustrative example in ASCII text [70], where character repetition represents the duration of spoken phonemes, and space indicates a pause:

- “time series 20 25” and “time series 20 25”. Here, the Hamming distance (the discrete analogue of ED) fails due to misalignment in the underlined locations, but the string edit distance (the discrete analogue of DTW) can resolve it.
- “time sseerriiss 222000222555”. This sequence exhibits three distinct phases with scaling factors of 1, 2, and 3, respectively. The corresponding invariance cannot be

achieved by DTW or US (which is restricted to a single global scalar). US would 1482  
enforce a single compromised global scale instead. 1483

In Query-by-Content scenarios, such as query-by-humming or gesture retrieval, the 1484  
query is generated by a human. Humans do not maintain a consistent rate for each 1485  
phase. For example, humans rush through a familiar sequence but slow down for a 1486  
new or complex sequence. It is commonly observed in a piece of music performed by a 1487  
beginner. The piece's tempo is not uniform. 1488

We introduce a novel distance measure framework, termed Piecewise Scaling Distance 1489  
(PSD). It addresses the local scaling effect within each phase by employing a scaling factor 1490  
to each phase, instead of using a single scaling factor for the whole time series. It releases 1491  
the basic constraint or assumption made in US and USDTW. PSD employs an existing 1492  
distance metric, such as ED or DTW, to quantify the similarity of aligned segment pairs. 1493  
While the PSD framework is agnostic to the underlying metric, this study focuses on its 1494  
two fundamental instantiations: 1495

- PSED, which employs ED to compute the similarity of aligned segment pairs. 1496
- PSDTW, which employs DTW to compute the similarity of aligned segment pairs. 1497

In the formulation that follows, we utilize PSDTW as the running example. PSDTW 1498  
generalizes PSED. The PSED formulation can be trivially derived from it. 1499

#### 4.4.1 Piecewise Scaling & Dynamic Time Warping (PSDTW) 1500

**Problem formulation:** To simplify the discussion, we focus on the comparison between 1501  
 $Q$  and the entire sequence  $C$ , rather than a prefix of  $C$ . Note that this formulation can 1502  
be generalized to prefix matching as in Definition 6 and Definition 7. 1503

Given two sequences  $Q$  and  $C$ , where  $Q$  is not longer than  $C$ ,  $|Q| = m \leq |C| = n$ , and 1504  
the number of segments or pieces  $P$  allowed, our goal is to segmentalize both  $Q$  and  $C$  1505  
into  $P$  contiguous segments automatically in a way that minimize the total sum of DTW 1506  
distance of aligned segment pairs with interpolation. 1507

**Definition 9** (Piecewise Scaling & Dynamic Time Warping (PSDTW)). With the same 1508  
notations defined in Definition 7, 1509

$$\begin{aligned} \text{PSDTW}_r(Q, C, l, L, P) = \\ \min_{\substack{i_1 < i_2 < \dots < i_{P+1} \\ j_1 < j_2 < \dots < j_{P+1}}} \sum_{p=1}^P \text{DTW}_r(Q(i_p + 1 : i_{p+1})^L, \\ C(j_p + 1 : j_{p+1})^L) \end{aligned} \quad (4.14)$$

, where  $i_1 = 0$ ,  $i_{P+1} = m$ ,  $j_1 = 0$ ,  $j_{P+1} = n$  and the setting of  $L$  will be discussed later. 1510

---

**Algorithm 1** Naive PSDTW

---

**Input:** Query series  $Q$ , Candidate series  $C$ , DTW constraint parameter  $r$  (in fraction), Number of pieces  $P$ , Scaling parameter  $L$

**Output:** Distance Matrix  $D$  of size  $(m + 1) \times (n + 1) \times (P + 1)$

```
1: Initialize  $D$  with  $\infty$ 
2:  $D[0, 0, 0] \leftarrow 0$ 
3: for  $p \leftarrow 1$  to  $P$  do
4:   for  $i \leftarrow 1$  to  $m$  do
5:     for  $j \leftarrow 1$  to  $n$  do
6:        $D[i, j, p] \leftarrow \min_{i' < i, j' < j} \{D[i', j', p - 1]$ 
          $+ \text{DTW}_r(Q(i' + 1 : i)^L, C(j' + 1 : j)^L)\}$ 
7: return  $D[m, n, P]$ 
```

---

**Algorithm 2** Line 6 in Algorithm 1

---

```
1: for  $i' \leftarrow 0$  to  $i - 1$  do
2:   for  $j' \leftarrow 0$  to  $j - 1$  do
3:      $dist_{\text{prev}} \leftarrow D[i', j', p - 1]$ 
4:      $dist_{\text{seg}} \leftarrow \text{DTW}_r(Q(i' + 1 : i)^L, C(j' + 1 : j)^L)$ 
5:      $D[i, j, p] \leftarrow \min(D[i, j, p], dist_{\text{prev}} + dist_{\text{seg}})$ 
```

---

1511     Essentially,  $L$  needs to be at least the length of all segments to preserve all the points  
1512     by up-sampling.

1513     We refer to Figure 4.3 to clarify Equation 4.14. Given two sequences  $Q$  and  $C$ , with the  
1514     aid of different colors and the dashed lines, we observe that  $Q$  consists of three segments  
1515     while  $C$  consists of four segments, with the first three segments of  $C$  similar to those  
1516     of  $Q$ . They form three segment pairs. The scaling factor used in each segment pair is  
1517     determined from the length of the two subsequences involved, i.e.,  $(i_{p+1} - i_p)/(j_{p+1} - j_p)$ .  
1518     These three parts have different scaling factors. For example, the first part in  $C$  is the  
1519     stretched version of that in  $Q$ . The second part in  $C$  is the compressed version of that in  
1520      $Q$ .

1521     Equation 4.14 can be formulated in a recurrence relation as follows. Let  $D[i, j, p]$  be  
1522     the minimum cost to align the first  $i$  points in  $Q$  (i.e.,  $Q(1 : i)$ ) with the first  $j$  points in  
1523      $C$  (i.e.,  $C(1 : j)$ ) using exactly  $p$  segments:

$$D[i, j, p] = \min_{\substack{i' < i \\ j' < j}} \left\{ D[i', j', p - 1] + \text{DTW}_r(Q(i' + 1 : i)^L, C(j' + 1 : j)^L) \right\} \quad (4.15)$$

1524 **Naive PSDTW:**

---

**Algorithm 3** Initialization of PSDTW

---

- 1:  $L_{\text{gmin}}^Q \leftarrow \lceil (m/P)/\sqrt{l} \rceil, \quad L_{\text{gmax}}^Q \leftarrow \lfloor (m/P)\sqrt{l} \rfloor$  ▷ “g” refers to “global”.
  - 2:  $L_{\text{gmin}}^C \leftarrow \lceil (n/P)/\sqrt{l} \rceil, \quad L_{\text{gmax}}^C \leftarrow \lfloor (n/P)\sqrt{l} \rfloor$
  - 3:  $L = \max(L_{\text{gmax}}^Q, L_{\text{gmin}}^C)$
  - 4: Initialize  $D$  of size  $(m+1) \times (n+1) \times (P+1)$  with  $\infty$
  - 5:  $D[0, 0, 0] \leftarrow 0$
- 

Our goal is  $D[m, n, P]$ . Equation 4.15 can be solved exactly by dynamic programming 1525 (DP). The base case is  $D[0, 0, 0] = 0$ . It refers to the zero cost to align the first 0 point 1526 (i.e., the empty prefix) of  $Q$  with that of  $C$ . Other cells in  $D$  are first initialized with  $\infty$ . 1527 They are calculated using a bottom-up approach via Equation 4.15. A straightforward 1528 implementation in DP is shown in Algorithm 1. Line 6 is achieved by looping all the 1529 previous indices of the current  $i$  and  $j$  as in Algorithm 2. 1530

We explain the lines in Algorithm 2. Line 3 retrieves the accumulated distance cost 1531 from the beginning up to the endpoints  $(i', j')$ , and saves it as  $dist_{\text{prev}}$ . Line 4 considers 1532 the current aligned segment pair, which consists of  $Q(i'+1 : i)$  and  $C(j'+1, j)$ , and they 1533 are interpolated to the length  $L$ . The DTW distance of this pair is calculated and saved 1534 as  $dist_{\text{seg}}$ . 1535

We now analyze the time complexity of Algorithm 1. There are  $Pmn$  entries in  $D$ . 1536 The  $\min$  operator in line 6 takes  $\mathcal{O}(mn)$ . Hence, the time complexity of Algorithm 1 1537 is  $\mathcal{O}(Pm^2n^2) = \mathcal{O}(Pn^4)$ , multiplied by the running time of the DTW. It is slow, which 1538 prevents us from using it in practice. To note, we use  $r$  in a fraction instead of a fixed 1539 integer here. This allows the deviation tolerance to scale adaptively with pieces of varying 1540 lengths. 1541

#### 4.4.2 Speedup Techniques

---

**Length constraints of the segment:** A way to reduce complexity and to prevent 1543 pathological segment pairs is to limit the possible segment lengths that are considered by 1544 constraining the minimum and maximum lengths of segments. It is similar to constrained 1545 DTW, in which we limit the search space of the warping path as in Figure 4.5. The 1546 version of PSDTW that considers the segment constraint is termed constrained PSDTW 1547 (cPSDTW). It is shown in Algorithm 4. The uncolored part shows the main logic, while 1548 the colored part shows the speedup techniques, which will be explained later. 1549

We initialize in Algorithm 3. For a given number of segments  $P$ , the expected length 1550 of each segment in  $Q$  and  $C$  would be  $m/P$  and  $n/P$ , respectively. For  $Q$ , we set the 1551 minimum possible segment length  $L_{\text{gmin}}^Q$  to be  $\lceil (m/P)/\sqrt{l} \rceil$  and the maximum possible 1552 length  $L_{\text{gmax}}^Q$  to be  $\lfloor (m/P)\sqrt{l} \rfloor$  in line 1 such that the scaling ratio of any two segments 1553 in  $Q$  would be bounded by  $l$ . It allows some deviation in the length of the segments from 1554 their expected length. Similarly, we compute the segment constraints for  $C$  in line 2. We 1555

---

**Algorithm 4** Constrained PSDTW (cPSDTW) with early abandoning and lower bounding

---

**Input:** Query series  $Q$ , Candidate series  $C$ , DTW constraint parameter  $r$  (in fraction), Number of pieces  $P$ , best\_so\_far bsf

**Output:** The final distance  $D[m, n, P]$  if  $D[m, n, P] \leq \text{bsf}$ , otherwise  $\infty$

- 1: Execute Algorithm 3 for initialization
- 2: **for**  $p \leftarrow 1$  **to**  $P$  **do**
- 3:   **for**  $i \leftarrow (p \cdot L_{\text{gmin}}^Q)$  **to**  $\min(p \cdot L_{\text{gmax}}^Q, m)$  **do** ▷ The iterations can be parallelized.
- 4:     **for**  $L^Q \leftarrow L_{\text{gmin}}^Q$  **to**  $L_{\text{gmax}}^Q$  **do**
- 5:        $i' \leftarrow i - L^Q$  ▷  $i'$ : End point of previous segment on  $Q$ .
- 6:        $Q' \leftarrow \text{rev}(Q(i' + 1 : i))$  ▷  $\text{rev}(T)$ : Reverse the input series  $T$ .
- 7:        $L_{\text{min}}^C \leftarrow \max(L_{\text{gmin}}^C, \lceil L^Q/l \rceil)$
- 8:        $L_{\text{max}}^C \leftarrow \min(\lfloor L^Q/l \rfloor, L_{\text{gmax}}^C)$
- 9:        $r' \leftarrow r \times \max(L^Q, L_{\text{max}}^C)$  ▷ Compute the integer value of  $r$ .
- 10:      **for**  $k \leftarrow 1$  **to**  $L_{\text{max}}^C$  **do**
- 11:        $\mathbf{q}_k \leftarrow (q'_{\max(1, \lceil k/l \rceil - r')}, \dots, q'_{\min(\lfloor k/l \rfloor + r', L^Q)})$  ▷ Construct indexed collection  $\mathbb{Q}$ .
- 12:        $\tilde{\mathbf{q}}_k \leftarrow \text{sort}(\mathbf{q}_k)$
- 13:       **for**  $j \leftarrow (p \cdot L_{\text{gmin}}^C)$  **to**  $\min(p \cdot L_{\text{gmax}}^C, n)$  **do**
- 14:         **for**  $L^C \leftarrow L_{\text{min}}^C$  **to**  $L_{\text{max}}^C$  **do**
- 15:            $j' \leftarrow j - L^C$
- 16:            $C' \leftarrow \text{rev}(C(j' + 1 : j))$
- 17:            $dist_{\text{prev}} \leftarrow D[i', j', p - 1]$
- 18:           **if**  $dist_{\text{prev}} = \infty$  **then**
- 19:             **continue**
- 20:           **if**  $dist_{\text{prev}} > \text{bsf}$  **then**
- 21:             **continue**
- 22:           **if**  $dist_{\text{prev}} > D[i, j, p]$  **then** ▷  $D[i, j, p]$  stores the best so far.
- 23:             **continue**
- 24:           **if**  $L^C = L_{\text{min}}^C$  **then** ▷ Compute the lower bound from sketch.
- 25:              $lb = (c'_1 - q'_1)^2$  ▷ Partial distance contributed by the first alignment.
- 26:             **for**  $k \leftarrow 2$  **to**  $L^C$  **do**
- 27:                $lb = lb + \delta(c'_k, \tilde{\mathbf{q}}_k)$
- 28:           **else**
- 29:              $lb = lb + \delta(c'_{L^C}, \tilde{\mathbf{q}}_{L^C})$  ▷ Compute the lower bound incrementally.
- 30:              $lb_{\text{check}} = lb - \delta(c'_{L^C}, \tilde{\mathbf{q}}_{L^C}) + (c'_{-1} - q'_{-1})^2$  ▷ Tighten the lower bound by using the last alignment.
- 31:           **if**  $dist_{\text{prev}} + lb_{\text{check}} > D[i, j, p]$  **then**
- 32:             **continue**
- 33:            $dist_{\text{seg}} \leftarrow \text{DTW}_r(Q'^L, C'^L)$
- 34:           **if**  $dist_{\text{prev}} + dist_{\text{seg}} < D[i, j, p]$  **then**
- 35:              $D[i, j, p] \leftarrow dist_{\text{prev}} + dist_{\text{seg}}$  ▷ Also save pointer  $(i', j')$  for the cut.
- 36: **return**  $D[m, n, P]$

---

1556 set the maximum segment length be the alignment factor  $L$  in line 3. We set the base  
 1557 case in line 5.

1558 We fill the table  $D$  in Algorithm 4. In line 3, given  $p$  pieces in  $Q$ , the ending index  
 1559 of the last piece (i.e., the  $p^{\text{th}}$  piece) will range from  $(p \cdot L_{\text{gmin}}^Q)$ , given all the  $p$  pieces are  
 1560 in minimum length  $L_{\text{gmin}}^Q$ , to  $\min(p \cdot L_{\text{gmax}}^Q, m)$ , given all the  $p$  pieces are in maximum  
 1561 length  $L_{\text{gmax}}^Q$ .

1562 In line 4, we enumerate for all the allowed lengths  $L^Q$ . For the segment with length  
 1563  $L^Q$  in  $Q$ , the length  $L^C$  of the corresponding aligned segment in  $C$  will have a range from

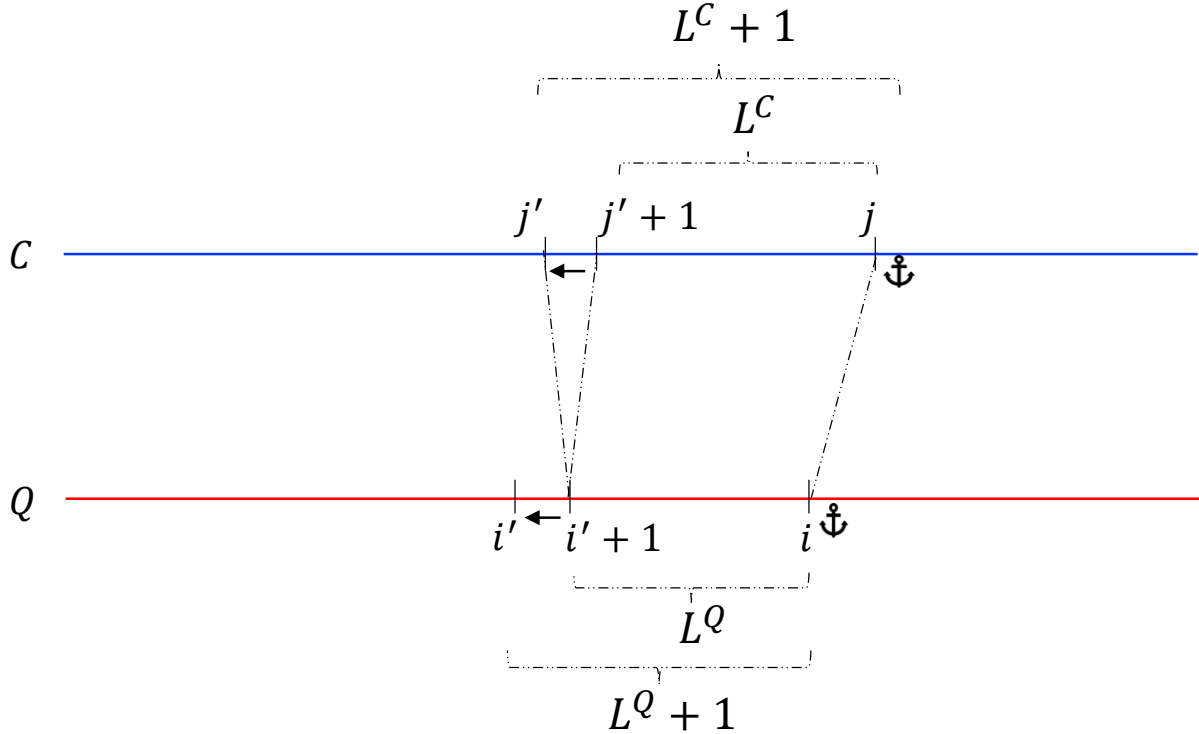


Figure 4.7: Relationship of  $L_Q$  and  $L_C$ .

$L_{\min}^C$  to  $L_{\max}^C$ , as defined in lines 7–8, such that the ratio of  $L^Q$  and  $L^C$  would be bounded by  $l$ . Because  $L^Q$  and  $L^C$  increase in line 4 and line 14, and the  $i$  and  $j$  are fixed by the outer loop, in line 3 and line 13, respectively, the  $i'$  and  $j'$  decrease correspondingly. It is visualized in Figure 4.7. A segment in  $Q$  with ending index  $i$  and starting index  $i' + 1$  would be compared to a set of segments in  $C$ , all of which have a fixed end at  $j$  and a decreasing starting index, starting at  $j' + 1$ . For example, the starting index of the first segment with being compared is  $j' + 1$ , which has length  $L^C$ , and that of the second segment is  $j'$ , which has length  $L^C + 1$ , as in Figure 4.7.

In line 18, we terminate the current iteration if there are no previously valid segment pairs (i.e.,  $dist_{\text{prev}} = \infty$ ).

In line 22, if the accumulated cost  $dist_{\text{prev}}$  exceeds the current best so far, we stop the current iteration as the resulting ( $dist_{\text{prev}} + dist_{\text{seg}}$ ) is guaranteed to be greater than the current best so far, which is stored in  $D[i, j, p]$ .

To be consistent with the result of using the lower bound speedup technique, which will be introduced later, we compute the DTW in the reverse manner in line 33. Due to the nearest neighbor interpolation,  $\text{DTW}_r(Q'^L, C'^L)$  may not equal to  $\text{DTW}_r(\text{rev}(Q')^L, \text{rev}(C')^L)$ .

In line 35, we also save the pairs  $(i', j')$  that serve as cutting points between segments to obtain the segmentation result.

**Parallel computing:** We observe that the recurrence relation for the state  $D[i, j, p]$  at stage  $p$  depends exclusively on the states computed at stage  $p - 1$ , as shown in Equa-

1584 tion 4.15. There are no stage dependencies over indices  $i$  and  $j$ . It allows us to parallelize  
 1585 the loops over indices  $i$  and  $j$  on lines 3 and 13. In the following experimental section, we  
 1586 distribute the i-loop iterations (i.e., line 3 in Algorithm 4, which is colored in blue) across  
 1587 available threads only because there are already sufficient iterations from the i-loop to  
 1588 fill the available threads. There are  $\left(\min(p \cdot L_{\text{gmax}}^Q, m) - (p \cdot L_{\text{gmin}}^Q) + 1\right)$  iterations from  
 1589 the i-loop. The parallel execution of the  $i$ -loop is implemented by `prange` in Numba in  
 1590 Python.

1591 **Early Abandoning in nearest neighbor search:** To accelerate the nearest neighbor  
 1592 search (or top- $k$  search) for a query  $Q$  on a candidate set, we employ an early abandoning  
 1593 strategy. It prunes the search branch within the PSD computation of a specific candidate  
 1594  $C$  as soon as the result corresponding to this search branch is determined to be sub-  
 1595 optimal. We maintain a variable,  $\text{bsf}$  (best-so-far), which represents the minimum final  
 1596 distance among the candidates processed with  $Q$  so far.  $\text{bsf}$  serves as an upper-bound  
 1597 threshold. During the evaluation of a new candidate  $C$ , we monitor the accumulated  
 1598 partial distance,  $\text{dist}_{\text{prev}}$ . If  $\text{dist}_{\text{prev}}$  exceeds  $\text{bsf}$ , the corresponding final distance is guar-  
 1599 anteed to exceed  $\text{bsf}$ . In such cases, the current search branch is immediately terminated.  
 1600 The implementation of this pruning mechanism is detailed in lines 20–21 in Algorithm 4,  
 1601 which are colored in orange. In the case of top- $k$  search, we must maintain the top- $k$   
 1602 final distances and use the  $k$ -th distance as the threshold.

### 1603 Lower bound:

1604 When we use DTW as a routine in PSD, the computation of the DTW of the interpo-  
 1605 lated segment can be sped up by computing  $\text{LB}_{\text{Shen}}$  for the lower bound. From Figure 4.7,  
 1606 we observe that a segment of  $Q$ , with length  $L^Q$ , is compared to a set of growing seg-  
 1607 ments of  $C$ , with a fixed end at  $j$ . The length of these segments is from  $L_{\text{min}}^C$  to  $L_{\text{max}}^C$ ,  
 1608 as indicated in line 14 in Algorithm 4. They share the same suffix with length  $L_{\text{min}}^C$ . It  
 1609 encourages us to view both  $Q$  and  $C$  reversely. The reversed segments are denoted as  $Q'$   
 1610 and  $C'$ , as in lines 6 and 16 in Algorithm 4. In this reversed view, they share the same  
 1611 prefix with length  $L_{\text{min}}^C$ . Hence, we construct an indexed collection  $\tilde{\mathbb{Q}}$  for  $Q'$  with the  
 1612 maximum length of the segments being compared in  $C$ , which is  $L_{\text{max}}^C$ , as in lines 10–12.

1613 In lines 24–27, we first compute the lower bound between  $Q'$  and the shortest segment  
 1614 of  $C$ . We add the minimum possible contribution of each  $c'$  to the distance contributed  
 1615 by the first alignment, which is  $lb = (c'_1 - q'_1)$ . For the lower bound of the subsequent  
 1616 segments, we compute them incrementally in line 29. Because the last point of segment  
 1617  $C'$  must map to the last point of  $Q'$ , we further tighten the lower bound by using the last  
 1618 alignment in line 30 instead.

1619 Furthermore, we can reduce the computational overhead of constructing the sorted  
 1620 reaches  $\tilde{\mathbb{q}}_k$  (lines 9–12). As illustrated in Figure 4.7, the segment of  $Q$  involved in the  
 1621 comparison grows incrementally. Since the reversed versions of these segments share a  
 1622 common prefix, the sorted reaches  $\tilde{\mathbb{q}}_k$  computed for a segment  $Q'$  of length  $L^Q$  can be

---

**Algorithm 5** Replace lines 3 to 9 in Algorithm 5 to reuse the computed sorted reaches  $\tilde{q}_k$ .

---

```

1:  $r'_{\text{cache}} \leftarrow -1$ 
2: for  $i \leftarrow (p \cdot L_{\text{gmin}}^Q)$  to  $\min(p \cdot L_{\text{gmax}}^Q, m)$  do
3:   for  $L^Q \leftarrow L_{\text{gmin}}^Q$  to  $L_{\text{gmax}}^Q$  do
4:      $i' \leftarrow i - L^Q$ 
5:      $Q' \leftarrow \text{rev}(Q(i' + 1 : i))$ 
6:      $L_{\text{min}}^C \leftarrow \max(L_{\text{gmin}}^C, \lceil L^Q/l \rceil)$ 
7:      $L_{\text{max}}^C \leftarrow \min(\lfloor L^Q/l \rfloor, L_{\text{gmax}}^C)$ 
8:      $r' \leftarrow r \times \max(L^Q, L_{\text{max}}^C)$ 
9:     if  $r'_{\text{cache}} = r'$  then
10:      for  $k \leftarrow 1$  to  $L_{\text{max}}^C$  do
11:        if  $k \leq |Q'|$  then
12:           $e_{\text{prev}} \leftarrow \min(\lfloor kl \rfloor + r', L^Q - 1)$ 
13:           $e_{\text{new}} \leftarrow \min(\lfloor kl \rfloor + r', L^Q)$ 
14:          if  $e_{\text{new}} > e_{\text{prev}}$  then
15:             $\tilde{q}_k \leftarrow \tilde{q}_k \cup q'_{e_{\text{new}}}$ 
16:        else
17:           $q_k \leftarrow (q'_{\max(1, \lceil k/l \rceil - r')}, \dots,$ 
18:           $q'_{\min(\lfloor kl \rfloor + r', L^Q)})$   $\triangleright L^Q$  equals to  $|Q'|$ .
19:        else
20:          for  $k \leftarrow 1$  to  $L_{\text{max}}^C$  do
21:             $q_k \leftarrow (q'_{\max(1, \lceil k/l \rceil - r')}, \dots,$ 
22:             $q'_{\min(\lfloor kl \rfloor + r', L^Q)})$ 
23:             $\tilde{q}_k \leftarrow \text{sort}(\tilde{q}_k)$ 
 $r_{\text{cache}} \leftarrow r'$ 

```

---

reused to compute those for the subsequent segments. This optimization is detailed in 1623  
Algorithm 5, with the new components highlighted in blue. It is important to note that 1624  
because  $r'$  is a function of  $L^Q$ , and the construction of  $\tilde{q}_k$  depends on  $r$ , reuse is limited 1625  
to cases where  $r'$  remains constant. We construct reaches  $\tilde{q}_k$  from the sketch in lines 1626  
20–22 and keep track of the  $r'$  used for construction in line 23. If  $r'$  remains constant, 1627  
we can use previously computed reaches  $\tilde{q}_k$  to compute the new set of reaches  $\tilde{q}_k$ . Since 1628  
the ending index of reaches depends on  $\min(\lfloor kl \rfloor + r', L^Q)$ , we need to check whether we 1629  
have a new ending index when  $L^Q$  increases. If the ending index has been changed, we 1630  
need to add the new data points  $q'_{e_{\text{new}}}$  to the sorted sequence  $\tilde{q}_k$ , as in line 15. 1631

$L_{\text{max}}^C$  depends of  $L^Q$ . If  $L_{\text{max}}^C$  increase because  $L^Q$  increase, we construct the new reach 1632  
 $\tilde{q}_k$  and sort it in lines 16–18. 1633

### 1634 4.4.3 Guided Distance

1635 For faster computation, one would want to use a distance measure with linear complexity,  
1636 such as ED, as the base measure for PSD. While PSED is effective for identifying phase-  
1637 scaling changes, certain applications require capturing complex properties within those  
1638 segments that ED cannot handle. There are two ways to address it. One approach is  
1639 to use an alternative distance measure that captures these complex properties as the  
1640 base distance for computing the PSD, such as DTW. But PSDTW is slower than PSED.  
1641 The other approach is to use the segmentation result returned by PSED. To address  
1642 this, we propose a two-stage framework in which PSED-derived segmentation guides the  
1643 application of advanced distance metrics  $M$ . Let  $\mathcal{P}^* = \{(i_1, j_1), (i_2, j_2), \dots, (i_{P+1}, j_{P+1})\}$   
1644 be the set of optimal cut points on  $Q$  and  $C$  obtained by minimizing the PSED. We  
1645 utilize  $\mathcal{P}^*$  to partition both series into  $P$  aligned pairs of segments. The final distance,  
1646 denoted as  $M^{\text{PSED}}$ , is calculated by summing the distances of these pairs using a target  
1647 metric  $M$ :

$$M^{\text{PSED}}(Q, C) = \sum_{p=1}^P M(Q_p^L, C_p^L) \quad (4.16)$$

1648 , where  $Q_p = Q(i_p + 1 : i_{p+1})$  and  $C_p = C(j_p + 1 : j_{p+1})$ .

## 1649 4.5 Experiments

1650 We evaluate the performance of our proposed distance measure framework, PSD, via its  
1651 two instantiations: PSED and PSDTW. Specifically, we focus on a query retrieval task  
1652 in which the query exhibits piecewise-scaled distortion, that is, distinct phases of the  
1653 query exhibit different expression rates relative to the target in the candidate dataset.  
1654 Our objective is to verify whether PSD achieves invariance to these multiple scaling  
1655 distortions, thereby allowing it to correctly retrieve the most similar candidate. We detail  
1656 the experimental setup in Section 4.5.1 and present the results in Section 4.5.2. The code  
1657 and data are available at <https://github.com/colemanyu/k-scaling-factor-dtw>.

### 1658 4.5.1 Experimental Setup

1659 We utilize the GunPoint dataset, originally released in 2003 [71], as the running example.  
1660 Widely regarded as the “iris” dataset of the time series community [22], it has appeared  
1661 in over one thousand publications. Beyond its ubiquity, the dataset addresses a critical  
1662 distinction: misinterpreting the act of aiming a gun as merely pointing a finger could  
1663 have life-threatening consequences.

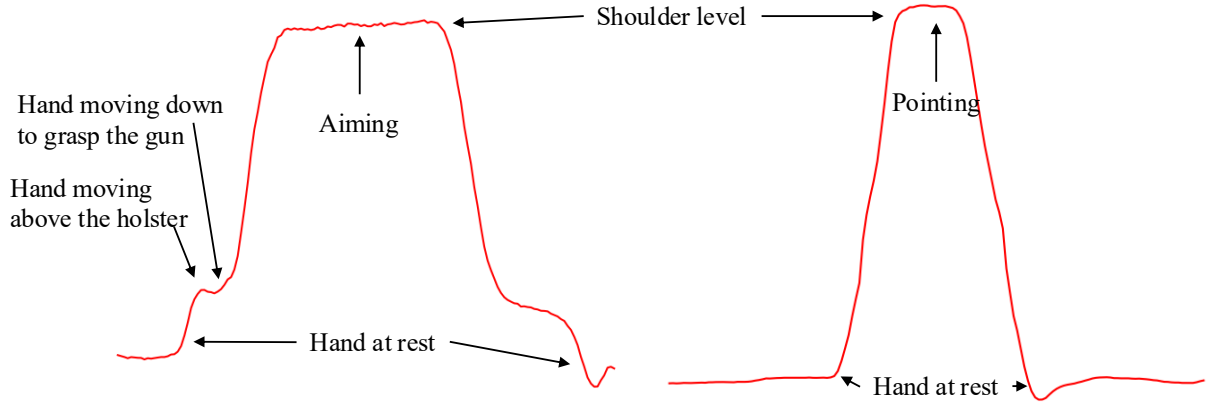


Figure 4.8: Visualization of the GunPoint dataset. Left (Right): A time series of the “Gun” (“Point”) scenario. Critical periods, such as “Aiming”, are annotated.

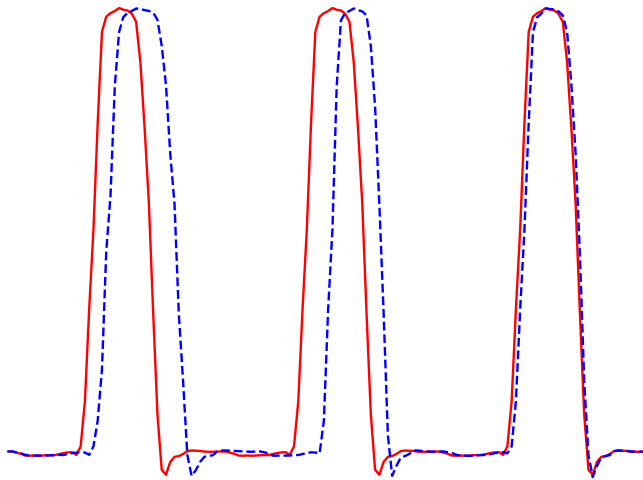


Figure 4.9: The red solid time series shows an instant in the target set. The blue dashed time series shows an instant in the query set.

The dataset contains two classes: “Gun” and Point”. Actors aim at an eye-level target 1664 using either a replica gun or their index finger, as illustrated in Figure 4.8. The resulting 1665 time series represent the X-axis centroid of the actor’s right hand. Each action lasts 1666 for 5 seconds, with the pointing/aiming phase occurring for approximately one second. 1667 Recorded at 30 fps, each sample consists of 150 data points. The dataset comprises 50 1668 training and 150 test series, all of length 150. 1669

A key limitation of the original dataset is the assumption that every action lasts 1670 exactly 5 seconds. In reality, actors perform actions at varying speeds. If an actor is 1671 asked to perform the action three times continuously in a row, we are likely to observe a 1672 time series containing three phases, each with a unique rate. The first phase should take 1673 longer than subsequent phases because it is the first time the action is performed. This 1674 phenomenon is depicted in Figure 4.9, where the red curve represents an ideal case that 1675 consists of three identical phases (i.e., identical rate), while the blue curve represents a 1676

1677 realistic scenario with varying rates. The first action is slower than the second action.  
1678 Consequently, retrieving such patterns requires assigning different scaling factors to each  
1679 phase to accommodate the phase-specific rates.

1680 We now describe the procedure for generating the target and query sets for the re-  
1681 trieval task. To construct the target set, we concatenate  $P$  repetitions of each time series  
1682 instance from the source dataset. To ensure a fair comparison, we constrain the resulting  
1683 time series to match the original length  $n$ . This is achieved by rescaling each phase to a  
1684 length of  $n/P$  prior to concatenation. Note that we must handle remainders to ensure  
1685 that the final time series length is exactly  $n$ . An example of such a target (where  $P = 3$ )  
1686 is depicted by the red solid line in Figure 4.9.

1687 To construct the query set, we first determine the specific lengths for the  $P$  segments.  
1688 Starting with an expected mean length of  $n/P$ , we define the minimum segment length  
1689 as  $L_{\min} = (n/P)\sqrt{l}$  and the maximum as  $L_{\max} = (n/P)\sqrt{l}$ . This formulation ensures  
1690 that the ratio of the lengths of any two segments is bounded by  $l$ . We then generate  $P$   
1691 random integers within  $[L_{\min}, L_{\max}]$  subject to the constraint that their sum is exactly  $n$ .  
1692 Finally, we construct the query by rescaling  $P$  copies of the source time series to these  
1693 generated random lengths and concatenating them. The resulting time series maintains  
1694 the original length  $n$ . An example of such a query (where  $P = 3$ ) is depicted by the blue  
1695 dashed line in Figure 4.9.

1696 Both the query and target sets are derived from the same source dataset. Conse-  
1697 quently, the ground truth target for a given query is defined as the instance in the target  
1698 set that is generated from the same underlying source time series.

Table 4.1: Details of the ten datasets for the experiments

Name	Type	Train/Test?	Size	Class	Length
SonyAIBORobotSurface1	Sensor	Test	601	2	70
ECG200	ECG	Train	100	2	96
MedicalImages	Image	Train	381	10	99
CBF	Simulated	Train	30	3	128
SwedishLeaf	HAR	Train	500	15	128
Plane	Sensor	Train	105	7	144
PowerCons	Device	Train	180	2	144
GunPoint	HAR	Train	50	2	150
Adiac	Image	Train	390	37	176
Epilepsy	HAR	Train	137	4	207

1699 Table 4.1 details the additional datasets used in this study. The column labeled  
1700 “Train/Test?” specifies which split was employed as the source dataset.

1701 In our experiments, we set the warping window parameter  $r = 0.1$ , as suggested in  
1702 the literature. The algorithms were implemented in Python. We utilized the `aeon` [63]

library to obtain the baseline distance measures. All experiments were conducted on a 1703  
workstation equipped with an Intel Xeon Gold 6326 CPU and 256GB of RAM. 1704

## 4.5.2 Experimental Results

1705

We employ Top- $k$  Accuracy (often referred to as Precision@ $k$  [86]) as the primary evaluation metric. For a single query  $Q$ , this metric indicates whether the correct match is successfully retrieved within the top  $k$  candidates: 1706  
1707  
1708

$$P@k(Q) = \begin{cases} 1 & \text{if the ground truth is in the top-}k \text{ results} \\ 0 & \text{otherwise} \end{cases} \quad (4.17)$$

To determine the top- $k$  results, we compute the distance between  $Q$  and every time series in the target set, generating a distance profile of length equal to the dataset size. 1709  
1710  
1711  
1712  
1713  
The top- $k$  results correspond to the  $k$  instances with the smallest distances in this profile. Finally, we evaluate the overall performance by computing the mean Top- $k$  Accuracy across the entire query set  $\mathcal{D}$ : 1712

$$\overline{P@k} = \frac{\sum_{Q \in \mathcal{D}} P@k(Q)}{|\mathcal{D}|} \quad (4.18)$$

We choose  $k \in \{1, 3\}$ .  $k = 1$  refers to the exact retrieval.  $k = 3$  give some tolerance for the retrieval. 1714  
1715

Table 4.2: The accuracy comparison for eight distance measures of the GunPoint dataset

$P$	$l$	ED		DTW [74]		ADTW [37]		DDTW [45]		shapeDTW [100]		WDDTW [40]		WDTW [40]		PSED		PSDTW	
		$\overline{P@1}$	$\overline{P@3}$																
2	1.25	0.30	0.56	0.82	1.00	0.54	0.84	0.84	0.92	<u>0.96</u>	1.00	0.88	0.96	0.82	0.98	<b>0.98</b>	1.00	0.86	1.00
	1.50	0.14	0.36	0.88	1.00	0.38	0.64	0.78	0.94	<b>1.00</b>	1.00	0.80	0.92	0.88	0.96	<b>1.00</b>	1.00	<u>0.96</u>	1.00
	1.75	0.16	0.34	0.82	1.00	0.38	0.66	0.64	0.80	0.90	1.00	0.66	0.80	0.82	0.96	<b>1.00</b>	1.00	<u>0.94</u>	1.00
	2.00	0.12	0.24	0.84	0.98	0.34	0.66	0.72	0.88	<u>0.96</u>	1.00	0.68	0.86	0.82	0.98	<b>1.00</b>	1.00	<u>0.96</u>	1.00
3	1.25	0.30	0.50	0.84	0.92	0.70	0.88	0.80	0.92	<b>0.96</b>	0.98	0.84	0.94	0.86	0.98	<u>0.94</u>	1.00	0.88	0.96
	1.50	0.10	0.28	0.84	0.96	0.60	0.78	0.66	0.86	<u>0.90</u>	1.00	0.72	0.86	0.84	0.98	<b>0.96</b>	1.00	0.86	0.96
	1.75	0.10	0.28	<u>0.88</u>	1.00	0.42	0.78	0.72	0.88	0.76	0.94	0.74	0.88	<u>0.88</u>	1.00	<b>1.00</b>	1.00	<u>0.88</u>	0.98
	2.00	0.02	0.12	<u>0.86</u>	0.94	0.38	0.52	0.60	0.78	0.70	0.94	0.60	0.80	0.82	0.92	<b>0.98</b>	1.00	<u>0.86</u>	0.98
4	1.25	0.34	0.50	0.70	0.86	0.68	0.88	0.60	0.78	0.70	0.90	0.64	0.80	0.70	0.86	<b>0.86</b>	0.94	<u>0.72</u>	0.88
	1.50	0.22	0.38	0.64	0.80	0.60	0.92	0.52	0.64	0.68	0.90	0.52	0.66	0.64	0.82	<b>0.86</b>	0.98	<u>0.72</u>	0.82
	1.75	0.16	0.30	0.72	0.92	0.56	0.80	0.60	0.78	0.56	0.80	0.56	0.80	0.70	0.88	<b>0.92</b>	1.00	<u>0.80</u>	0.94
	2.00	0.06	0.12	0.58	0.78	0.50	0.72	0.46	0.64	0.50	0.82	0.50	0.64	0.56	0.82	<b>0.88</b>	0.98	<u>0.64</u>	0.88

**Results of GunPoint dataset:** We utilize the GunPoint dataset to evaluate how the parameters  $P$  and  $l$  affect the ability of PSD to achieve invariance under piecewise scaling. 1716  
1717  
1718  
1719  
1720  
1721  
1722  
The results are presented in Table 4.2, where the best performance of  $\overline{P@1}$  is highlighted in bold, and the second-best is underlined. We benchmark our method against several state-of-the-art distance measures, including ADTW [37], DDTW [45], shapeDTW [100], WDDTW [40], and WDTW [40]. PSED achieves the highest accuracy, followed closely by PSDTW. We attribute PSED’s superior performance over PSDTW to the specific nature

of the distortions in the query set, that is, the “pure” piecewise scaling distortions. Since  
 the query set exhibits only piecewise scaling distortions, the corresponding segments of the  
 query and target time series differ solely in length (scale). Consequently, the additional  
 flexibility provided by DTW in PSDTW is unnecessary and may inadvertently increase  
 the similarity of incorrect matches, thereby reducing discriminative power relative to the  
 stricter PSED measure. However, PSDTW remains theoretically essential for handling  
 local distortions within the phase. PSDTW applies DTW within the scaled segment,  
 enabling robust alignment across local nonlinearities.

Table 4.3: The accuracy comparison for six PSED-guided distance measures of the Gun-Point dataset

$P$	$l$	DTW <sup>PSED</sup>		ADTW <sup>PSED</sup>		DDTW <sup>PSED</sup>		shapeDTW <sup>PSED</sup>		WDDTW <sup>PSED</sup>		WDTW <sup>PSED</sup>	
		$\overline{P@1}$	$\overline{P@3}$	$\overline{P@1}$	$\overline{P@3}$	$\overline{P@1}$	$\overline{P@3}$	$\overline{P@1}$	$\overline{P@3}$	$\overline{P@1}$	$\overline{P@3}$	$\overline{P@1}$	$\overline{P@3}$
2	1.25	0.86	1.00	0.98	1.00	<b>0.72</b>	0.92	0.98	1.00	<b>0.74</b>	0.96	0.86	1.00
	1.50	0.88	1.00	1.00	1.00	<b>0.60</b>	0.90	<b>0.98</b>	1.00	<b>0.64</b>	0.90	0.92	1.00
	1.75	0.94	1.00	1.00	1.00	0.84	0.94	1.00	1.00	0.86	0.96	0.94	1.00
	2.00	0.98	1.00	1.00	1.00	<b>0.60</b>	0.78	0.98	1.00	<b>0.66</b>	0.80	0.98	1.00
3	1.25	<b>0.82</b>	0.96	0.94	1.00	<b>0.74</b>	0.90	<b>0.92</b>	0.98	<b>0.76</b>	0.90	<b>0.82</b>	0.96
	1.50	0.86	1.00	0.96	1.00	0.72	0.90	0.94	1.00	0.80	0.90	0.88	1.00
	1.75	0.88	1.00	1.00	1.00	<b>0.68</b>	0.90	1.00	1.00	<b>0.70</b>	0.94	0.90	1.00
	2.00	0.86	0.96	0.98	1.00	<b>0.54</b>	0.86	0.96	1.00	0.62	0.86	0.88	0.96
4	1.25	0.74	0.88	0.86	0.94	0.78	0.80	0.80	0.92	0.78	0.82	0.74	0.88
	1.50	0.72	0.84	0.86	0.98	0.68	0.84	0.84	0.96	0.66	0.84	0.72	0.86
	1.75	0.74	0.96	0.92	1.00	<b>0.54</b>	0.90	0.90	1.00	0.56	0.88	0.74	0.96
	2.00	0.66	0.90	0.88	0.98	0.58	0.82	0.88	0.98	0.62	0.80	0.66	0.90

We further investigate whether the segmentation results returned by PSED can serve  
 as a guide to enhance other distance measures. As shown in Table 4.3, this approach  
 generally improves accuracy. The exceptions are highlighted in bold, indicating cases  
 where the segmentation led to worse performance. Notably, in most cases, only DDTW  
 and WDDTW failed to benefit from PSED-guided segmentation. We argue that the  
 performance degradation of DDTW and WDDTW stems from their derivative-based  
 nature. They rely on matching slope or shape features. Consequently, they are highly  
 sensitive to segmentation boundaries. A non-perfect cut that falls within a shape feature  
 segmentizes it, and these features are then destroyed. When the algorithm subsequently  
 attempts to map these features, it fails to find correct correspondences, resulting in high  
 distances.

Figure 4.10 illustrates the runtime performance across varying parameters  $P$  and  $l$ .  
 We evaluate two variants of PSD, PSED and PSDTW, each implemented with three  
 levels of

- 1745 1. `vanilla` (i.e., Basic implementation)
- 1746 2. `parallel_bsf` (i.e., With parallelization with Best-So-Far early abandoning)

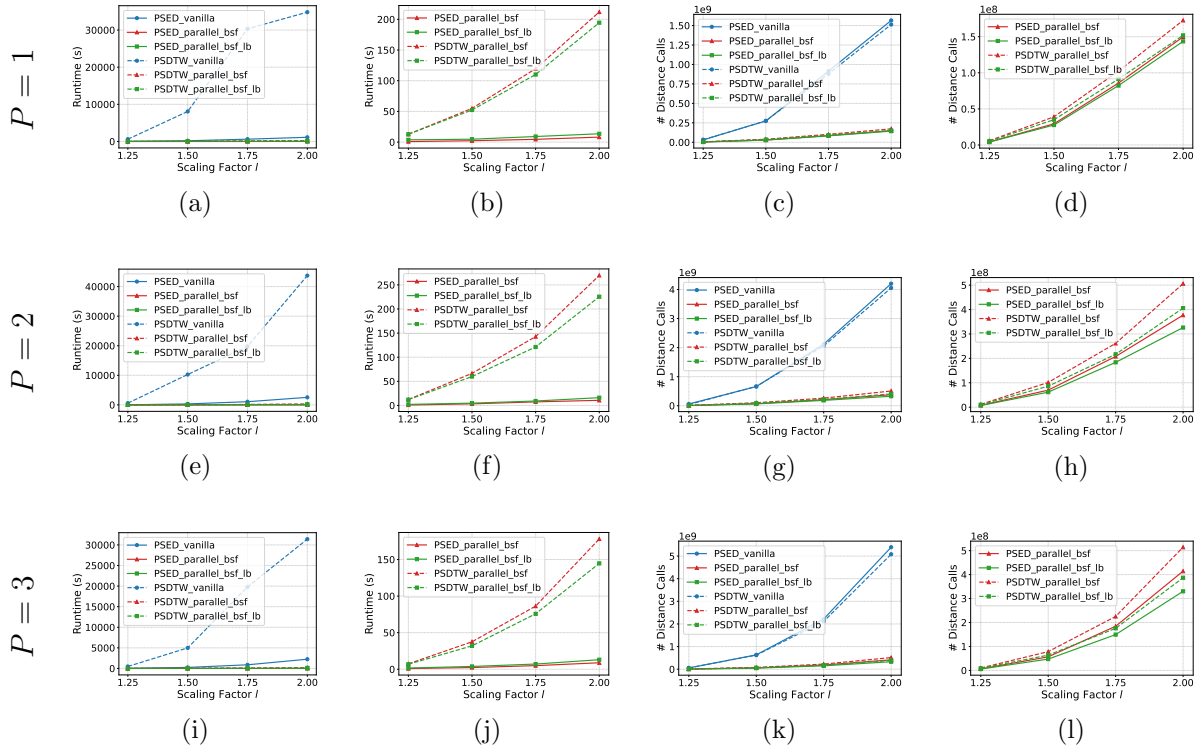


Figure 4.10: Runtime and number of distance calls comparison of GunPoint dataset. (a)-(d)  $P = 1$ , (e)-(h)  $P = 2$ , (i)-(l)  $P = 3$ .

### 3. parallel\_bsf\_lb (i.e., Incorporating lower bound pruning)

1747

This yields a total of six methods. The figure is organized into four columns plotted against the scaling factor  $l$ . The rows refer to the number of pieces  $P$ . The first and third columns display the running time and the number of distance calculations, respectively, for all six methods. To better visualize the performance differences among the efficient implementations, the second and fourth columns omit the `vanilla` baselines and focus exclusively on the four optimized variants. 1748  
1749  
1750  
1751  
1752  
1753

The results indicate that `vanilla_PSDTW` is orders of magnitude slower than the other approaches, whereas the optimized methods operate within a similar performance range. 1754  
1755  
As anticipated, the computation time for all methods increases with the scaling factor 1756  
 $l$ . The fourth column confirms that the lower bounding strategy effectively reduces the 1757  
number of distance calculations (pruning power). However, the second column reveals 1758  
a critical trade-off in actual runtime. While the lower bound successfully accelerates 1759  
PSDTW, it actually slows down PSED. This suggests that for the computationally lighter 1760  
ED, the overhead of calculating the lower bound outweighs the time saved by pruning. 1761  
Overall, the results demonstrate that PSED is significantly faster than PSDTW. 1762

### Results of the ten datasets:

For the remaining nine datasets, we fix the parameters at  $P = 3$  and  $l = 1.5$ . We 1764  
have the following findings from the previous experiment: 1765

Table 4.4: The accuracy comparison for eight distance measures of the ten datasets

Dataset	ED		DTW		ADTW		DDTW		shapeDTW		WDDTW		WDTW		PSED	
	P@1	P@3	P@1	P@3	P@1	P@3	P@1	P@3	P@1	P@3	P@1	P@3	P@1	P@3	P@1	P@3
SonyAIBORobotSurface1	0.04	0.08	0.51	0.63	<u>0.60</u>	0.74	0.45	0.57	0.20	0.29	0.45	0.58	0.51	0.64	<b>0.67</b>	0.77
ECG200	0.12	0.20	0.70	0.81	<u>0.78</u>	0.83	0.60	0.74	0.59	0.76	0.59	0.73	0.70	0.80	<b>0.81</b>	0.88
MedicalImages	0.08	0.19	0.63	0.78	0.69	0.85	0.52	0.68	0.57	0.75	0.51	0.68	0.62	0.78	<b>0.76</b>	0.88
CBF	0.53	0.67	0.83	1.00	<u>0.90</u>	1.00	0.73	0.87	0.73	0.90	0.77	0.90	<u>0.90</u>	1.00	<b>1.00</b>	1.00
SwedishLeaf	0.07	0.12	0.82	0.92	<u>0.84</u>	0.93	0.70	0.83	0.78	0.91	0.69	0.83	0.83	0.92	<b>0.97</b>	0.99
Plane	0.09	0.14	0.50	0.74	<u>0.59</u>	0.78	0.38	0.64	0.53	0.79	0.37	0.61	0.49	0.75	<b>0.75</b>	0.93
PowerCons	0.26	0.43	0.77	0.98	<b>0.80</b>	1.00	0.77	0.98	0.77	0.99	0.77	0.99	0.77	0.99	<b>0.80</b>	1.00
GunPoint	0.10	0.28	<u>0.84</u>	0.96	0.60	0.78	0.66	0.86	0.90	1.00	0.72	0.86	<u>0.84</u>	0.98	<b>0.96</b>	1.00
Adiac	0.01	0.02	<u>0.37</u>	0.50	0.12	0.21	0.32	0.42	0.27	0.41	0.31	0.41	0.36	0.50	<b>0.57</b>	0.71
Epilepsy	0.18	0.26	0.74	0.88	<u>0.80</u>	0.91	0.65	0.82	0.38	0.47	0.58	0.79	0.70	0.83	<b>0.83</b>	0.91

Table 4.5: The accuracy comparison for six PSED-guided distance measures of the ten datasets

Dataset	DTW <sup>PSED</sup>		ADTW <sup>PSED</sup>		DDTW <sup>PSED</sup>		shapeDTW <sup>PSED</sup>		WDDTW <sup>PSED</sup>		WDTW <sup>PSED</sup>	
	P@1	P@3	P@1	P@3	P@1	P@3	P@1	P@3	P@1	P@3	P@1	P@3
SonyAIBORobotSurface1	0.53	0.64	0.64	0.76	<b>0.37</b>	0.53	0.65	0.76	<b>0.38</b>	0.53	0.53	0.65
ECG200	0.73	0.84	0.80	0.88	<b>0.54</b>	0.68	0.81	0.88	<b>0.53</b>	0.69	0.73	0.84
MedicalImages	0.66	0.78	0.76	0.88	0.51	0.69	0.74	0.88	0.51	0.70	0.66	0.79
CBF	0.90	1.00	0.93	1.00	0.73	0.93	0.93	0.97	<b>0.70</b>	0.93	0.90	1.00
SwedishLeaf	0.82	0.92	0.97	0.99	0.72	0.87	0.97	0.99	0.73	0.88	<b>0.82</b>	0.92
Plane	0.60	0.80	0.75	0.94	0.50	0.67	0.74	0.90	0.50	0.69	0.59	0.80
GunPoint	0.86	1.00	0.96	1.00	0.72	0.90	0.94	1.00	0.80	0.90	0.88	1.00
PowerCons	0.78	0.99	0.79	1.00	0.79	1.00	0.79	1.00	0.79	1.00	0.78	1.00
Adiac	<b>0.33</b>	0.45	0.57	0.71	<b>0.21</b>	0.34	0.53	0.70	<b>0.20</b>	0.33	<b>0.34</b>	0.45
Epilepsy	0.77	0.88	<b>0.78</b>	0.88	0.66	0.79	0.74	0.89	0.66	0.82	0.80	0.89

1766 1. From Table 4.3, PSED outperformed PSDTW in handling piecewise scaling distortions.

1767 2. From Figure 4.10, the lower bound offered no efficiency gain for PSED.

1769 Hence, we select PSED\_parallel\_bsfs as the representative method for this evaluation.

1770 The accuracy results are presented in Table 4.4, while the results for the PSED-guided  
1771 distance measures are detailed in Table 4.5. Finally, the runtime efficiency for all datasets  
1772 is summarized in Table 4.6. It shows a significant speedup, ranging from 10.10X to  
1773 191.46X.

## 1774 4.6 Concluding Remarks

1775 In this paper, we proposed a novel distance measure framework, Piecewise Scaling Dis-  
1776 tance (PSD), which relaxes the strict assumption of a single uniform scaling factor across  
1777 the entire time series. We presented an exact dynamic programming (DP) algorithm to  
1778 solve this problem. To enhance efficiency and prevent pathological segment alignments,  
1779 we introduced a constraint version, which limits the search space of segment lengths  
1780 based on given scaling factors. To enhance computational efficiency, we integrated two

Table 4.6: The number of distance calls and runtime on PSED\_vanilla and PSED\_parallel\_bsf of the ten datasets

Name	Size	Length	PSED_vanilla	PSED_parallel_bsf	% distance calls pruned	Speed Up
			Time (s)	Time (s)		
SonyAIBORobotSurface1	601	70	697	69	90.40%	10.10X
ECG200	100	96	91	3	91.08%	30.33X
MedicalImages	381	99	2082	40	96.03%	52.05X
CBF	30	128	43	2	75.31%	21.50X
SwedishLeaf	500	128	16601	107	96.24%	155.15X
Plane	105	144	621	6	96.05%	103.50X
PowerCons	180	144	3629	49	82.32%	74.06X
GunPoint	50	150	159	3	89.42%	53.00X
Adiac	390	175	23550	123	96.71%	191.46X
Epilepsy	137	206	13131	336	39.88%	39.08X

optimization techniques for the general PSD framework. In addition, we propose incorporating a lower-bounding strategy to accelerate PSDTW. Our experimental results demonstrate the necessity and effectiveness of PSD when identifying matches between a query  $Q$  and a candidate  $C$  under piecewise scaling distortions.

We outline several directions for future research. First, we aim to develop a lower bound specifically optimized for PSED that can improve actual runtime. Second, while the current PSDTW algorithm requires the number of segments  $P$  to be specified as a hyperparameter, it is preferable for the algorithm to determine this value adaptively. A simple heuristic is to test a range of  $P$  values and select the configuration that yields the minimum distance. Finally, we plan to investigate efficiency improvements for PSDTW. Currently, PSDTW computes dynamic time warping on two growing subsequences after scaling. While techniques for Incremental DTW [51] allow for the reuse of the accumulating cost matrix  $D$  to avoid redundant calculations, applying this to PSDTW is non-trivial. The interpolation performed before DTW fundamentally alters the sequence structure, preventing the straightforward extension of  $D$  (e.g., by appending rows or columns) to reuse the computed  $D$  that is possible in standard DTW.



# Chapter 5

1797

## Leveraging Nearest Neighbors for Time Series Forecasting with Matrix Profile

1798

1799

1800

### 5.1 Introduction

1801

Humans have made predictions since ancient times. In ancient societies, accurate predictions were important to the success of subsistence activities such as hunting, planting, and harvesting. There was a need to predict weather dynamics, such as rainfall and temperature. For example, it is crucial to plant during the period with sufficient rainfall and appropriate temperatures. Our ancestors used divination tools such as turtle shells, wooden blocks (moon blocks), or bones to make predictions. Without doubt, the accuracy was not guaranteed. Even in modern societies, prediction is still essential. Predicting traffic-jam patterns only a few hours ahead can save time by enabling the selection of an alternative route [48]. A wealth could be created by forecasting stock market trends. Predicting the future, also known as time series forecasting, is crucial.

1811

With advances in hardware technologies, we collect enormous amounts of data from diverse sources, such as smart sensors and social media platforms, continuously in the form of time series data. A time series is an ordered sequence of measures, represented in real-valued numbers, at discrete equal-interval timestamps [15]. The vast data collections have created the era of “Big Data”, which provides a wealth of datasets for developing and deploying reliable, robust, data-driven forecasting techniques to discover patterns and extract valuable information [5]. Applications can be found in the financial sector, such as predicting business cycles and stock market movements [53, 48, 76, 17] and the medical field, such as the status of critical patients according to their vital signs [88, 20] and the propagation of diseases such as influenza [17, 91] and COVID-19 [88, 60].

1821

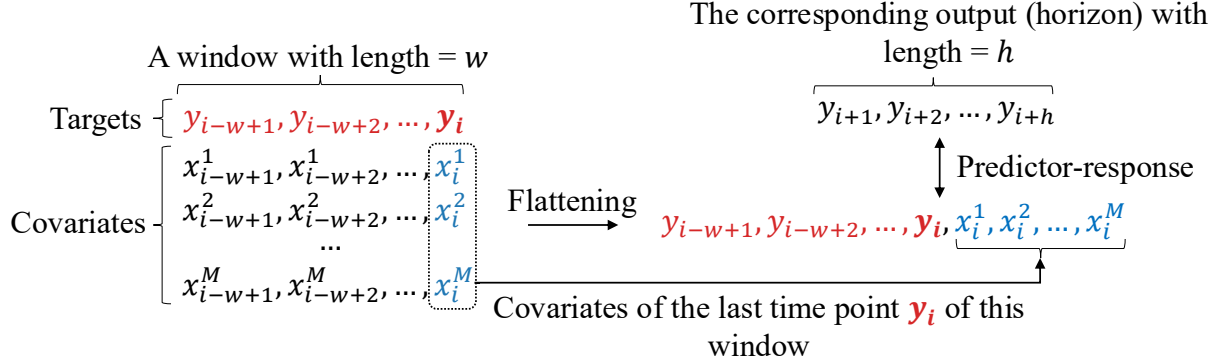


Figure 5.1: Flattening a 2D window of size  $(1+M) \times w$  to a 1D vector of length  $w+M$ . The resulting vector serves as the *predictor* for the regressor. Its expected *response* is the vector of length  $h$ . The regressor learns from this predictor-response pair.

1822     A recent study [64] shows that, in time series classification, a non-parametric, instance-  
 1823     based method, namely nearest-neighbor classifiers (1-NN) and its generalized form  $k$ -NN,  
 1824     with appropriate distance measures, such as Dynamic Time Warping (DTW), despite  
 1825     their simplicity, perform well and are therefore commonly used as benchmarks. In de-  
 1826     tail, when a new instance is to be classified,  $k$ -NN finds its  $k$  nearest neighbors in the  
 1827     training set and returns their majority label among them.  $k$ -NN is considered a lazy  
 1828     learner because the training steps involve only memorizing all the instances verbatim; no  
 1829     higher-level concepts have been learned. In addition, in time series forecasting, a recent  
 1830     study demonstrates that a well-known machine learning baseline, Gradient Boosting Re-  
 1831     gression Tree (GBRT), such as XGBoost, equipped with an appropriate data engineering  
 1832     of the data, can achieve competitive or even superior performance than the deep learning  
 1833     method. In detail, they transform the time series forecasting task into a window-based  
 1834     regression problem, as shown in Figure 5.1. For each training window of length  $w$  with  
 1835     the last time point  $\mathbf{y}_i$ , and its lagged values  $\mathbf{y}_{i-1}, \mathbf{y}_{i-2}, \dots, \mathbf{y}_{i-w+1}$  are concatenated with  
 1836     covariates  $x_i^1, x_i^2, \dots, x_i^M$  to form a *predictor* for a multi-output GBRT. This transfor-  
 1837     mation is called flattening. The corresponding response is the following  $h$  points of  $\mathbf{y}_i$ . It  
 1838     provides a simple, more efficient yet accurate method for time series forecasting.

1839     Moreover,  $k$ -NN has also shown to be a promising method for time series forecast-  
 1840     ing [59]. The  $k$ -NN uses the lagged values of the last time point to form a query  $Q$ .  
 1841     It identifies the  $k$  previous similar subsequences to  $Q$  and uses their immediate subse-  
 1842     quences to predict the immediate subsequence, which is the forecasting window, of  $Q$ .  
 1843     The intuition is that history repeats itself. The previous (historical) subsequences that  
 1844     are similar to  $Q$  can provide a hint about the future of  $Q$ . They are similar, and so are  
 1845     their immediate subsequences. Figure 5.2 depicts this idea. Observe that the immediate  
 1846     subsequence of the right gray box is similar to that of the left gray box. The left gray  
 1847     box is the nearest neighbor of the right gray in the “past”.

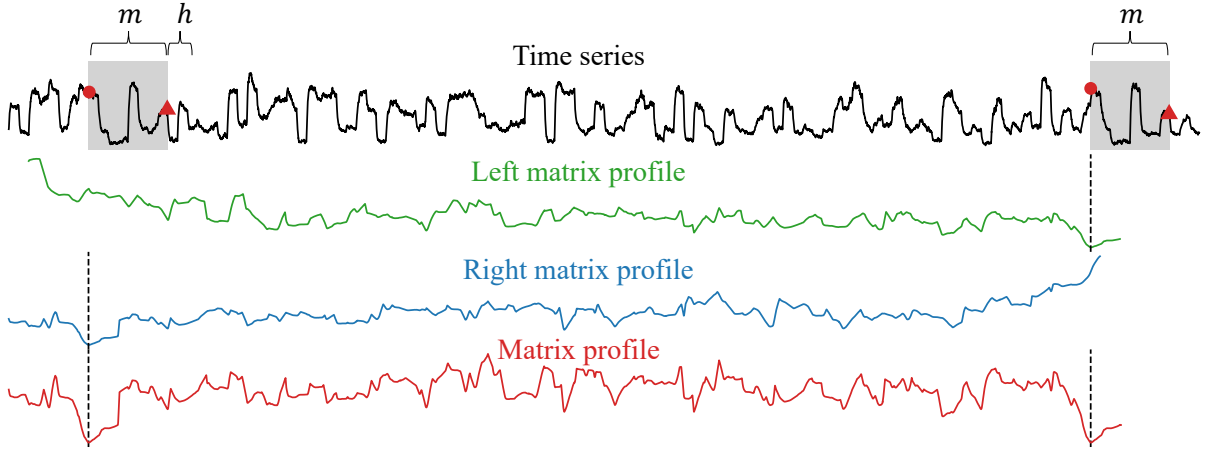


Figure 5.2: The **left** (**right**) matrix profile and the **matrix profile** of a time series. The **matrix profile** shows the distances between each  $m$ -subsequence and its nearest neighbor, where  $m$  is a user-given value. The **left** (**right**) matrix profile shows the same information but is limited to its left (right) nearest neighbor. For a particular  $m$ -subsequence shown by the right gray box, its nearest neighbor is the left gray box, as indicated by the dashed line in the **left matrix profile** and the **matrix profile**. Similarly, the nearest neighbor of the left gray box is the right gray box, as indicated by the dashed line in the **right matrix profile** and the **matrix profile**. The first (last) point in each box is denoted by a red circle (triangle).  $h$  denotes the length of the immediate subsequence of the nearest neighbor. Intuitively, this subsequence should be similar to the immediate subsequence (i.e., future) of the right gray box. To note, the **left** (**right**) matrix profile starts (ends) at a later (earlier) index because the corresponding nearest neighbor with length  $m$  does not exist.

---

**Algorithm 6** The brute force approach to compute Matrix Profile

---

```

1: for  $i \leftarrow 1$  to  $n - m + 1$  do
2:   for  $j \leftarrow 1$  to  $n - m + 1$  do
3:     Compute the z-normalized Euclidean distance between  $t_{i,m}$  and  $t_{j,m}$ .

```

---

Based on these findings, this study proposes a method to improve the performance of existing forecasters by leveraging information from the nearest neighbors of each subsequence in the target variable. For each time point  $y_i$  of the target variable  $Y$ , a window of length  $w$  is constructed with  $y_i$  as the last point, then we retrieve the window's historical nearest neighbors and use their information to create new covariates for the window. The information includes the similarities between the window and its nearest neighbors, as well as the immediate subsequences of them. The similarity can be interpreted as a measure of confidence or weight in using the information from the corresponding nearest neighbor. The intuition is that, if the similarity of the window and a neighbor is high, then the future (i.e., immediate subsequence) of the neighbor should also be similar to the future of the window. The fundamental difference between this study and previous approaches [82, 59, 87] is that they directly use the subsequent points for prediction, whereas we use the nearest neighbor information for each subsequence as covariates,

1861 which are used as primitives for other forecasters. We explain this subtle difference by  
1862 Figure 5.2. The previous approaches simply use the information of the nearest neighbors  
1863 of the last look-back window, which consisted of the last time point and its lagged values  
1864 (i.e., the right gray box), for prediction. In contrast, we use the information of the nearest  
1865 neighbors of **all** of the windows.

1866 We use the Matrix Profile [95, 102] to annotate the nearest neighbor for each  $m$ -  
1867 subsequence of a time series  $T$  of length  $n$ . The distance is the z-normalized Euclidean  
1868 distance. It may seem computationally expensive to perform this annotation at first  
1869 glance. Algorithm 6 shows the brute force approach to compute the matrix profile.  
1870 The two for-loops and the computation of z-normalized Euclidean distance, which takes  
1871  $\mathcal{O}(m)$ , indicate that the computational complexity is  $\mathcal{O}(n^2m)$ . The space complexity is  
1872  $\mathcal{O}(n^2)$  because of the pairwise distance of each subsequence with the other subsequence.  
1873 However, the matrix profile can be computed in  $\mathcal{O}(n^2)$  using an exact method, namely  
1874 STOMP [95] or its community-open-sourced version, STUMP [49]. Besides, the running  
1875 time can be further sped up by parallelization for a single machine with multiple compu-  
1876 tation units, such as CPUs or GPUs. The tool also allows us to compute the left matrix  
1877 profile to find the left nearest neighbor of each window. To note, the matrix profile an-  
1878 notates a time series with information about the nearest neighbor of each subsequence,  
1879 including the similarity with its nearest neighbor and its location, as shown in Figure 5.2.  
1880

In this study, we make the following contributions:

- We are the first to propose leveraging the matrix profile to create meaningful co-  
variates that improve forecaster performance.

The rest of this paper is organized as follows. Section 5.2 presents the related-work.  
In Section 5.3, we introduce the necessary background knowledge, then introduce our  
method. Section 5.4 contains an empirical evaluation. Finally, we conclude this paper  
and provide future work in Section 5.5.

## 1887 5.2 Related Work

1888 Many methods have been developed for time series forecasting. Traditional methods in-  
1889 clude rolling averages (RA), vector auto-regression (VAR) [48, 13], and auto-regressive  
1890 integrated moving averages (ARIMA) [27, 12, 13]. Because of their rigorous statisti-  
1891 cal properties, they have long been the standard. The shortcomings of ARIMA and  
1892 its variants include their high computational cost [48]. In contrast, VAR is arguably  
1893 the most widely used method, particularly in multivariate time series analysis, owing to  
1894 its simplicity. However, most of these traditional approaches have certain limitations.  
1895 They perform well when the data meet specific statistical assumptions, such as station-  
1896 arity [55], which means that the mean and variance of the time series remain constant

over time. It motivates the community to develop machine learning methods, particularly deep learning methods for time series forecasting. Many deep learning models have been proposed, including RNN-based models, CNN-based models, GNN-based models, Transformer-based models, and compound models that incorporate different base models mentioned before [17]. The compound models are promising. For example, RNNs are well suited to capturing long-term dependencies, whereas CNNs are well suited to capturing short-term dependencies. A good way to improve performance is to compound them. For example, LSTnet [48] integrates CNN, RNN, and autoregressive [97] techniques to extract both short-term and long-term patterns. Using the occupancy rate of a freeway as an example [48] to explain these two patterns, the “short-term” patterns refer to the morning peaks against evening peaks, while the “long-term” patterns refer to the workday patterns against weekend patterns. Clearly, a good forecaster needs to capture and distinguish both kinds of patterns. Despite the superior performance deep learning methods have achieved, they tend to be overly complex, opaque, and incur high computational costs compared to traditional techniques.

### 5.3 Method

In this section, we first formulate the time series forecasting problem, followed by the evaluation method. We then explain how to use a Gradient Boosting Regression Tree (GBRT) for forecasting. Subsequently, we discuss how to leverage the nearest neighbors’ information of each subsequence to improve GBRT’s performance. Finally, we discuss how to compute those nearest neighbors using the Matrix Profile.

To begin, we define the data type of interest: time series.

**Definition 10** (Time series). A *time series*  $T = t_1, t_2, \dots, t_n$  is a sequence of real-valued numbers with length  $= n$ .

In Definition 10,  $T$  is a univariate time series where each entry is a scalar number. If each entry is a vector consisting of scalar numbers with size  $> 1$ ,  $T$  is a multivariate time series. A multivariate time series can be regarded as a sequence of vectors. It can also be represented as a vector of univariate time series, where each univariate time series is referred to as a channel. In a dataset with more than one time series, we use  $T_i$  to denote a time series in a dataset with  $N$  time series, where  $1 \leq i \leq N$ .

The local properties of  $T$  can be analyzed through its subsequences.

**Definition 11** (Subsequence). A *subsequence*  $T_{i,m} = t_i, t_{i+1}, \dots, t_{i+m-1} = t_{i:i+m-1}$  of a  $T$  is a sequence that consists of a continuous subset of the entries from  $T$  of length  $m$  starting from  $i$ .

### 1931 5.3.1 Problem Formulation

1932 Time series forecasting is the task of predicting  $h$ -future values  $y_{t+1}, y_{t+2}, \dots, y_{t+h}$  of a  
1933 target  $Y$  at the current time point  $t$ . In this study, there is only one target variable  $Y$ .  $h$  is  
1934 the number of steps we want to predict in the future. The simplest case is one-step-ahead  
1935 forecasting, where  $h = 1$ . The predicted value is denoted as  $\hat{y}_{t+1}$  where the actual value  
1936 is  $y_{t+1}$ . It is preferable to predict multiple points in the future. It is called multi-horizon  
1937 (multi-step) forecasting, where  $h > 1$ . The task of forecasting is encoded in Equation 5.1.

$$\hat{y}_{t+\tau} = f(y_{t-w+1:t}, x_{t-w+1:t}, u_{t-w+1:t+\tau}, \tau) \quad (5.1)$$

1938 where

- 1939 •  $\hat{y}_{t+\tau}$  is a prediction of the target value at  $t + \tau$ , where  $\tau \in \{1, 2, \dots, h\}$ .
- 1940 •  $y_{t-w+1:t}$  are the actual values consisting of the current value  $y_t$  and the lag values  
1941 before it.  $y_{t-i}$  is called the lag of  $i$  or  $i$ -lag.
- 1942 •  $x_t$  are inputs that can only be known historically at time  $t$ .  $x_{t+1}$  is not known at  $t$ .
- 1943 •  $u_t$  are known inputs for all time. For example, the date information such as the  
1944 day of the week or month [55]. Even at  $t$ ,  $u_{t+i}$  where  $1 \leq i \leq \infty$  are known.

1945  $x_t$  and  $u_t$  are called covariates of  $y_t$ . The input of Equation 5.1 is a look-back window  $w$ .

1946 We explain the task of forecasting in terms of Equation 5.1. The forecasting process  
1947 estimates the value of  $y_{t+\tau}$ , denoted by  $\hat{y}_{t+\tau}$  with the aim to minimize the error function,  
1948 typically represented as a function of  $y_{t+\tau} - \hat{y}_{t+\tau}$  for each  $\tau$ . It is obvious that date  
1949 information is useful when the target variable depends on when the measurement is  
1950 taken. For example, if the target variable is the electricity consumption rate, there is a  
1951 clear pattern by month: consumption is higher during the winter and summer months,  
1952 when air conditioners and heaters are used.  $x_t$  provides additional information about the  
1953 state of  $y_t$ . For example, if the target variable is the body temperature, and  $x_t$  tells us  
1954 the severity of the sore throat, we may guess the body temperature will raise tomorrow.

### 1955 5.3.2 Evaluation Method

1956 Given a dataset  $D$  of  $N$  time series  $T_i$ , where  $1 \leq i \leq N$ , we explain how to evaluate the  
1957 performance of a forecaster on  $T_i$ . The error made by the forecaster on  $D$  is simply the  
1958 summation of errors made by the forecaster on each  $T_i$ . We now focus on a single time  
1959 series; hence, we drop the index  $i$ .  $T$  is divided into two subsequences, namely training  
1960 subsequence  $T_{\text{train}}$  and test subsequence  $T_{\text{test}}$ .

1961 In our study, the forecaster is only allowed to train on  $T_{\text{train}}$ . Recall that we are  
1962 predicting the  $h$  future values from the  $w$  values just before them. Hence, we use a

sliding window of length  $w + h$  to generate the  $w$ -predictor- $h$ -response pairs in  $T_{\text{train}}$ , enabling the forecaster to train on them. During the test (evaluation) phase, we do rolling forecasts. We predict based on the ground truth, not results generated from the model. It is used to prevent the accumulation of errors.

This concept is called “Teacher forcing” [90] because the teacher’s values are “force fed” into the forecaster when we “roll” the forecaster on the  $T_{\text{test}}$  [67]. The intuition is that, suppose each question (except the first one) in an exam depends on the answers to the previous questions, rather than simply grading every answer in the end, a teacher would grade (evaluate) the answer once it is given by the student, and provide the correct answer to the student so he can answer the next question based on the correct answer.

To evaluate the forecaster, we used the following three evaluation metrics defined as:

- Root Mean Square Error (RMSE)

$$\text{RMSE} = \sqrt{\frac{1}{n} \sum_{i=1}^n (y_i - \hat{y}_i)^2} \quad (5.2)$$

- Weighted Absolute Percentage Error (WAPE)

$$\text{WAPE} = \frac{\sum_{i=1}^n |y_i - \hat{y}_i|}{\sum_{i=1}^n |y_i|} \quad (5.3)$$

- Mean Absolute Error (MAE)

$$\text{MAE} = \frac{1}{n} \sum_{i=1}^n |y_i - \hat{y}_i| \quad (5.4)$$

where  $n$  is the length of the time series,  $y_i$ ,  $\hat{y}_i$  is ground true value and predicted value, respectively. RMSE and MAE are widely used metrics. MAE can better reflect the actual error situation than RMSE [53]. WAPE was introduced by [47]. By rewriting Equation 5.3 to Equation 5.5, it is more obvious that it is a weighted absolute percentage error.

$$\text{WAPE} = \sum_{i=1}^n w_i \frac{|y_i - \hat{y}_i|}{|y_i|} \quad (5.5)$$

where the weights are given by

$$w_i = \frac{|y_i|}{\sum_{i=1}^n |y_i|} \quad (5.6)$$

For all of them, a lower value is better.

1984    **5.3.3 Gradient Boosting Regression Tree (GBRT)**

1985    Gradient boosting [30] is a boosting algorithm that ensembles a group of weak learners  
1986    (usually decision trees) to make predictions. It sequentially adds learners to an ensemble,  
1987    with each learner connecting its predecessor. It constructs weak learners in a way that  
1988    each learner strategically corrects the predecessor’s mistakes by fitting the new learner  
1989    to the residual errors made by the predecessor [78, 33]. It can be used in classification  
1990    and regression. In this study, we focus on its use in regression. For the usage in regres-  
1991    sion, the model is called “Gradient Boosting Regression Tree (GBRT)”. Some popular  
1992    optimized implementations of gradient boosting are XGBoost [16], CatBoost [26], and  
1993    LightGBM [41]. In this study, we use XGBoost.

1994    In order to apply GBRT into time series forecasting problem, we need to cast the  
1995    input into an appropriate format to input into GBRT. The casting approach is similar to  
1996    successful time-series forecasting models, which reconfigure the time series into windowed  
1997    inputs [27]. Figure 5.1 presents the reconfiguration. For each entry of the target variable  
1998     $y_i$ , we retrieve its  $u_i$ , such as the day information from the calendar. Hence, for each  $y_i$ , it  
1999    is associated with  $x_i$  and  $u_i$ . To simplify the notation, we absorb  $u_i$  into  $x_i$ , and it is called  
2000    the covariates of  $y_i$ . The 2D window, as shown on the left-hand side in Figure 5.1, with  
2001    size  $w \times M$ , where  $M$  is the total number of covariates, is flattened into a 1D array on the  
2002    right-hand side with length  $w + M$ . To note, as suggested in the literature [27], only the  
2003    covariates of the last time-point  $i$  are kept and appended to the final vector. By recon-  
2004    figuration, we obtain the predictor-response pairs for training. In detail, the predictor is  
2005     $\textcolor{red}{y_{i-w+1}, y_{i-w+2}, \dots, y_i}$ ,  $\textcolor{blue}{x_i^1, x_i^2, \dots, x_i^M}$  where the red part refers to the current target value  
2006     $\textcolor{red}{y_i}$  and its lag values, and the blue part refers to the covariates of  $\textcolor{red}{y_i}$ . The corresponding  
2007    output is  $y_{i+1}, y_{i+2}, \dots, y_{i+h}$ , with length =  $h$ . We predict the  $h$ -horizon from the  $w$ -look  
2008    back window (i.e.  $w + M$ -flattened predictor). With this predictor-response formulation,  
2009    the forecasting problem becomes a multi-output regression problem. Standard XGBoost  
2010    cannot return a sequence of predicted values; it only returns a single number [27]. To  
2011    note, a multi-output regression problem is simply a group of single-output regression  
2012    problems. In other words, XGBoost internally simply treats the prediction of  $h$ -steps as  
2013     $h$  individual problems. Hence, the final output is produced by the  $h$  regressors rather  
2014    than by a single model. One may argue that the  $h$  regressors operate individually and  
2015    hence the temporal relationship in the output sequence is lost. However, as the individual  
2016    regressors are trained on the same flattened input, the prediction would still preserve the  
2017    temporal relationship [27].

2018    **5.3.4 Matrix Profile**

2019    We would like to find

**Definition 12** (Distance profile). A *distance profile*  $D_i = d_{i,1}, d_{i,2}, \dots, d_{i,n-m+1}$  of a  $T$  is a vector of the Euclidean distances between a given subsequence  $T_{i,m}$  and each subsequences in  $T$ , where  $d_{i,j}$  is the distance between  $T_{i,m}$  and  $T_{j,m}$ ,  $1 \leq i, j \leq n - m + 1$ . 2020  
2021  
2022

The distances are measured between z-normalized time series. 2023

**Definition 13** (Matrix profile). A *matrix profile*  $P = \min(D_1), \min(D_2), \dots, \min(D_{n-m+1})$  of  $T$  is a vector of Euclidean distances between every subsequence  $T_{i,m}$  of  $T$  and its nearest neighbor in  $T$ . 2024  
2025  
2026

**Definition 14** (Matrix profile index). A *matrix profile index*  $I = I_1, I_2, \dots, I_{n-m+1}$  of  $T$  is a vector of integers, where  $I_i = j$  if  $d_{i,j} = \min D_i$ . 2027  
2028

**Definition 15** (Left distance profile). A *left distance profile*  $D_i^L = d_{i,1}, d_{i,2}, \dots, d_{i,i-\lceil m/4 \rceil - 1}$  of  $T$  is a vector of Euclidean distances between a given subsequence  $T_{i,m}$  and each subsequence that appears before  $T_{i,m}$ . To note,  $i - \lceil m/4 \rceil - 1$  is the index location of the last eligible subsequence before  $T_{i,m}$  because of the exclusion zone. 2029  
2030  
2031  
2032

**Definition 16** (Left matrix profile). A *left matrix profile*  $P^L = \min(D_1^L), \min(D_2^L), \dots, \min(D_{n-m+1}^L)$  of  $T$  is a vector of Euclidean distances between every subsequence  $T_{i,m}$  of  $T$  and its nearest neighbor in  $T$  before it. 2033  
2034  
2035

**Definition 17** (Left matrix profile index). A *left matrix profile index*  $I^L = I_1^L, I_2^L, \dots, I_{n-m+1}^L$  of  $T$  is a vector of integers, where  $I_i^L = j$  if  $d_{i,j} = \min D_i^L$ . 2036  
2037

## 5.4 Experiments

2038

Table 5.1: Dataset Statistics.  $N$  is the number of time series in the dataset, while  $|T| = n$  is the length of each time series. “rate” refers to the measuring rate.  $w$  is the size of the look-back window.  $h$  is the size of the forecasting window, also known as the forecasting horizon.  $T_{\text{train}}$  is the training subsequence of  $T$ .  $T_{\text{test}}$  is the test subsequence of  $T$ . To note,  $|T_{\text{train}}| + |T_{\text{test}}| = n$ .

Dataset	Data			Forecasting Task		
	$N$	$n$	rate	$w, h$	$ T_{\text{train}} $	$ T_{\text{test}} $
Electricity [77]	70	26,136	hourly	24	25,968	168
Traffic [77]	90	10,560	hourly	24	10,392	168
PeMSD7(M) [77]	228	12,672	/5 mins	9	11,232	1,440
Exchange-Rate [48]	8	7,536	daily	24	6,048	1,488

2039 **5.5 Conclusion and Future work**

2040 **5.5.1 Conclusion**

2041 **5.5.2 Future Work**

2042 **Leveraging nearest neighbors' location information:** It would be beneficial to re-  
2043 trive the nearest neighbors for each subsequence in a specific range with respect to it.  
2044 Real-world applications often require the separation of information of short-term and  
2045 long-term repeating patterns for making accurate predictions [48]. Notably, the matrix  
2046 profile also provides the locations of the nearest neighbors from the matrix profile in-  
2047 dex. Using this location (index) information, we can retrieve the nearest neighbors of  
2048 each subsequence in a specified range with respect to it to find those "short-term" and  
2049 "long-term" patterns.

2050 **Extend to multidimensional case:** This study focuses on univariate time series fore-  
2051 casting, where there is a single target and no exogenous inputs. It only requires us  
2052 to find one-dimensional nearest neighbors. When there are multiple targets or a sin-  
2053 gle target with multiple exogenous inputs, we need to identify multidimensional nearest  
2054 neighbors [94] and leverage their information for forecasting.

2055 **Top- $k$  motifs:** We can use motifs instead of neighbors to receive more stable "future"  
2056 information for each window. Recall that a time series motif is a repeated pattern that  
2057 consists of at least two occurrences. A motif can be considered as a family of nearest  
2058 neighbors A nearest neighbor is a historical occurrence that instantiates this motif. The  
2059 motif captures the ideal behavior. By finding the occurrences of a motif and considering  
2060 their immediate subsequences, we can make a more confident guess about this motif. We  
2061 outline the approach for finding members of a motif<sup>1</sup> Given a subsequence  $A$  in a time  
2062 series  $T$ , we denote the left-hand side of  $A$  in  $T$  as  $T_L$ . We find  $A$ 's nearest neighbor in  
2063  $T_L$ , denoted as  $B$ . They are the two members of a motif  $M$ . We want to identify other  
2064 subsequences in  $T_L$  that belong to  $M$ . We define a threshold  $\theta = r \times \text{ED}(A, B)$ , where  
2065  $r > 1$ . The center  $M_C$  of  $M$  is defined as the average of  $A$  and  $B$ . Then, we compute  
2066 the distance profile between  $M_C$  and  $T_L$ . Any part of the distance profile that is smarter  
2067 than  $\theta$  points to a member of  $M$  in  $T_L$ . These members can then be added to  $M$ . After  
2068 identifying all the members of  $M$  and excluding these members in the next consideration,  
2069 we can find the next left nearest neighbor of  $A$  in  $T_L$ , and repeat the same process for  
2070 finding the next motif. Given a set of immediate subsequences of members (occurrences)  
2071 of  $M$ , we can compute a more stable immediate subsequence (future) associated with  $M$   
2072 by excluding the outliers among them or using the ensemble value, such as the mean or  
2073 median of them, to cancel the noise.

---

<sup>1</sup>The idea has been mentioned in <https://www.cs.ucr.edu/~eamonn/TimeSeriesMotifs/>.

**Identify outliers of immediate subsequences:** When we have a set of immediate 2074 subsequences, we can determine whether an immediate subsequence is an outlier or not 2075 by comparing it with others. We provide a heuristic to identify an outlier as follows. 2076 Recall that the length of a nearest neighbor and its immediate subsequence is  $m$  and  $h$ , 2077 respectively. We concatenate all nearest neighbors into a single long time series  $T'$ . To 2078 establish a clear boundary, we append a NaN value after each of them. It ensures that all 2079 matrix profile computations do not consider subsequences that span multiple neighbors. 2080 Then, we compute a distance profile of  $T'$  to find the nearest neighbor distance  $d_i$  of each 2081 neighbor  $i$ . Let  $S_i$  be the sequence consisting of neighbor  $i$  of length  $m$  and its immediate 2082 subsequence of length  $h$ . The expected nearest neighbor distance of  $S_i$  (found within the 2083 set of all extended sequences) should be proportional to the increase in length:  $d_i \times \frac{m+h}{m}$ . 2084 If the actual nearest neighbor distance of  $S_i$  is greater than  $r' \times (d_i \times (m + h)/m)$  among 2085 the others, where  $r'$  is a user-given value, the immediate subsequence in  $S_i$  is considered 2086 as an outlier. 2087



# Chapter 6

2088

## Conclusion and Future Directions

2089

In this thesis, we contribute to time series analysis by addressing two aspects, with applications in bioinformatics. The first is to frame the prediction of biological sequence problems as time series classification tasks. The second addresses a fundamental limitation in existing time series distance measures.

2090  
2091  
2092  
2093

In the first study, we investigate the prediction of human Dicer cleavage sites. This task is important for the biogenesis of microRNAs (miRNAs). Accurate prediction of Dicer cleavage sites is crucial for elucidating mechanisms of post-transcriptional gene regulation. Computationally, this task is a classification problem. First, we curate the dataset based on existing studies. The resulting datasets are 14-strings. Then, they are transformed into time series. We employ ROCKET-based classifiers for the classification. The main contributions are summarized as follows. We are the first to frame this problem as a multivariate time series classification problem. We introduced nine encoding methods for the transformation. In the transformation, to our surprise, we are the first to use the base-pair probabilities derived from the predicted secondary structure. We employ state-of-the-art time-series classifiers, namely ROCKET-based classifiers. They use random convolutional kernels to generate the summary statistics and then use a simple ridge classifier to generate the final results. Because of the simplicity of the transformation method and the classifiers we adopted, our framework, namely MTSCCleave, is fast. It achieved predictive performance comparable to or even better than deep learning-based state-of-the-art methods. Furthermore, MTSCCleave demonstrated substantial computational efficiency, with speedups ranging from 3.7X to 28.8X relative to existing methods. We carried out perturbation-based experiments to identify the subsequence that are important for the classification. We found that regions near the center of the pre-miRNA secondary structure are most critical for Dicer cleavage site determination. It aligns with the existing study. Future work for this study is as follows. We make use of the predicted secondary structure information to construct the complementary strand and the base pair probability sequence for the input strand. However, there is more than one predicted secondary structure for the given RNA sequence. One future work is to make

use of all potential secondary structures, each with its own pair probability sequence, and encode this data into a multivariate time series with more channels. Another area for future work is to use interpretable time series classifiers, such as those based on time series shapelets. By doing this, we can study which subsequence is critical for the definition of the classes, namely “5p cleav”, “5p non-cleav”, “3p leav”, and “3p non-cleav” because shapelets serve as the subsequence that has the most discriminating power between classes.

The second study develops a new distance measure framework, namely PSD. It aims to release a fundamental assumption that the prior studies have overlooked. There is only one scaling rate throughout the entire time series. However, there are much data that exhibits multiple rates. For example, human motion or music performance. They consist of phases. Each phase has its own expression rate. Existing distance measures cannot account for such variations. For example, DTW is designed for handling local distortions. US assumes that there is only one scaling factor in the whole series. To address this, we introduced the Piecewise Scaling Distance (PSD) framework, the first of its kind to account for multiple scaling factors. Recall that PSD is agnostic to the base measure we used. We can use any existing distance measure as the base measure. We studied the two instantiations of it. They are PSED (using Euclidean Distance as the base measure) and PSDTW (using DTW as the base measure). We provided an exact dynamic programming solution to compute PSD and three general ways to speed it up. In particular, we proposed a constrained version of it that limits the search space based on allowed segment lengths derived from scaling factor bounds. Besides, we use parallel computing and early abandoning to further accelerate it. For PSDTW, due to its quadratic complexity, we can further speed it up using lower-bounding techniques. Experiments show that PSD, and in particular PSED, perform best when the query contains multi-rate distortions, compared with ED, DTW and the other five DTW-based methods.

Future works on it are as follows. Currently, the number of segments  $P$  is given by users. It is preferable to develop a heuristic or algorithmic approach to automatically determine  $P$ . A simple heuristic is to test a range of possible  $P$ . Besides, while we have successfully applied a lower bound on PSDTW and accelerated it, the computational overhead of calculating a lower bound on PSED outweighs the pruning benefit and makes the computation slower eventually. Developing a specialized lower bound for PSED could further improve its running time. In addition, some existing works on speeding up DTW such as “incremental DTW” can reuse the accumulated cost matrix  $D$ . However, it is challenging to apply a similar method to USDTW and PSDTW due to time series interpolation.

# Bibliography

2155

- [1] Charu C. Aggarwal. *Data Mining: The Textbook*. Springer International Publishing, Cham, 2015. 2156
- [2] Charu C. Aggarwal and Chandan K. Reddy, editors. *Data Clustering: Algorithms and Applications*. Chapman and Hall/CRC, Boca Raton, 1st edition edition, August 2013. 2157
- [3] Firoz Ahmed, Rakesh Kaundal, and Gajendra PS Raghava. Phdcleav: A svm based method for predicting human dicer cleavage sites using sequence and secondary structure of mirna precursors. *BMC Bioinformatics*, 14(14):S9, October 2013. 2158
- [4] Mahmood Akhtar, Julien Epps, and Eliathamby Ambikairajah. On dna numerical representations for period-3 based exon prediction. In *2007 IEEE International Workshop on Genomic Signal Processing and Statistics*, pages 1–4, June 2007. 2159
- [5] Omar Y. Al-Jarrah, Paul D. Yoo, Sami Muhaidat, George K. Karagiannidis, and Kamal Taha. Efficient machine learning for big data: A review. *Big Data Research*, 2(3):87–93, September 2015. 2160
- [6] Bruce Alberts. *Molecular Biology of the Cell*. W. W. Norton & Company, New York, seventh edition edition, 2022. 2161
- [7] Dimitris Anastassiou. Genomic signal processing. *IEEE Signal Processing Magazine*, 18(4):8–20, July 2001. 2162
- [8] Anthony Bagnall, Jason Lines, Aaron Bostrom, James Large, and Eamonn Keogh. The great time series classification bake off: A review and experimental evaluation of recent algorithmic advances. *Data Mining and Knowledge Discovery*, 31(3):606–660, May 2017. 2163
- [9] Yu Bao, Morihiro Hayashida, and Tatsuya Akutsu. Lbsizecleav: Improved support vector machine (svm)-based prediction of dicer cleavage sites using loop/bulge length. *BMC Bioinformatics*, 17(1):487, November 2016. 2164

- 2181 [10] Gustavo E. A. P. A. Batista, Eamonn J. Keogh, Oben Moses Tataw, and Vinícius  
2182 M. A. de Souza. Cid: An efficient complexity-invariant distance for time series.  
2183 *Data Mining and Knowledge Discovery*, 28(3):634–669, May 2014.
- 2184 [11] John A Berger, Sanjit K Mitra, Marco Carli, and Alessandro Neri. Visualization  
2185 and analysis of dna sequences using dna walks. *Journal of the Franklin Institute*,  
2186 341(1):37–53, January 2004.
- 2187 [12] G. E. P. Box and David A. Pierce. Distribution of residual autocorrelations in  
2188 autoregressive-integrated moving average time series models. *Journal of the Ameri-*  
2189 *cian Statistical Association*, 65(332):1509–1526, 1970.
- 2190 [13] George E. P. Box, Gwilym M. Jenkins, Gregory C. Reinsel, and Greta M. Ljung.  
2191 *Time Series Analysis: Forecasting and Control*. John Wiley & Sons, May 2015.
- 2192 [14] Niranjan Chakravarthy, A. Spanias, L. D. Iasemidis, and K. Tsakalis. Autore-  
2193 gressive modeling and feature analysis of dna sequences. *EURASIP Journal on*  
2194 *Advances in Signal Processing*, 2004(1):1–16, December 2004.
- 2195 [15] Chris Chatfield. *The Analysis of Time Series: An Introduction, Sixth Edition*.  
2196 Chapman and Hall/CRC, New York, 6 edition, July 2003.
- 2197 [16] Tianqi Chen and Carlos Guestrin. Xgboost: A scalable tree boosting system.  
2198 In *Proceedings of the 22nd ACM SIGKDD International Conference on Knowledge*  
2199 *Discovery and Data Mining*, KDD ’16, pages 785–794, New York, NY, USA, August  
2200 2016. Association for Computing Machinery.
- 2201 [17] Zonglei Chen, Minbo Ma, Tianrui Li, Hongjun Wang, and Chongshou Li. Long  
2202 sequence time-series forecasting with deep learning: A survey. *Information Fusion*,  
2203 97:101819, September 2023.
- 2204 [18] William W. Cohen. *A Computer Scientist’s Guide to Cell Biology: A Travelogue*  
2205 *from a Stranger in a Strange Land*. Springer-Verl, New York, NY, 2007.
- 2206 [19] P. D. Cristea. Conversion of nucleotides sequences into genomic signals. *Journal of*  
2207 *Cellular and Molecular Medicine*, 6(2):279–303, 2002.
- 2208 [20] Denise Bandeira da Silva, Diogo Schmidt, Cristiano André da Costa, Rodrigo da  
2209 Rosa Righi, and Björn Eskofier. Deepsigns: A predictive model based on deep  
2210 learning for the early detection of patient health deterioration. *Expert Systems*  
2211 *with Applications*, 165:113905, March 2021.
- 2212 [21] Roger B. Dannenberg, William P. Birmingham, George P. Tzanetakis, Colin P.  
2213 Meek, Ning P. Hu, and Bryan P. Pardo. The musart testbed for query-by-humming  
2214 evaluation. *Comput. Music J.*, 28(2):34–48, June 2004.

- [22] Hoang Anh Dau, Anthony Bagnall, Kaveh Kamgar, Chin-Chia Michael Yeh, Yan Zhu, Shaghayegh Gharghabi, Chotirat Ann Ratanamahatana, and Eamonn Keogh. The ucr time series archive. *IEEE/CAA Journal of Automatica Sinica*, 6(6):1293–1305, November 2019. 2215  
2216  
2217  
2218
- [23] Angus Dempster, François Petitjean, and Geoffrey I. Webb. Rocket: Exceptionally fast and accurate time series classification using random convolutional kernels. *Data Mining and Knowledge Discovery*, 34(5):1454–1495, September 2020. 2219  
2220  
2221
- [24] Angus Dempster, Daniel F. Schmidt, and Geoffrey I. Webb. Minirocket: A very fast (almost) deterministic transform for time series classification. In *Proceedings of the 27th ACM SIGKDD Conference on Knowledge Discovery & Data Mining*, KDD ’21, pages 248–257, New York, NY, USA, August 2021. Association for Computing Machinery. 2222  
2223  
2224  
2225  
2226
- [25] Angus Dempster, Daniel F. Schmidt, and Geoffrey I. Webb. Hydra: Competing convolutional kernels for fast and accurate time series classification. *Data Mining and Knowledge Discovery*, 37(5):1779–1805, September 2023. 2227  
2228  
2229
- [26] Anna Veronika Dorogush, Vasily Ershov, and Andrey Gulin. Catboost: Gradient boosting with categorical features support. In *Workshop on ML Systems at NIPS 2017*, 2017. 2230  
2231  
2232
- [27] Shereen Elsayed, Daniela Thyssens, Ahmed Rashed, Hadi Samer Jomaa, and Lars Schmidt-Thieme. Do we really need deep learning models for time series forecasting?, October 2021. 2233  
2234  
2235
- [28] Philippe Esling and Carlos Agon. Time-series data mining. *ACM Computing Surveys*, 45(1):1–34, November 2012. 2236  
2237
- [29] Yong Feng, Xiaoxiao Zhang, Paul Graves, and Yan Zeng. A comprehensive analysis of precursor microrna cleavage by human dicer. *RNA*, 18(11):2083–2092, November 2012. 2238  
2239  
2240
- [30] Jerome H. Friedman. Greedy function approximation: A gradient boosting machine. *The Annals of Statistics*, 29(5):1189–1232, October 2001. 2241  
2242
- [31] Ada Wai-Chee Fu, Eamonn Keogh, Leo Yung Hang Lau, Chotirat Ann Ratanamahatana, and Raymond Chi-Wing Wong. Scaling and time warping in time series querying. *The VLDB Journal*, 17(4):899–921, July 2008. 2243  
2244  
2245
- [32] Tak-chung Fu. A review on time series data mining. *Engineering Applications of Artificial Intelligence*, 24(1):164–181, February 2011. 2246  
2247

- 2248 [33] Aurélien Géron. *Hands-On Machine Learning with Scikit-Learn and PyTorch: Concepts, Tools, and Techniques to Build Intelligent Systems*. O'Reilly Media, US, 2025.
- 2249
- 2250 [34] J. Gorodkin. Comparing two k-category assignments by a k-category correlation coefficient. *Computational Biology and Chemistry*, 28(5):367–374, December 2004.
- 2251
- 2252 [35] Sam Griffiths-Jones, Harpreet Kaur Saini, and Stijn van Dongen. mirbase: Tools for microrna genomics. *Nucleic Acids Research*, 36(suppl\_1):D154–D158, January 2008.
- 2253
- 2254
- 2255 [36] Shuo Gu, Lan Jin, Yue Zhang, Yong Huang, Feijie Zhang, Paul N. Valdmanis, and Mark A. Kay. The loop position of shrnas and pre-mirnas is critical for the accuracy of dicer processing in vivo. *Cell*, 151(4):900–911, November 2012.
- 2256
- 2257
- 2258 [37] Matthieu Herrmann and Geoffrey I. Webb. Amercing: An intuitive and effective constraint for dynamic time warping. *Pattern Recognition*, 137:109333, May 2023.
- 2259
- 2260 [38] Todd Holden, R. Subramaniam, R. Sullivan, E. Cheung, C. Schneider, G. Tremberger Jr, A. Flamholz, D. H. Lieberman, and T. D. Cheung. Atcg nucleotide fluctuation of deinococcus radiodurans radiation genes. In *Instruments, Methods, and Missions for Astrobiology X*, volume 6694, pages 402–411. SPIE, October 2007.
- 2261
- 2262
- 2263
- 2264 [39] Fumitada Itakura. Minimum prediction residual principle applied to speech recognition. *IEEE Transactions on Acoustics, Speech, and Signal Processing*, 23(1):67–72, February 1975.
- 2265
- 2266
- 2267 [40] Young-Seon Jeong, Myong K. Jeong, and Olufemi A. Omitaomu. Weighted dynamic time warping for time series classification. *Pattern Recognition*, 44(9):2231–2240, September 2011.
- 2268
- 2269
- 2270 [41] Guolin Ke, Qi Meng, Thomas Finley, Taifeng Wang, Wei Chen, Weidong Ma, Qiwei Ye, and Tie-Yan Liu. Lightgbm: A highly efficient gradient boosting decision tree. In *Advances in Neural Information Processing Systems*, volume 30. Curran Associates, Inc., 2017.
- 2271
- 2272
- 2273
- 2274 [42] Eamonn Keogh, Kaushik Chakrabarti, Michael Pazzani, and Sharad Mehrotra. Dimensionality reduction for fast similarity search in large time series databases. *Knowledge and Information Systems*, 3(3):263–286, August 2001.
- 2275
- 2276
- 2277 [43] Eamonn Keogh, Themistoklis Palpanas, Victor B. Zordan, Dimitrios Gunopoulos, and Marc Cardle. Indexing large human-motion databases. In *Proceedings of the Thirtieth International Conference on Very Large Data Bases - Volume 30*, VLDB '04, pages 780–791, Toronto, Canada, August 2004. VLDB Endowment.
- 2278
- 2279
- 2280

- [44] Eamonn Keogh and Chotirat Ann Ratanamahatana. Exact indexing of dynamic time warping. *Knowledge and Information Systems*, 7(3):358–386, March 2005. 2281
- [45] Eamonn J. Keogh and Michael J. Pazzani. Derivative dynamic time warping. In *Proceedings of the 2001 SIAM International Conference on Data Mining (SDM)*, 2283 Proceedings, pages 1–11. Society for Industrial and Applied Mathematics, April 2284 2001. 2285
- [46] Sang-Wook Kim, Sanghyun Park, and W.W. Chu. An index-based approach for 2287 similarity search supporting time warping in large sequence databases. In *Proceedings 17th International Conference on Data Engineering*, pages 607–614, April 2288 2001. 2289
- [47] Stephan Kolassa and Wolfgang Schütz. Advantages of the mad/mean ratio over 2291 the mape. *Foresight: The International Journal of Applied Forecasting*, 6:40–43, 2292 2007. 2293
- [48] Guokun Lai, Wei-Cheng Chang, Yiming Yang, and Hanxiao Liu. Modeling long- 2294 and short-term temporal patterns with deep neural networks. In *The 41st Interna- 2295 tional ACM SIGIR Conference on Research & Development in Information 2296 Retrieval, SIGIR ’18*, pages 95–104, New York, NY, USA, June 2018. Association 2297 for Computing Machinery. 2298
- [49] Sean M. Law. Stumpy: A powerful and scalable python library for time series data 2299 mining. *Journal of Open Source Software*, 4(39):1504, July 2019. 2300
- [50] Yoontae Lee, Kipyoungh Jeon, Jun-Tae Lee, Sunyoung Kim, and V. Narry Kim. 2301 Microrna maturation: Stepwise processing and subcellular localization. *The EMBO 2302 Journal*, 21(17):4663–4670, September 2002. 2303
- [51] Maximilian Leodolter, Claudia Plant, and Norbert Brändle. Incdtw: An r package 2304 for incremental calculation of dynamic time warping. *Journal of Statistical Software*, 2305 99:1–23, September 2021. 2306
- [52] Ker-Chau Li, Ming Yan, and Shinsheng Yuan. A simple statistical model for de- 2307 picting the cdc15-synchronized yeast cell-cycle regulated gene expression data. *Sta- 2308 tistica Sinica*, 12(1):141–158, 2002. 2309
- [53] Wenxiang Li and K. L. Eddie Law. Deep learning models for time series forecasting: 2310 A review. *IEEE Access*, 12:92306–92327, 2024. 2311
- [54] Yan Li, Tianshu Wang, and Heung-Yeung Shum. Motion texture: A two-level 2312 statistical model for character motion synthesis. *ACM Trans. Graph.*, 21(3):465– 2313 472, July 2002. 2314

- 2315 [55] Bryan Lim and Stefan Zohren. Time-series forecasting with deep learning: A sur-  
2316 vey. *Philosophical Transactions of the Royal Society A: Mathematical, Physical and*  
2317 *Engineering Sciences*, 379(2194):20200209, February 2021.
- 2318 [56] Pengyu Liu, Jiangning Song, Chun-Yu Lin, and Tatsuya Akutsu. Recgbm: A  
2319 gradient boosting-based method for predicting human dicer cleavage sites. *BMC*  
2320 *Bioinformatics*, 22(1):63, February 2021.
- 2321 [57] Ronny Lorenz, Stephan H. Bernhart, Christian Höner zu Siederdissen, Hakim Tafer,  
2322 Christoph Flamm, Peter F. Stadler, and Ivo L. Hofacker. Viennarna package 2.0.  
2323 *Algorithms for Molecular Biology*, 6(1):26, November 2011.
- 2324 [58] Ian J. MacRae, Kaihong Zhou, and Jennifer A. Doudna. Structural determinants  
2325 of rna recognition and cleavage by dicer. *Nature Structural & Molecular Biology*,  
2326 14(10):934–940, October 2007.
- 2327 [59] Francisco Martínez, María Pilar Frías, María Dolores Pérez, and Antonio Jesús  
2328 Rivera. A methodology for applying k-nearest neighbor to time series forecasting.  
2329 *Artificial Intelligence Review*, 52(3):2019–2037, October 2019.
- 2330 [60] F. Martínez-Álvarez, G. Asencio-Cortés, J. F. Torres, D. Gutiérrez-Avilés,  
2331 L. Melgar-García, R. Pérez-Chacón, C. Rubio-Escudero, J. C. Riquelme, and  
2332 A. Troncoso. Coronavirus optimization algorithm: A bioinspired metaheuristic  
2333 based on the covid-19 propagation model. *Big Data*, 8(4):308–322, August 2020.
- 2334 [61] B. W. Matthews. Comparison of the predicted and observed secondary structure  
2335 of t4 phage lysozyme. *Biochimica et Biophysica Acta (BBA) - Protein Structure*,  
2336 405(2):442–451, October 1975.
- 2337 [62] Gerardo Mendizabal-Ruiz, Israel Román-Godínez, Sulema Torres-Ramos, Ri-  
2338 cardo A. Salido-Ruiz, and J. Alejandro Morales. On dna numerical representations  
2339 for genomic similarity computation. *PLOS ONE*, 12(3):e0173288, March 2017.
- 2340 [63] Matthew Middlehurst, Ali Ismail-Fawaz, Antoine Guillaume, Christopher Holder,  
2341 David Guijo-Rubio, Guzal Bulatova, Leonidas Tsaprounis, Lukasz Mentel, Martin  
2342 Walter, Patrick Schäfer, and Anthony Bagnall. Aeon: A python toolkit for learning  
2343 from time series. *Journal of Machine Learning Research*, 25(289):1–10, 2024.
- 2344 [64] Matthew Middlehurst, Patrick Schäfer, and Anthony Bagnall. Bake off redux: A  
2345 review and experimental evaluation of recent time series classification algorithms.  
2346 *Data Mining and Knowledge Discovery*, 38(4):1958–2031, July 2024.

- [65] Lixuan Mu and Tatsuya Akutsu. Dicleaseplus: A transformer-based model to detect human dicer cleavage sites within cleavage patterns. *Genes to Cells*, 31(1):e70074, 2026. 2347  
2348  
2349
- [66] Lixuan Mu, Jiangning Song, Tatsuya Akutsu, and Tomoya Mori. Diclease: A deep learning model for predicting human dicer cleavage sites. *BMC Bioinformatics*, 25(1):13, January 2024. 2350  
2351  
2352
- [67] Kevin P. Murphy. *Probabilistic Machine Learning: An Introduction*. Adaptive Computation and Machine Learning. The MIT Press, Cambridge, Massachusetts London, England, 2022. 2353  
2354  
2355
- [68] Achuthsankar S Nair and Sivarama Pillai Sreenadhan. A coding measure scheme employing electron-ion interaction pseudopotential (eiip). *Bioinformation*, 1(6):197–202, October 2006. 2356  
2357  
2358
- [69] Thanawin Rakthanmanon, Bilson Campana, Abdullah Mueen, Gustavo Batista, Brandon Westover, Qiang Zhu, Jesin Zakaria, and Eamonn Keogh. Searching and mining trillions of time series subsequences under dynamic time warping. In *Proceedings of the 18th ACM SIGKDD International Conference on Knowledge Discovery and Data Mining*, KDD ’12, pages 262–270, New York, NY, USA, August 2012. Association for Computing Machinery. 2359  
2360  
2361  
2362  
2363  
2364
- [70] Thanawin Rakthanmanon, Bilson Campana, Abdullah Mueen, Gustavo Batista, Brandon Westover, Qiang Zhu, Jesin Zakaria, and Eamonn Keogh. Addressing big data time series: Mining trillions of time series subsequences under dynamic time warping. *ACM Trans. Knowl. Discov. Data*, 7(3):10:1–10:31, September 2013. 2365  
2366  
2367  
2368
- [71] Chotirat Ann Ratanamahatana and Eamonn Keogh. Everything you know about dynamic time warping is wrong. In *3 Rd International Workshop on Mining Temporal and Sequential Data (TDM-04)*. Citeseer, 2004. 2369  
2370  
2371
- [72] Charles Rose, Brian Guenter, Bobby Bodenheimer, and Michael F. Cohen. Efficient generation of motion transitions using spacetime constraints. In *Proceedings of the 23rd Annual Conference on Computer Graphics and Interactive Techniques*, SIGGRAPH ’96, pages 147–154, New York, NY, USA, August 1996. Association for Computing Machinery. 2372  
2373  
2374  
2375  
2376
- [73] Alejandro Pasos Ruiz, Michael Flynn, James Large, Matthew Middlehurst, and Anthony Bagnall. The great multivariate time series classification bake off: A review and experimental evaluation of recent algorithmic advances. *Data Mining and Knowledge Discovery*, 35(2):401–449, March 2021. 2377  
2378  
2379  
2380

- 2381 [74] Hiroaki Sakoe and Seibi Chiba. Dynamic programming algorithm optimization  
2382 for spoken word recognition. *IEEE Transactions on Acoustics, Speech, and Signal*  
2383 *Processing*, 26(1):43–49, February 1978.
- 2384 [75] Stan Salvador and Philip Chan. Toward accurate dynamic time warping in linear  
2385 time and space. *Intelligent Data Analysis*, 11(5):561–580, October 2007.
- 2386 [76] Nicholas I. Sapankevych and Ravi Sankar. Time series prediction using support  
2387 vector machines: A survey. *IEEE Computational Intelligence Magazine*, 4(2):24–  
2388 38, May 2009.
- 2389 [77] Rajat Sen, Hsiang-Fu Yu, and Inderjit S Dhillon. Think globally, act locally: A deep  
2390 neural network approach to high-dimensional time series forecasting. In *Advances in*  
2391 *Neural Information Processing Systems*, volume 32. Curran Associates, Inc., 2019.
- 2392 [78] Luis G. Serrano and Sebastian Thrun. *Grokking Machine Learning*. Manning,  
2393 Shelter Island, 2021.
- 2394 [79] Yilin Shen, Yanping Chen, Eamonn Keogh, and Hongxia Jin. Searching time series  
2395 with invariance to large amounts of uniform scaling. In *2017 IEEE 33rd Interna-*  
2396 *tional Conference on Data Engineering (ICDE)*, pages 111–114, April 2017.
- 2397 [80] Yilin Shen, Yanping Chen, Eamonn Keogh, and Hongxia Jin. Accelerating time  
2398 series searching with large uniform scaling. In *Proceedings of the 2018 SIAM Inter-*  
2399 *national Conference on Data Mining (SDM)*, Proceedings, pages 234–242. Society  
2400 for Industrial and Applied Mathematics, May 2018.
- 2401 [81] Ahmed Shifaz, Charlotte Pelletier, François Petitjean, and Geoffrey I. Webb. Elas-  
2402 tic similarity and distance measures for multivariate time series. *Knowledge and*  
2403 *Information Systems*, 65(6):2665–2698, June 2023.
- 2404 [82] Samya Tajmouati, Bouazza E. L. Wahbi, Adel Bedoui, Abdallah Abarda, and Mo-  
2405 hamed Dakkon. Applying k-nearest neighbors to time series forecasting: Two new  
2406 approaches. *Journal of Forecasting*, 43(5):1559–1574, 2024.
- 2407 [83] Chang Wei Tan, Angus Dempster, Christoph Bergmeir, and Geoffrey I. Webb.  
2408 Multirocket: Multiple pooling operators and transformations for fast and effective  
2409 time series classification. *Data Mining and Knowledge Discovery*, 36(5):1623–1646,  
2410 September 2022.
- 2411 [84] Chang Wei Tan, Matthieu Herrmann, Germain Forestier, Geoffrey I. Webb, and  
2412 François Petitjean. Efficient search of the best warping window for dynamic time  
2413 warping. In *Proceedings of the 2018 SIAM International Conference on Data Mining*

(SDM), Proceedings, pages 225–233. Society for Industrial and Applied Mathematics, May 2018. 2414  
2415

- [85] Chang Wei Tan, François Petitjean, and Geoffrey I. Webb. Elastic bands across 2416  
the path: A new framework and method to lower bound dtw. In *Proceedings of the 2417  
2019 SIAM International Conference on Data Mining (SDM)*, Proceedings, pages 2418  
522–530. Society for Industrial and Applied Mathematics, May 2019. 2419
- [86] Nesime Tatbul, Tae Jun Lee, Stan Zdonik, Mejbah Alam, and Justin Gottschlich. 2420  
Precision and recall for time series. In *Advances in Neural Information Processing 2421  
Systems*, volume 31. Curran Associates, Inc., 2018. 2422
- [87] Dung Tran Thi, Nha Tran Phong, and Ngoc Dung Bui. Forecast timeseries based 2423  
on matrix profile. *Journal of Informatics and Innovative Technologies (JIIT)*, 2021. 2424
- [88] José F. Torres, Dalil Hadjout, Abderrazak Sebaa, Francisco Martínez-Álvarez, and 2425  
Alicia Troncoso. Deep learning for time series forecasting: A survey. *Big Data*, 2426  
9(1):3–21, February 2021. 2427
- [89] Lisa A. Urry, Michael L. Cain, Steven Alexander Wasserman, Peter V. Minorsky, 2428  
Rebecca B. Orr, and Neil A. Campbell. *Campbell Biology*. Pearson, New York, NY, 2429  
twelfth edition edition, 2020. 2430
- [90] Ronald J. Williams and David Zipser. A learning algorithm for continually running 2431  
fully recurrent neural networks. *Neural Computation*, 1(2):270–280, June 1989. 2432
- [91] Neo Wu, Bradley Green, Xue Ben, and Shawn O’Banion. Deep transformer models 2433  
for time series forecasting: The influenza prevalence case, January 2020. 2434
- [92] Taosheng Xu, Ning Su, Lin Liu, Junpeng Zhang, Hongqiang Wang, Weijia 2435  
Zhang, Jie Gui, Kui Yu, Jiuyong Li, and Thuc Duy Le. mirbaseconverter: An 2436  
r/bioconductor package for converting and retrieving mirna name, accession, se- 2437  
quence and family information in different versions of mirbase. *BMC Bioinformat- 2438  
ics*, 19(19):514, December 2018. 2439
- [93] Dragomir Yankov, Eamonn Keogh, Jose Medina, Bill Chiu, and Victor Zordan. 2440  
Detecting time series motifs under uniform scaling. In *Proceedings of the 13th 2441  
ACM SIGKDD International Conference on Knowledge Discovery and Data Min- 2442  
ing*, KDD ’07, pages 844–853, New York, NY, USA, August 2007. Association for 2443  
Computing Machinery. 2444
- [94] Chin-Chia Michael Yeh, Nickolas Kavantzas, and Eamonn Keogh. Matrix pro- 2445  
file vi: Meaningful multidimensional motif discovery. In *2017 IEEE International 2446  
Conference on Data Mining (ICDM)*, pages 565–574, November 2017. 2447

- 2448 [95] Chin-Chia Michael Yeh, Yan Zhu, Liudmila Ulanova, Nurjahan Begum, Yifei Ding,  
2449 Hoang Anh Dau, Diego Furtado Silva, Abdullah Mueen, and Eamonn Keogh. Matrix profile i:  
2450 All pairs similarity joins for time series: A unifying view that includes  
2451 motifs, discords and shapelets. In *2016 IEEE 16th International Conference on*  
2452 *Data Mining (ICDM)*, pages 1317–1322, Barcelona, Spain, December 2016. IEEE.
- 2453 [96] Byoung-Kee Yi and Christos Faloutsos. Fast time sequence indexing for arbitrary  
2454 lp norms. In *Proceedings of the 26th International Conference on Very Large Data*  
2455 *Bases, VLDB '00*, pages 385–394, San Francisco, CA, USA, September 2000. Morgan  
2456 Kaufmann Publishers Inc.
- 2457 [97] G. Udny Yule. On a method of investigating periodicities in disturbed series, with  
2458 special reference to wolfer's sunspot numbers. *Philosophical Transactions of the*  
2459 *Royal Society of London. Series A, Containing Papers of a Mathematical or Physi-*  
2460 *cal Character*, 226:267–298, 1927.
- 2461 [98] Ren Zhang and Chun-Ting Zhang. Z curves, an intutive tool for visualizing and  
2462 analyzing the dna sequences. *Journal of Biomolecular Structure and Dynamics*,  
2463 11(4):767–782, February 1994.
- 2464 [99] Jiaping Zhao and Laurent Itti. Decomposing time series with application to tempo-  
2465 ral segmentation. In *2016 IEEE Winter Conference on Applications of Computer*  
2466 *Vision (WACV)*, pages 1–9, March 2016.
- 2467 [100] Jiaping Zhao and Laurent Itti. shapedtw: Shape dynamic time warping. *Pattern*  
2468 *Recognition*, 74:171–184, February 2018.
- 2469 [101] Jing Zhao, Xiu Wen Yang, Jian Ping Li, and Yuan Yan Tang. Dna sequences classi-  
2470 *fication based on wavelet packet analysis. In Wavelet Analysis and Its Applications*,  
2471 pages 424–429. Springer, Berlin, Heidelberg, 2001.
- 2472 [102] Yan Zhu, Makoto Imamura, Daniel Nikovski, and Eamonn Keogh. Matrix profile  
2473 vii: Time series chains: A new primitive for time series data mining. In *2017 IEEE*  
2474 *International Conference on Data Mining (ICDM)*, pages 695–704, November 2017.
- 2475 [103] Yunyue Zhu and Dennis Shasha. Warping indexes with envelope transforms for  
2476 query by humming. In *Proceedings of the 2003 ACM SIGMOD International Con-*  
2477 *ference on Management of Data, SIGMOD '03*, pages 181–192, New York, NY,  
2478 USA, June 2003. Association for Computing Machinery.
- 2479 [104] Marketa J. Zvelebil, Jeremy O. Baum, and Marketa Zvelebil. *Understanding Bioin-*  
2480 *formatics*. Garland Science, New York, 2008.